

CERN-EP-2020-116
2020/12/07

CMS-SMP-18-012

Measurements of the W boson rapidity, helicity, double-differential cross sections, and charge asymmetry in pp collisions at $\sqrt{s} = 13$ TeV

The CMS Collaboration*

Abstract

The differential cross section and charge asymmetry for inclusive W boson production at $\sqrt{s} = 13$ TeV is measured for the two transverse polarization states as a function of the W boson absolute rapidity. The measurement uses events in which a W boson decays to a neutrino and either a muon or an electron. The data sample of proton-proton collisions recorded with the CMS detector at the LHC in 2016 corresponds to an integrated luminosity of 35.9 fb^{-1} . The differential cross section and its value normalized to the total inclusive W boson production cross section are measured over the rapidity range $|y_W| < 2.5$. In addition to the total fiducial cross section, the W boson double-differential cross section, $d^2\sigma/dp_T^\ell d|\eta^\ell|$, and the charge asymmetry are measured as functions of the charged lepton transverse momentum and pseudorapidity. The precision of these measurements is used to constrain the parton distribution functions of the proton using the next-to-leading order NNPDF3.0 set.

"Published in Physical Review D as doi:10.1103/PhysRevD.102.092012."

1 Introduction

The standard model (SM) of particle physics provides a description of nature in terms of fundamental particles and their interactions mediated by vector bosons. The electromagnetic and weak interactions are described by a unified gauge theory based on the $SU(2)_L \times U(1)_Y$ symmetry group, where the photon, the W boson, and the Z boson act as mediators of the unified electroweak interaction [1–3].

Measurements of the kinematic properties of W bosons produced at hadron colliders provide stringent tests of perturbative quantum chromodynamics (QCD) calculations and probe the nature of the electroweak interaction. In particular, the measurement of the polarization of the W boson is fundamental in determining its production mechanism.

At leading order (LO) in QCD, W bosons are produced at a hadron collider with small transverse momentum (p_T) through the annihilation of a quark and an antiquark: $u\bar{d}$ for the W^+ and $\bar{u}d$ for the W^- . At the CERN LHC, W bosons with large rapidity ($|y_W|$) are produced predominantly with momentum in the same direction as the momentum of the quark that participates in the hard scattering. This is because the parton distribution functions (PDFs) of the proton favor the quark to carry a larger fraction (x) of the proton momentum rather than the antiquark [4].

Because of the $V-A$ coupling of the W boson to fermions in the SM, the spin of the W boson is aligned with that of the quark, i.e., purely left-handed, and thus aligned opposite to the direction of the momenta of both the W boson and the quark. With smaller $|y_W|$, the W bosons produced at the LHC become a mixture of left-, and right-handed polarization states at LO in QCD, and the rates of the two polarizations become equal at $|y_W| = 0$. With increasing W boson p_T (p_T^W), next-to-leading order (NLO) amplitudes contribute in its production, and longitudinally polarized W bosons arise. The relative fractions of the three polarization states depend on the relative size of the amplitudes of the three main production processes: $u\bar{d} \rightarrow W^+g$, $\bar{u}g \rightarrow W^+d$, and $g\bar{d} \rightarrow W^+\bar{u}$, and are determined by the PDFs at high values of x . Overall, left-handed W bosons are favored at the LHC over right-handed and longitudinally polarized W bosons. The relative fraction of positively (negatively) charged left-handed W bosons is around 65 (60)%, of right-handed W bosons around 28 (33)%, and of longitudinally polarized W bosons around 7 (7)% of the total production cross section. The fraction of longitudinally polarized W bosons increases monotonically with p_T^W in the p_T^W range relevant for this analysis.

At the LHC, W bosons are produced in large quantities, and it is easy to trigger on their leptonic decays ($W \rightarrow \ell\nu$) with high purity. Since the escaping neutrino means the momentum of the W boson is not known, the direct measurement of the fully differential cross section of the W boson is not possible. In particular, the polarization and rapidity distributions of the W boson must be inferred by using the PDFs. Uncertainties stemming from the imperfect knowledge of these PDFs contribute a large fraction of the overall uncertainties in recent measurements of the mass of the W boson [5] and in other high-precision measurements at the LHC [6].

Constraints on the PDFs and their uncertainties are possible through many different measurements. Recently, the ATLAS and CMS Collaborations published PDF constraints from double-differential measurements of Z boson production and the accurate measurement of $\sin^2 \theta_W$ [7–9]. Studies of W bosons have been used by the ATLAS and CMS Collaborations to set constraints on PDFs through the measurement of charge asymmetries, in particular as a function of the charged lepton pseudorapidity η^ℓ [10–18]. Measurements of associated production of a W boson and a charm quark by the ATLAS, CMS, and LHCb Collaborations at the LHC [19–

21], and by the CDF and D0 Collaborations at the Fermilab Tevatron [22, 23], also contribute to constrain the strange quark distribution within the light quark sea in the proton.

Previous measurements of the decay characteristics and polarization of W bosons have been carried out by collaborations at the Tevatron and the LHC [24–27].

Recently, a method has been proposed to directly measure the rapidity spectrum differentially in three helicity states [28] for W bosons at the LHC. It exploits the fact that the three helicity states of the leptonically decaying W boson behave differently in the two-dimensional (2D) plane of observable lepton transverse momentum p_T (p_T^ℓ) and η^ℓ .

This paper describes an experimental implementation of this novel method of measuring the W boson production differentially in its helicity states, rapidity, and electric charge. In addition, a measurement of the charge asymmetry as a function of $|y_W|$ is presented. Furthermore, cross sections for W boson production are provided as a function of the charged lepton kinematics in the 2D plane of p_T^ℓ and $|\eta^\ell|$, unfolded to particle level, along with the fiducial cross section in the experimental phase space.

The paper is organized as follows. Section 2 gives a brief description of the CMS detector, followed by Sec. 3 detailing the data sample and the simulated samples used for this analysis. Section 4 summarizes the physics object and event selection. Section 5 describes the relevant background sources and the methods to estimate their contributions. Section 6 explains the procedure to define the simulated 2D templates for p_T^ℓ and η^ℓ and the fitting strategy to perform the statistical analysis. The treatment of the systematic uncertainties is documented in Sec. 7. The results are presented in Sec. 8 and a summary in Sec. 9.

2 The CMS detector

The central feature of the CMS apparatus is a superconducting solenoid of 6 m internal diameter, providing a magnetic field of 3.8 T. A silicon pixel and strip tracker, a lead tungstate crystal electromagnetic calorimeter (ECAL), and a brass and scintillator hadron calorimeter (HCAL), each composed of a barrel and two end cap sections, reside within the solenoid volume. Muons are measured in gas-ionization detectors embedded in the steel flux-return yoke outside the solenoid. Extensive forward calorimetry complements the coverage provided by the barrel and end cap section detectors. A more detailed description of the CMS detector can be found in Ref. [29].

Events of interest are selected using a two-tiered trigger system [30]. The first level (L1), composed of custom hardware processors, uses information from the calorimeters and muon detectors to select events at a rate of around 100 kHz within a latency of 4 μ s. The second level, known as the high-level trigger (HLT), consists of a farm of processors running a version of the full event reconstruction software optimized for fast processing, and reduces the event rate to around 1 kHz before data storage. In this paper the definition “on-line” refers to quantities computed either in the L1 or in the HLT processing, while “off-line” refers to the ones evaluated later on the recorded events.

3 Data and simulated samples

The measurement is based on a data sample corresponding to an integrated luminosity of 35.9 fb⁻¹ of proton-proton (pp) collisions at a center-of-mass energy of 13 TeV recorded by the CMS experiment at the LHC during 2016.

Candidate events are selected with single-lepton triggers with online p_T thresholds of 24 (27) GeV for muons (electrons) at the HLT. For electrons, a higher threshold (up to about 40 GeV) for the L1 hardware trigger was operational during the second half of the 2016 data-taking period. These higher thresholds were present in the periods of highest instantaneous luminosities at the beginning of the LHC fills. Because of the higher trigger thresholds for electrons, the data sample for electrons is considerably smaller than that for muons and requires a careful modeling of the trigger efficiencies as a function of electron p_T . Identification and isolation criteria are applied for these triggers to suppress backgrounds before full event reconstruction.

Several Monte Carlo (MC) event generators are used to simulate the signal and background processes. The signal sample of W +jets events is simulated at NLO in perturbative QCD with the MADGRAPH5_aMC@NLO event generator in version 2.2.2. [31]. Relevant background processes are simulated with MADGRAPH5_aMC@NLO ($Z \rightarrow \ell\ell$ and $W \rightarrow \tau\nu$ at NLO, and diboson and top quark-antiquark pair ($t\bar{t}$) processes at LO), as well as with POWHEG 2.0 [32–34] at NLO (single-top processes). All simulated events are interfaced with the PYTHIA 8.226 [35] package and its CUETP8M1 [36] tune for parton showering, hadronization, and underlying event simulation. The NNPDF3.0 set of PDFs at NLO in QCD is used for all simulated event samples [37]. Additional pp interactions in the same or adjacent bunch crossings (pileup) are added to each simulated event sample. The events are weighted to match the pileup distribution in simulation to that observed in data. The average pileup in the data sample is 23.

Both simulated W and Z boson samples, generated at NLO accuracy in perturbative QCD, are further reweighted by the ratio of observed and predicted values in the p_T^Z spectrum, taken from a measurement by the CMS Collaboration using the same dataset [38]. While this procedure ensures consistency for the Z background sample, reweighting p_T^W by the measured p_T^Z data versus the MC spectrum is not inherently necessary. However, when adopting this weighting, the agreement between the observed data and the MC prediction in Z events is improved for the observable relevant to this analysis, namely p_T^ℓ . In addition, the theoretical uncertainties for the boson p_T spectrum, which will be described in Sec. 7, are large enough to cover the difference between the raw and reweighted spectra.

The detector response is simulated using a detailed description of the CMS detector implemented with the GEANT4 package [39]. Reconstruction algorithms are the same for simulated events and data.

4 Reconstruction and event selection

The analysis is performed by selecting $W \rightarrow \ell\nu$ candidate events characterized by a single prompt, energetic, and isolated lepton and missing transverse momentum (p_T^{miss}) due to the escaping neutrino. A particle-flow (PF) algorithm [40] that reconstructs all observable particles in the event is used. This algorithm classifies particles into muons, electrons, photons, and charged or neutral hadrons. It optimally combines information from the central tracking system, energy deposits in the ECAL and HCAL, and tracks in the muon detectors to reconstruct these individual particles. The algorithm also determines quality criteria, which are used to select the particles used in the distributions of the final-state observables.

Muon candidates are required to have a transverse momentum $p_T^\mu > 26$ GeV and be within the geometrical acceptance of the muon spectrometer, defined by $|\eta^\mu| < 2.4$. These values are chosen so that the inefficiency due to the trigger is minimal, once the full selection is applied.

Quality requirements on the reconstructed muons are applied to ensure high purity of the

selected events. These include requirements on the matching of the tracker information to the information from the muon system, as well as quality requirements on the combined track itself. In addition, a requirement on the relative isolation of the reconstructed muon is applied to suppress muons from background processes, such as leptonic heavy-flavor decays. This isolation variable is defined as the pileup-corrected ratio of the sum of the p_T of all charged hadrons, neutral hadrons, and photons, divided by the p_T of the muon itself [41]. It is calculated for a cone around the muon of $\Delta R = \sqrt{(\Delta\phi)^2 + (\Delta\eta)^2} < 0.4$, where ϕ is the azimuthal angle, and it is required to be smaller than 15%.

Electron candidates are formed from energy clusters in the ECAL (called superclusters) that are matched to tracks in the silicon tracker. Their p_T is required to exceed 30 GeV and they are selected within the volume of the CMS tracking system up to $|\eta^e| < 2.5$. Electrons reconstructed in the transition region between the barrel and the end cap sections, within $|\eta^e| > 1.4442$ and $|\eta^e| < 1.5660$, are rejected.

Electron identification is based on observables sensitive to bremsstrahlung along the electron trajectory and geometrical and momentum-energy matching between the electron trajectory and the associated supercluster, as well as ECAL shower-shape observables and variables that allow the rejection of the background arising from random associations of a track and a supercluster in the ECAL. Energetic photons produced in pp collision may interact with the detector material and convert into electron-positron pairs. The electrons or positrons originating from such photon conversions are suppressed by requiring that there is no more than one missing tracker hit between the primary vertex and the first hit on the reconstructed track matched to the electron; candidates are also rejected if they form a pair with a nearby track that is consistent with a conversion. Additional details of electron reconstruction and identification can be found in Refs. [42, 43].

A relative isolation variable similar to that for muons is constructed for electrons, in a cone of $\Delta R < 0.3$ around their momenta [43]. This variable is required to be less than a value that varies from around 20% in the barrel part of the detector to 8% in the end cap part. The values used are driven by similar requirements in the HLT reconstruction.

Off-line selection criteria are generally equal to or tighter than the ones applied at the HLT. Despite this, differences in the definition of the identification variables defined in the on-line system and off-line selection create differences between data and simulation that need dedicated corrections, as described in Sec. 4.1.

The analysis is carried out separately for W^+ and W^- bosons and aims to measure the charge asymmetry in W boson production, so any charge misidentification has to be reduced to a minimum. Thus, the off-line electron selection also employs a tight requirement for the charge assignment, which reduces the charge misidentification to 0.02 (0.20)% in the barrel region (end cap sections) in the p_T range of interest [44].

Events coming from $W \rightarrow \ell\nu$ decays are expected to contain one charged lepton (muon or electron) and significant p_T^{miss} resulting from the neutrino. The missing transverse momentum vector \vec{p}_T^{miss} is computed as the negative vector sum of the transverse momenta of all the PF candidates in an event, and its magnitude is denoted as p_T^{miss} [45]. No direct requirement on p_T^{miss} is applied, but a requirement is placed on the transverse mass, defined as $m_T = \sqrt{2p_T p_T^{\text{miss}}(1 - \cos \Delta\phi)}$, where $\Delta\phi$ is the angle in the transverse plane between the directions of the lepton p_T and the p_T^{miss} . Events are selected with $m_T > 40$ GeV. This requirement rejects a large fraction of QCD multijet backgrounds.

Events from background processes that are expected to produce multiple leptons, mainly $Z \rightarrow \ell\ell$, $t\bar{t}$, and diboson production are suppressed by a veto on the presence of additional electrons or muons in the event. To maximize the rejection efficiency, these events are rejected if additional leptons, selected with looser identification and isolation criteria than the selected lepton, have $p_T > 10 \text{ GeV}$.

4.1 Efficiency corrections

The measurement of differential cross sections relies crucially on the estimation of the lepton selection efficiencies, both in the collision data and in the MC, because these are among the dominant contributions to the uncertainty. For the total absolute cross sections, the uncertainties are dominated by the integrated luminosity uncertainty. For normalized differential cross sections, the correlation of the luminosity uncertainty between the inclusive and differential measurements is such that it mostly cancels out in their ratio. Thus, the dominant uncertainties are the ones related to the lepton efficiency that are not fully correlated through the lepton kinematics phase space.

The lepton efficiency is determined separately for three different steps in the event selection: the trigger (L1+HLT), the off-line reconstruction, and the off-line selection, which includes identification and isolation criteria. The lepton efficiency for each step is determined with respect to the previous one.

A technique called *tag-and-probe* is used, in which the efficiency for each step is measured for MC simulation and collision data using samples of $Z \rightarrow \ell\ell$ events with very high purity [46]. The sample is defined by selecting events with exactly two leptons. One lepton candidate, denoted as the *tag*, satisfies tight identification and isolation requirements. The other lepton candidate, denoted as the *probe*, is selected with the selection criteria that depend on the efficiency of the above steps being measured. The number of probes passing and failing the selection is determined from fits to the invariant mass distribution with $Z \rightarrow \ell\ell$ signal and background components. The backgrounds in these fits stem largely from QCD multijet events and are at the percent level. In certain regions of phase space, especially in the sample of failing probes, these backgrounds contribute significantly, requiring an accurate modeling of the background components. The nominal efficiency in collision data is estimated by fitting the Z signal using a binned template derived from simulation, convolved with a Gaussian function with floating scale and width to describe the effect of the detector resolution. An exponential function is used for the background. The nominal efficiency in MC simulation is derived from a simple ratio of the number of passing probes over all probes.

For each step, the tag-and-probe method is applied to data and to simulated samples, and the efficiency is computed as a function of lepton p_T and η . The ratio of efficiencies in data and simulation is computed together with the associated statistical and systematic uncertainties and is used to weight the simulated W boson events. The uncertainties in the efficiencies are propagated as a systematic uncertainty in the cross section measurements. The analysis strategy demands a very high granularity in the lepton kinematics. Therefore, the efficiencies are computed in slices of $\Delta\eta = 0.1$ and steps of p_T ranging from 1.5 to 5.0 GeV. A smoothing is applied as a function of lepton p_T for each slice in η , modeled by an error function. Systematic uncertainties associated with this method are propagated to the measurement and are discussed in Sec. 7.1.3. These include a correlated component across η^ℓ and an uncorrelated component related to the statistical uncertainty in each of the slices in η^ℓ .

Table 1: Estimated ratios of each background component to the total W boson signal in the $W \rightarrow \mu\nu$ and $W \rightarrow e\nu$ channels. The DY simulation includes $\ell = e, \mu, \tau$.

Processes	Bkg. to sig. ratio	
	$W \rightarrow \mu\nu$	$W \rightarrow e\nu$
$Z \rightarrow \ell\ell$ (DY)	5.2%	3.9%
$W \rightarrow \tau\nu$	3.2%	1.3%
$WW+WZ+ZZ$	0.1%	0.1%
Top	0.5%	0.5%
Wrong charge	—	0.02%
QCD	5.5%	8.2%

5 Background estimation

The selection requirements described in Sec. 4 result in a data sample of $114(51) \times 10^6$ W^+ and $88(42) \times 10^6$ W^- candidate events in the muon (electron) final state with small background. A summary of the inclusive background-to-signal ratios is shown in Table 1. The most significant residual background is QCD multijet production, where the selected nonprompt leptons stem from either semileptonic decays of heavy-flavor hadrons or are the product of misidentified jets (usually from light quarks). The former is the principal source of QCD background in the muon channel; the latter dominates the background in the electron channel, along with the production of electron-positron pairs from photon conversions.

The nonprompt-lepton background is estimated directly from data. A control sample (the *application* sample) is defined by one lepton candidate that fails the standard lepton selection criteria, but passes a looser selection. The efficiency, ϵ_{pass} , for such a loose lepton object to pass the standard selection is determined using another independent sample (the *QCD-enriched sample*) dominated by events with nonprompt leptons from QCD multijet processes. This QCD-enriched sample, which is disjointed to the signal sample by means of the requirement $m_T < 40 \text{ GeV}$, is defined by one loosely identified lepton and a jet with $p_T > 45 \text{ GeV}$ recoiling against it. The measured efficiency for the leptons in this sample, parametrized as a function of p_T and η of the lepton, is used to weight the events in the application sample by $\epsilon_{\text{pass}}/(1 - \epsilon_{\text{pass}})$ to obtain the estimated contribution from the nonprompt-lepton background in the signal region. The efficiency ϵ_{pass} is computed with granularity of $\Delta\eta = 0.1$, and in each η bin it is parametrized as a linear function of p_T .

A small fraction of the events passing the selection criteria are due to other electroweak processes, and this contribution is estimated from simulation. Drell–Yan (DY) events that produce a pair of muons or electrons, and one of the two leptons falls outside the detector acceptance, mimic the signature of W boson events rather closely. A smaller effect from DY production stems from $Z \rightarrow \tau\tau$ decays, where one τ lepton decays leptonically and the other hadronically. Additionally, events from $W \rightarrow \tau\nu$ decays are treated as background in this analysis. The light leptons from the τ decays typically exhibit lower p_T than that in signal events and are strongly suppressed by the minimum p_T^ℓ requirements. Other backgrounds arise from $t\bar{t}$ and single top production, with one of the top quarks producing a W boson that subsequently decays leptonically. There are small contributions to the background from diboson (WW, WZ, ZZ) production. Finally, for the electron channel only, the background from $W \rightarrow e\nu$, where the lepton is reconstructed with the wrong charge, is estimated. This background is completely negligible for the muon final state.

6 Template construction and fitting procedure

The measurement strategy is to fit 2D templates in the charged-lepton kinematic observables of p_T^ℓ and η^ℓ to the observed 2D distribution in data. Whereas each of the background processes results in a single template, the simulated W boson signal is divided into its three helicity states, as well as into slices of the W boson rapidity $|y_W|$. The procedure of constructing these helicity- and rapidity-binned signal templates is described below.

6.1 Construction of helicity and rapidity signal templates

The inclusive W boson production cross section at a hadron collider, with its subsequent leptonic decay, neglecting the small terms which are exclusively NLO in QCD, is given by [47]:

$$\begin{aligned} \frac{dN}{d\cos\theta^*d\phi^*} &\propto (1 + \cos^2\theta^*) + \frac{1}{2}A_0(1 - 3\cos^2\theta^*) \\ &+ A_1\sin 2\theta^*\cos\phi^* + \frac{1}{2}A_2\sin^2\theta^*\cos 2\phi^* \\ &+ A_3\sin\theta^*\cos\phi^* + A_4\cos\theta^*, \end{aligned} \quad (1)$$

where θ^* and ϕ^* are the polar and azimuthal decay angles of the lepton in the Collins–Soper frame of reference [48], where the lepton refers to the charged lepton in the case of W^- and the neutrino in the case of W^+ . The angular coefficients A_0 to A_4 in Eq. (1) depend on the W boson charge, p_T^W , and y_W , and receive contributions from QCD at leading and higher orders. When integrating Eq. (1) over ϕ^* , the cross section is written as:

$$\begin{aligned} \frac{dN}{d\cos\theta^*} &\propto (1 + \cos^2\theta^*) \\ &+ \frac{1}{2}A_0(1 - 3\cos^2\theta^*) + A_4\cos\theta^*. \end{aligned} \quad (2)$$

This expression can equivalently be written as a function of the helicity amplitudes [49]:

$$\begin{aligned} \frac{1}{N} \frac{dN}{d\cos\theta^*dp_T^W dy_W} &= \frac{3}{8}(1 \mp \cos\theta^*)^2 f_L^{(p_T^W, y_W)} \\ &+ \frac{3}{8}(1 \pm \cos\theta^*)^2 f_R^{(p_T^W, y_W)} \\ &+ \frac{3}{4}\sin^2\theta^* f_0^{(p_T^W, y_W)}, \end{aligned} \quad (3)$$

where the coefficients f_i are the helicity fractions, and the upper (lower) sign corresponds to W^+ (W^-) boson, respectively. Thus, the fractions of left-handed, right-handed, and longitudinal W bosons (f_L , f_R and f_0 , respectively) are related to the coefficients A_i of Eq. (2), with $A_0 \propto f_0$ and $A_4 \propto \mp(f_L - f_R)$ depending on the W boson charge, where by definition $f_i > 0$ and $f_L + f_R + f_0 = 1$. The generated leptons are considered before any final-state radiation (“pre-FSR leptons”) and are called pre-FSR leptons.

Since there is no helicity information in the simulated MC signal sample, the reweighting procedure is implemented based on the production kinematics of the W boson and the kinematics of the leptonic decay of the W boson.

The coefficients f_i depend strongly on the production kinematics of the W boson, namely p_T^W , $|y_W|$, and its charge. Therefore, a reweighting procedure is devised in which the $\cos\theta^*$ distribution is fitted in bins of p_T^W and $|y_W|$, separately for each charge, to extract the predicted

f_i . These spectra of the decay angle are constructed in the full phase space of the W boson production. Each simulated event is reweighted three separate times to obtain pure samples of left-handed, right-handed, and longitudinally polarized W bosons. The results of this procedure are illustrated in Fig. 1, where the simulated signal is split into the three helicity states by reweighting by the extracted helicity fractions f_i . Distributions of p_T^W and $|y_W|$ are shown for both charges of W bosons, along with the resulting distribution of the charged lepton η .

The distributions of p_T^W and $|y_W|$ are substantially different for the three helicity components. Whereas the left-handed W bosons (W_L) and the right-handed W bosons (W_R) behave in the same way as a function of p_T , their behavior in $|y_W|$ is significantly different. Their production cross sections are equal at $|y_W| = 0$, but that of the W_L component increases up to a maximum at $|y_W|$ between 3.0 and 3.5, whereas the W_R component decreases monotonically with $|y_W|$. The longitudinally polarized W bosons (W_0) have an overall much lower production cross section, which is relatively flat in $|y_W|$ and increases as a function of p_T , as expected in the Collins–Soper reference frame. The different distributions in $|y_W|$ of the W_R and W_L components, paired with the preferential decay direction of the charged lepton for these two helicity states, results in distinctly different η^ℓ distributions. For positively charged W bosons at a given $|y_W|$, the W_L component causes the charged lepton to have values of η^ℓ closer to zero. In contrast, the positively charged W_R component tends to have larger values of $|\eta^\ell|$. The opposite is true for negatively charged W bosons, i.e., the charged lepton $|\eta^\ell|$ will tend to be large for left-handed W^- bosons, whereas right-handed W^- bosons lead to leptons observed mostly at small $|\eta^\ell|$.

6.2 Fitting strategy for the rapidity-helicity measurement

The characteristic behavior of the lepton kinematics for different polarizations of the W boson can be exploited to measure the cross section for W boson production differentially in $|y_W|$ and separately for the three helicity components. This is done by splitting each of the three helicity states into bins of $|y_W|$ and constructing the charged lepton p_T^ℓ versus η^ℓ templates for each of the helicity and charge components from the MC as described above. Example 2D templates are shown in Fig. 2, where three different templates are shown for W^+ bosons. The blue template is obtained from events with a W_R produced from 0.00 to 0.25 in $|y_W|$, the red template from events with a W_R produced between 0.50 and 0.75 in $|y_W|$, and the green template from events with a W_L produced between 2.00 and 2.25 in $|y_W|$. The behavior described above is clearly seen. Another important aspect of the underlying physics may also be understood from Fig. 2: while the W bosons are produced in orthogonal regions of phase space, the resulting templates for the observable leptons overlap considerably for the different helicity and rapidity bins. This overlap is most striking for adjacent bins in $|y_W|$ in a given helicity state. In Fig. 2, the two distributions for the right-handed W boson and the distribution for the left-handed W boson show sizeable overlap, albeit with contrasting shapes as a function of the observable lepton kinematics. A consequence of the large overlaps in general, and in neighboring bins in rapidity in particular, are large (anti-)correlations in the fitted differential cross sections in helicity and rapidity.

The 2D templates in the observable lepton kinematics extend from the minimum p_T^ℓ requirement of 26 (30) GeV for muons (electrons) to a maximum value of 45 GeV in bins with width of 1 GeV. In the observable η^ℓ , the width of the bins is 0.1, extending from -2.4 (-2.5) to 2.4 (2.5) for muons (electrons).

To extract the differential cross sections in W boson rapidity for the three helicity states, the full sample of simulated W boson events is divided using the method described earlier into the

three helicity components and 10 bins of $|y_W|$ of width 0.25 up to $|y_W| = 2.5$. These separate signal processes are left freely floating in a maximum likelihood (ML) fit to the observed 2D distribution for p_T^ℓ versus η^ℓ . All events above the threshold $|y_W| = 2.5$ are fixed to the prediction from simulation and are treated as background because of the rapid loss in acceptance for certain charge and helicity combinations at higher rapidity. Additionally, the longitudinally polarized states are fixed to the MC prediction. This results in 40 freely floating cross sections in the fit, corresponding to the 10 bins in W boson rapidity for each charge, and for the left- and right-handed polarizations.

6.3 Fitting strategy for the double-differential W boson cross section

The double-differential W boson production cross sections, as functions of p_T^ℓ and $|\eta^\ell|$, are measured with an analogous technique. The double-differential cross section for each charge of the W boson is denoted by

$$\sigma^\pm = \frac{d\sigma}{d|\eta^\ell|dp_T^\ell}(\text{pp} \rightarrow W^\pm + X \rightarrow \ell^\pm \nu + X), \quad (4)$$

and can be measured in very fine bins of η^ℓ and p_T^ℓ . Current theoretical calculations predict these cross sections with next-to-NLO (NNLO) accuracy in perturbative QCD, and such a measurement is a more rigorous test of these calculations than the previous studies performed by the CDF and D0 Collaborations at the Fermilab Tevatron $p\bar{p}$ collider [10, 11], or by the ATLAS, CMS, and LHCb Collaborations at the LHC [12–18], which all measured the cross section as a function of reconstructed η^ℓ only. The CDF Collaboration has also inferred the charge asymmetry as a function of $|y_W|$ in Ref. [10]. When integrating either over the $|\eta^\ell|$ or in the p_T^ℓ dimension, the usual one-dimensional differential cross section measurement can be recovered.

This measurement is performed by fitting the same 2D distributions of p_T^ℓ versus η^ℓ , with different freely floating signal processes. As opposed to the rapidity-helicity measurement, where each signal template corresponds to one bin in the underlying $|y_W|$ and helicity state of the generated W boson, each signal process in the double-differential measurement corresponds to a bin in the underlying generated lepton p_T and lepton $|\eta|$. The generated leptons in this measurement are subject to a so-called “dressing” procedure, where electroweak radiation is added back to the charged-lepton momentum within a cone of $\Delta R < 0.1$. The unfolding corrects for bin-by-bin differences in generated versus reconstructed p_T^ℓ and η^ℓ . The resulting number of underlying signal processes increases from the 40 processes in the helicity/rapidity fit to a total of 324, corresponding to 18 bins in the p_T^ℓ times 18 bins in $|\eta^\ell|$. The generated p_T^ℓ ranges from 26 to 56 GeV. The bin widths in p_T^ℓ are 2 GeV from 26 to 30 GeV, 1.5 GeV from 30 to 48 GeV, and 2 GeV above. The bin width in $|\eta^\ell|$ is 0.1 up to $|\eta^\ell| = 1.3$, followed by 4 bins of width 0.2, and a final bin ranging from $|\eta^\ell| = 2.1$ to 2.4. Events in which the generated leptons are outside of the reconstructed acceptances are treated as a background component in this fit. The treatment of the backgrounds and the systematic uncertainties remains the same as for the rapidity/helicity fit.

6.4 Likelihood construction and fitting

A ML fit is performed to extract the parameters of interest. The construction and calculation of the likelihood, as well as the minimization are implemented using the TENSORFLOW software package originally developed for machine learning applications [50]. The benefit of such an implementation is that the gradients required for minimization are computed automatically by backpropagation, which is both faster and more numerically accurate and stable than finite

difference approaches used in existing tools. The calculation of the likelihood, and the additional linear algebra associated with the minimization algorithm, can also be parallelized on vector processing units and/or multiple threads, as well as using graphics processing units, for a further improvement in the speed of the fit. The implementation is also optimized to keep memory usage acceptable, given the large number of measurement bins and parameters, with a sparse tensor representation used where appropriate.

The negative log-likelihood function can be written as follows:

$$L = -\ln(\mathcal{L}(\text{data}|\vec{\mu}, \vec{\theta})) = \sum_i \left(-n_i^{\text{obs}} \ln n_i^{\text{exp}}(\vec{\mu}, \vec{\theta}) + n_i^{\text{exp}}(\vec{\mu}, \vec{\theta}) \right) + \frac{1}{2} \sum_k (\theta_k - \theta_k^0)^2, \quad (5)$$

with

$$n_i^{\text{exp}}(\vec{\mu}, \vec{\theta}) = \sum_p \mu_p n_{i,p}^{\text{exp}} \prod_k \kappa_{i,p,k}^{\theta_k}, \quad (6)$$

where: n_i^{obs} is the observed number of events in each bin, assumed to be independently Poisson-distributed; $n_{i,p}^{\text{exp}}$ is the expected yield per bin per process; μ_p is the freely floating signal strength multiplier per signal process fixed to unity for background processes; θ_k are the nuisance parameters associated with each systematic uncertainty; and $\kappa_{i,p,k}$ is the size of the systematic effect per bin, per process, and per nuisance parameter. The systematic uncertainties are implemented with a unit Gaussian constraint on the nuisance parameter θ_k such that the factor $\kappa_{i,p,k}^{\theta_k}$ multiplying the yield corresponds to a log-normal distribution with the mean equal to 0 and the width equal to $\ln \kappa_{i,p,k}$. All nuisance parameters are fully profiled in the fit. This parametrization corresponds to the one used by the LHC Higgs Combination Working Group [51].

The signal strength modifiers and nuisance parameters are extracted directly from the ML fit, with the corresponding covariance matrix computed from the Hessian of the likelihood at the minimum, which can also be calculated to high numerical accuracy using backpropagation. The unfolded cross sections are extracted simultaneously in the ML fit by including the dependence of the predicted cross section on the nuisance parameters associated with the theoretical uncertainties. The cross sections and corresponding covariance matrix are extracted based on the postfit values of the signal strength modifiers and nuisance parameters and their covariance.

While the cross section vectors $\vec{\sigma}$ are left freely floating when fitting for the rapidity/helicity or the double-differential cross sections, it is also possible to fix these parameters to their expected values. Performing the fit in such a way allows for the direct measurement of the constraints set by the data on every nuisance parameter. This is especially interesting for the case of the PDF uncertainties, as the large and quite pure selected sample of W bosons can place strong constraints on the PDF uncertainties by using the charged lepton kinematics.

6.5 Measurement of the charge asymmetry and unpolarized cross sections

The fit to the data is performed simultaneously for the two charge categories and to the three helicity states. Therefore, the minimization can yield combinations of the measured cross sections with the proper propagation of the uncertainties through the fit covariance matrix, either differentially in rapidity or double-differentially in p_T^ℓ and $|\eta^\ell|$.

One of the additional quantities considered is the polarized W boson charge asymmetry, de-

defined as follows:

$$\mathcal{A}^{\text{pol}}(|y_W|) = \frac{d\sigma^{\text{pol}}/d|y_W|(W^+ \rightarrow \ell^+\nu) - d\sigma^{\text{pol}}/d|y_W|(W^- \rightarrow \ell^-\bar{\nu})}{d\sigma^{\text{pol}}/d|y_W|(W^+ \rightarrow \ell^+\nu) + d\sigma^{\text{pol}}/d|y_W|(W^- \rightarrow \ell^-\bar{\nu})}, \quad (7)$$

where pol represents the W polarization state. The charge asymmetry, as a function of $|y_W|$ as extracted from the ML fit, differentially in the three polarizations, provides a more direct constraint on the PDF than the previous measurements at the LHC, which are performed differentially in the reconstructed lepton pseudorapidity [12, 16]. In the CDF Collaboration measurement [10], the W boson charge asymmetry was extracted as a function of $|y_W|$, but not separately in the W boson helicity state.

The charge asymmetry of W bosons, which is also determined from the double-differential cross section measurement, is written as follows:

$$\mathcal{A}(|\eta^\ell|, p_T^\ell) = \frac{d^2\sigma^+/d|\eta^\ell|dp_T^\ell - d^2\sigma^-/d|\eta^\ell|dp_T^\ell}{d^2\sigma^+/d|\eta^\ell|dp_T^\ell + d^2\sigma^-/d|\eta^\ell|dp_T^\ell}. \quad (8)$$

When the distribution is integrated over p_T^ℓ , the results may be compared directly with previous measurements of $\mathcal{A}(|\eta^\ell|)$ at hadron colliders. Similarly, when integrating over $|\eta^\ell|$, $\mathcal{A}(p_T^\ell)$ is obtained. These one-dimensional (1D) distributions as functions of p_T^ℓ and η^ℓ are obtained by integrating over the other variable after performing the fully differential 2D fit. Associated uncertainties are included properly from the full 2D covariance matrix of the fit.

7 Systematic uncertainties

This section describes the treatment of systematic uncertainties from experimental sources, as well as from modeling and theoretical uncertainties. In general, systematic uncertainties are divided into two types: those affecting only the normalization of the templates and those affecting their shape.

Normalization uncertainties are treated as log-normal nuisance parameters acting on a given source of background or signal. They change the overall normalization of the process by the given value, while retaining the relative contributions of the process in each of the p_T^ℓ and η^ℓ bins.

Shape uncertainties do the exact opposite. While the integral of a background or signal component is kept constant at the central value, the relative shape of the 2D template is allowed to float. This necessitates both an up and down variation of each shape nuisance parameter. These uncertainties are incorporated by means of vertical interpolation of the event count in each bin of the template.

Uncertainties can also be a combination of the two, i.e., change the normalization, as well as the shape of the 2D templates simultaneously.

7.1 Experimental uncertainties

7.1.1 QCD multijet background

The QCD multijet background is estimated from data sidebands in the lepton identification and isolation variables, as described in Sec. 5.

The uncertainty in the method itself is estimated from closure tests in a background-dominated region, obtained by inverting the m_T requirement, i.e., $m_T < 40$ (30) GeV for the μ (e) channel.

The level of agreement in this background-dominated region is an estimate of the uncertainty in the normalization of this process. The agreement in the 2D (p_T^ℓ, η^ℓ) plane is rather good for both muons and electrons, and varies with lepton η and p_T . In the case of electrons, where this background is larger than in the muon case, the central value of the QCD background is also rescaled by the values derived in this closure test.

The nonclosure amounts to about 5% in the muon final state for all the $|\eta^\ell|$ bins, and 0.5 to 5.0% in the electron final state, with larger uncertainties at higher $|\eta^\ell|$. The smaller uncertainty for electrons is related to the increased size of the misidentified-lepton dominated control sample used for closure. Each of these normalization uncertainties is treated as uncorrelated with the others.

A systematic uncertainty in the normalization of the QCD multijet background is also estimated by a closure test in the background-dominated region in bins of p_T^ℓ 3 (5) GeV wide for the muon (electron) final state. The uncertainties range from 30 to 15% (10 to 20%), depending on the p_T^ℓ region for the muon (electron) final state. Although the uncertainty is related to differences in the composition of misidentified leptons in the control and signal regions, which are common across the whole p_T^ℓ range, the fraction of real leptons from jets and random combinations of tracks and ECAL deposits within jets might change across the phase space. Thus, conservatively, these normalization uncertainties are also considered uncorrelated among each other.

The closure test is also evaluated for the two charges separately, weighting the events with the charge-independent ϵ_{pass} misidentification efficiency. The two estimates are consistent within the uncertainties, with a similar dependency on p_T^ℓ and η^ℓ . A further check was carried out by computing a charge-dependent $\epsilon_{\text{pass}}^\pm$. Based on these checks, an additional charge-dependent uncertainty of 2% is introduced in the muon case, in the same coarse bins of $|\eta^\ell|$, to include possible charge asymmetries in the production of true muons from decays in flight of heavy quarks. No additional uncertainty for electrons is added, since the dominating source of misidentified electrons is random geometric association of energy deposits in the ECAL with tracks within jets, which is charge-symmetric.

The uncertainty in the extraction of the QCD multijet efficiency ϵ_{pass} is evaluated as follows. This lepton misidentification rate, ϵ_{pass} , is extracted through a linear fit to p_T^ℓ , which has an uncertainty associated with it. While a variation of the offset parameter of this fit is absorbed by the normalization uncertainty, the linear parameter of the fit is varied, which therefore varies the QCD multijet background as a function of p_T^ℓ . This uncertainty is applied in the same uncorrelated bins of $|\eta^\ell|$ as the normalization uncertainty.

In total, 46 (55) nuisance parameters that affect the QCD multijet background estimation are considered for each charge of the muon (electron) final state. The larger number of parameters for the electrons is due to a more granular binning and the larger acceptance in η^ℓ .

7.1.2 Lepton momentum scale

The lepton momentum scales are calibrated and corrected using events from Z boson decays. Closure tests are performed by fitting the invariant mass spectrum in data and simulation with a Breit-Wigner line shape, convolved with a Crystal Ball function. The data-to-MC difference in the fitted mass of the Z boson is taken as the nonclosure. Small values of nonclosure may arise because the lepton selection, fitting model, and invariant mass range are different in the derivation of the lepton momentum scale calibrations, as compared to the analysis. This nonclosure is of the order of 10^{-4} in the muon case. For such a precision, a detailed nuisance model

was implemented to cover residual effects [52] that can remain after the calibration procedure is applied.

Systematic uncertainties in the derivation of the muon momentum scale corrections are included. These uncertainties are related to: the modeling of p_T^Z , electroweak effects on the Z boson line shape, and the effect of the acceptance on the dimuon invariant mass. Hence, they are finely grained in muon η and p_T . Furthermore, the uncertainty in the limited data and simulated Z sample is estimated from 100 statistical replicas of the two data sets. Every such replica is constructed from a subset of the total event ensemble through a case resampling using a replacement method [53]. Each of them is also finely binned in muon η and p_T . The 99 independent statistical uncertainties are diagonalized with the procedure of Ref. [54], and their independent contributions are included as shape nuisance effects.

For electron candidates, the observed residual differences in the energy scales for the data and the simulated Z sample are of the order of 10^{-3} . A procedure similar to that used for the muon momentum scale is adopted. Two systematic effects are included in fine bins of η^e and p_T^e . The first is the difference in the Z boson mass value obtained by fitting the mass peak for $Z \rightarrow e^+e^-$ events in two different ways. The first fit uses a MC template convolved with a Gaussian resolution function and the second with a functional form consisting of a Breit-Wigner line shape for a Z boson, convolved with a Crystal Ball function, with floating mean and width parameters [55, 56]. The effect is the main contribution to the systematic uncertainty, and ranges from 0.1 to 0.2% for $p_T^e < 45$ GeV and 0.2–0.3% at higher values. The second smaller systematic effect comes from the modeling of p_T^Z . In the muon case, the limited size of the samples used to derive the energy scale corrections is accounted for by the means of 100 replicas of the data and MC samples, diagonalized to get 99 independent nuisance parameters.

For both lepton flavors, the precision in the estimate of the momentum scale decreases when increasing $|\eta^\ell|$. The W boson sample with a lepton in the more forward regions of the detector still has sufficient statistical power to allow the fit to constrain the momentum scale nuisance parameters. If the systematic effect related to the momentum scale is fully correlated across the full η^ℓ acceptance, then its constraint in the profiling procedure, driven by the large effect on the templates at high $|\eta^\ell|$, may result in an unphysical constraint in the central region. This is avoided by decorrelating the nuisance parameters related to the various momentum scale systematics in wide bins of η^ℓ , for both muons and electrons. In contrast, the parameters relating to the statistical part of this uncertainty are kept fully correlated across η^ℓ .

Since the systematic uncertainty in the momentum scale of the leptons allows the p_T of a lepton to be changed and, therefore, for bin-to-bin migration, it is applied as a shape uncertainty.

7.1.3 Lepton efficiency scale factors

Data-to-simulation efficiency scale factors are derived through the tag-and-probe method, also using $Z \rightarrow \ell\ell$ events. Two types of systematic uncertainties are considered for the tag-and-probe method.

The first uncertainty comes from the scale factors themselves and depends on the functional forms used to describe the background and signal components when fitting the efficiencies in each bin of η^ℓ as a function of p_T^ℓ of the probe lepton. In order to estimate it, alternative fits are performed by using different models for the dilepton invariant mass line shape for either the Z boson events or for the combinatorial background events, resulting in different efficiencies. The alternative signal shape is a Breit-Wigner function with the nominal Z boson mass and width, convolved with an asymmetric resolution function (Crystal Ball function) with floating param-

eters. The alternative background description is done with a function modeling the invariant mass of random combinations of two leptons satisfying the minimum p_T criteria. Overall, this alternative signal and background systematic uncertainty is assumed to be correlated among all bins in η^ℓ , and the size of it ranges from a few per mill at low $|\eta^\ell|$, to around 1–2% in the very forward region.

The second type of systematic uncertainty in the lepton efficiency scale factors arises from the statistical uncertainties in the event count in each η^ℓ bin in which the efficiencies are measured. These statistical uncertainties are derived by varying the parameters of the error function that is used to interpolate between the measured efficiency values as a function of p_T^ℓ , described in Sec. 4.1, by their uncertainties. These statistical uncertainties are uncorrelated between each bin in η^ℓ . In total, this procedure of estimating the statistical uncertainty introduces three nuisance parameters for each bin in η^ℓ , resulting in a total of 144 (150) nuisance parameters per charge in the muon (electron) final state. The larger number of parameters for the electrons is due to the larger acceptance in η^ℓ . These systematic uncertainties are considered uncorrelated for the two charges since they are measured independently, and the statistical uncertainty of the data and MC sample in each bin is large.

One additional uncertainty in the trigger efficiency is included for events with electrons in the end cap sections of the detector. This uncertainty is due to a radiation-induced shift in the ECAL timing in the 2016 data-taking period, which led to an early event readout (referred to as prefiring) in the L1 trigger and a resulting reduction in the efficiency for events with significant energy deposits in the ECAL end cap sections. The correction is estimated using a set of the $Z \rightarrow e^+e^-$ events collected in collisions where, because of L1 trigger rules, the event is saved regardless of the L1 trigger decision for the in-time bunch crossing (BX). This sample is composed of events where the L1 decision is positive for the third BX before the in-time BX: this records only about 0.1% of the total $Z \rightarrow e^+e^-$ events and is thus statistically limited. The uncertainty ranges from 0.5% for $|\eta| \approx 1.5$ to 10% at $|\eta| \approx 2.5$ for electrons from W boson decays.

7.1.4 Extra lepton veto

To reduce multilepton backgrounds, especially $Z \rightarrow \ell\ell$, a veto on additional leptons is implemented. The efficiency of this veto depends on the differences in the lepton selection efficiencies between the data and MC simulation. Since more background survives the selection at higher $|\eta^\ell|$, where the uncertainties in the lepton efficiencies are larger, a normalization uncertainty is applied, equal to 2 (3)% for the muon (electron) channel. In the electron channel, an additional uncertainty is included to account for the L1 trigger prefiring effect, described previously in Sec. 7.1.3, in $Z \rightarrow e^+e^-$ events in which one electron is in one of the ECAL end cap sections. This uncertainty ranges from 2% at low electron p_T to 10% in the highest $|\eta^\ell|$ and p_T^ℓ bins.

7.1.5 Charge misidentification

The probability of mistakenly assigning the incorrect charge to a muon in the p_T^ℓ range considered is negligible (10^{-5}) [57], thus no uncertainty is introduced for this effect. For the electrons, the statistical uncertainty in the estimate of wrong charge assignment in $Z \rightarrow e^+e^-$ events reconstructed with same-sign or opposite-sign events is used. It is dominated by the limited sample of same-sign events in the 2016 dataset. The uncertainty assigned to this small background component, in the electron channel only, is 30% [44].

7.1.6 Integrated luminosity

Because of the imperfect knowledge of the integrated luminosity, a fully correlated normalization uncertainty is assigned to all processes estimated from a MC simulation. Its value is set to 2.5% [58].

7.2 Modeling and theoretical uncertainties

7.2.1 p_T^W modeling and missing higher orders in QCD

Imperfect knowledge of the p_T^W spectrum results in an uncertainty that affects the p_T^ℓ spectrum. It is most important in the region of low p_T^W , where fixed-order perturbative calculations lead to divergent cross sections as p_T^W approaches zero, which can be fixed by using resummation. The nominal templates are evaluated from the MADGRAPH5_aMC@NLO simulated sample with the p_T^W spectrum reweighted by the measured data versus MC corrections in the p_T^Z distribution obtained in data, as described in Sec. 3.

The theoretical uncertainties resulting from missing higher orders in the QCD calculations, associated with the p_T^W modeling, are implemented in such a way as to reduce the sensitivity to the theoretical prediction, at the cost of increasing the statistical uncertainty of the results. They are implemented in the following way.

Renormalization and factorization scales, μ_R and μ_F , respectively, are changed to half and twice their original value. This change is propagated to the resulting weight for each simulated event in three variations: the uncorrelated ones in which either μ_R or μ_F is varied, and the correlated one in which both are varied simultaneously but in the same direction, i.e., both up or down by a factor of two. This uncertainty is applied to all signal processes, as well as to the simulated $Z \rightarrow \ell\ell$ background. For the signal processes, these variations lead to a normalization shift that is largely independent of η^ℓ . The impact on the shape of the p_T^ℓ distribution is within 0.5% up to $p_T^\ell < 35$ GeV; however, for $p_T^\ell > 35$ GeV a significant modification of the predicted p_T^ℓ distribution is seen. These uncertainties change both the normalization and the shape of the overall 2D templates. In the case of the signal, they are split into several components. The uncertainties in μ_R and μ_F are divided into ten bins of p_T^W : [0.0, 2.9, 4.7, 6.7, 9.0, 11.8, 15.3, 20.1, 27.2, 40.2, and 13 000] GeV. These nuisance parameters are uncorrelated for each charge. In the case of the polarized cross section measurement, an uncorrelated uncertainty is used for each helicity state to account for the different production mechanisms of the longitudinally, left, and right polarized W bosons. The μ_R and μ_F uncertainties in the $W \rightarrow \tau\nu$ process are binned in the same p_T^W bins, albeit integrated in polarization, and so are uncorrelated with the signal processes.

7.2.2 Parton distribution functions

Event weights in a MC simulation derived from 100 variations of the NNPDF3.0 PDF set, referred to as replica sets, are used to evaluate the PDF uncertainty in the predictions. These 100 replicas are transformed to a Hessian representation to facilitate the treatment of PDF uncertainties in the analysis via the procedure described in Ref. [54] with 60 eigenvectors and a starting scale of 1 GeV. Because the PDFs determine the kinematics and the differential polarization of the W boson, variations of the PDFs alter the relative contribution of the W boson helicity states in p_T^W and $|y_W|$. Thus, the alternative weighting of the signal templates described in Sec. 6.1 is repeated independently for each of the 60 Hessian variations. Each signal process is reweighted once for each of the 60 independent variations as the up variation, corresponding

to one positive standard deviation. The corresponding *down* variation is obtained by mirroring the up variation with respect to the nominal template. Since the underlying PDF uncertainties also affect the DY and $W \rightarrow \tau\nu$ backgrounds, the same procedure is applied to the simulated events for these backgrounds, and the uncertainties are treated as fully correlated between the signal and these two background processes. This procedure changes the overall normalization of the templates as well as their shapes. The magnitudes of the Hessian variations are 1% or lower for the normalization, but show significantly different behavior in the p_T^ℓ versus η^ℓ plane, from which a constraint on these PDF uncertainties is expected.

7.2.3 Choice of α_s value

The 100 PDF replicas of the NNPDF3.0 set are accompanied by two variations of the strong coupling. The central value of α_s at the mass of the Z boson of 0.1180 is varied from 0.1195 to 0.1165. Both normalization and shape are affected by this variation.

7.2.4 Simulated background cross sections

The backgrounds derived from simulation, namely DY, diboson, and $W \rightarrow \tau\nu$ production, and all top quark backgrounds are subject to an overall normalization-only uncertainty. The main contributions to the theoretical uncertainty in the Z and W boson production cross section arise from the PDF uncertainties, α_s , and μ_R and μ_F . These are included as shape nuisance parameters affecting the templates of such processes, and they are fully correlated with the same parameters affecting the signal. For the $W \rightarrow \tau\nu$ process, a further 4% normalization uncertainty is assigned, to address the residual uncertainty because of the much lower p_T of the decay lepton.

For the top quark and diboson backgrounds, the kinematic distributions are well modeled by the higher-order MC generators. The uncertainties assigned to the normalization are 6 and 16%, respectively, motivated by the large theoretical cross section uncertainty for each of the contributing processes. Because these processes make a small contribution to the selected sample of events, the effect of these relatively large uncertainties is small.

7.2.5 Choice of the m_W value

Events are reweighted to two alternative values of m_W with values ± 50 MeV, with respect to the default m_W value in the generator of 80.419 GeV, using a Breit–Wigner assumption for the invariant mass distribution at the generator level. Since the central value of m_W does not significantly influence the W boson cross sections, the impact of this uncertainty is very small.

7.2.6 Modeling of QED radiation

The simulation of the signal processes models the lepton FSR through the quantum electrodynamic (QED) showering in PYTHIA within the MADGRAPH5_aMC@NLO MC generator. An uncertainty in this modeling is assessed by considering an alternative showering program, PHOTOS 3.56 [59]. A large sample of $W \rightarrow \ell\nu$ ($\ell = e^+, e^-, \mu^+, \mu^-$ separately) events is produced at the generator level only at NLO in QCD, and is interfaced to either PYTHIA or PHOTOS. The variable sensitive to FSR, which accounts for the different radiation rate and, in case of radiation, for the harder FSR photon spectrum produced by PHOTOS with respect to PYTHIA, is the ratio $r_{\text{FSR}} = p_T^{\text{dress}} / p_T^{\text{bare}}$ between the dressed lepton p_T and the bare lepton p_T (after radiation). Alternative templates are built by reweighting the nominal MADGRAPH5_aMC@NLO events by the ratio between PHOTOS and PYTHIA, as a function of r_{FSR} .

The effect of QED FSR is largely different for the two lepton flavors because of the differences in the lepton masses and the estimate of the lepton momentum. For the muons, only the track is used, and there is no explicit recovery of the FSR. For these reasons, the nuisance parameters related to this effect are kept uncorrelated between the two lepton flavors. For the electrons, the effect is derived from a combination of the measurements using the track and the ECAL super-cluster. The latter dominates the estimate for the energy range exploited in this analysis, and its reconstruction algorithm, optimized to gather the bremsstrahlung photons, also efficiently collects the FSR photons.

7.2.7 Statistical uncertainty in the W simulation

An uncertainty is assigned to reflect the limited size of the MC sample used to build the signal templates. The sample size, when considering the negative weights of the NLO corrections, corresponds to approximatively one fifth of the data sample. This is included in the likelihood with the Barlow–Beeston Lite approach [60] and represents one of the dominant contributions to the systematic uncertainty.

A summary of the systematic uncertainties is shown in Table 2. They amount to 1176 nuisance parameters for the helicity fit.

7.3 Impact of uncertainties in the measured quantities

The effects of the systematic uncertainties on the measured quantities (signal strength modifiers for one process, μ_p in Eq. (5), absolute cross sections σ_p , or normalized cross sections $\sigma_p/\sigma_{\text{tot}}$) are presented as the impact of an uncertainty in the parameter of interest. The impact on a given measured parameter μ_p from a single nuisance parameter, θ_k in Eq. (5), is defined as $C_{pk}/\sigma(\theta_k)$, where C_{pk} is the covariance for the nuisance parameter and the parameter of interest, and $\sigma(\theta_k)$ is the postfit uncertainty on the nuisance parameter. In the limit of Gaussian uncertainties, this is equivalent to the shift that is induced as the nuisance parameter θ_k is fixed and brought to its $+1\sigma$ or -1σ postfit values, with all other parameters profiled as normal. The procedure is generalized to groups of uncertainties, gathered such that each group includes conceptually related and/or strongly correlated sources. Groups are defined for:

- *luminosity* — uncertainty in integrated luminosity,
- *efficiency stat.* — uncorrelated part (in η^ℓ) of the lepton efficiency systematics,
- *efficiency syst.* — correlated part (in η^ℓ) of the lepton efficiency systematics (coming from the tag-and-probe method), L1 prefiring uncertainty for the signal electron or the second electron from $Z \rightarrow e^+e^-$ events,
- *QCD bkg.* — includes both the normalization and shape uncertainties related to the misidentified lepton background from QCD multijet events,
- *lepton scale* — uncertainty in the lepton momentum scale,
- *other experimental* — systematic uncertainties estimated from simulation and the extra-lepton veto,
- *other bkg* — normalization uncertainties for all backgrounds, except for the non-prompt background,
- *PDFs $\oplus \alpha_S$* — 60 Hessian variations of the NNPDF3.0 PDF set and α_S ,
- μ_F, μ_R, μ_{F+R} — separate μ_R and μ_F variations, plus the correlated variation of both μ_R and μ_F ,
- *FSR* — modeling of final state radiation,

Table 2: Systematic uncertainties for each source and process. Quoted numbers correspond to the size of log-normal nuisance parameters applied in the fit, while a “yes” in a given cell corresponds to the given systematic uncertainty being applied as a shape variation over the full 2D template space.

Source/process	Signal	DY	$W \rightarrow \tau\nu$	QCD	Top	Dibosons	Charge flips
Normalization uncertainty for $W \rightarrow \ell\nu$ ($\ell = \mu, e$)							
Integrated luminosity	2.5%	2.5%	2.5%	—	2.5%	2.5%	—
DY cross section	—	3.8%	—	—	—	—	—
$t\bar{t}$, single- t cross section	—	—	—	—	6%	—	—
Diboson cross section	—	—	—	—	—	16%	—
Normalization uncertainty for $W \rightarrow \mu\nu$							
QCD normalization vs. η^ℓ	—	—	—	5%	—	—	—
QCD charge asymmetry vs. η^ℓ	—	—	—	2%	—	—	—
QCD normalization vs. p_T^ℓ	—	—	—	15–30%	—	—	—
Lepton veto	—	2%	—	—	—	—	—
Normalization uncertainty for $W \rightarrow e\nu$							
QCD normalization vs. η^ℓ	—	—	—	1–6%	—	—	—
QCD normalization vs. p_T^ℓ	—	—	—	10–30%	—	—	—
Charge-flip normalization	—	—	—	—	—	—	30%
Lepton veto	—	3%	—	—	—	—	—
Shape uncertainty for $W \rightarrow \ell\nu$ ($\ell = \mu, e$)							
Lepton efficiency (syst)	yes	yes	yes	—	—	—	—
Lepton efficiency (stat)	yes	yes	yes	—	—	—	—
L1 trigger pre-firing	yes	yes	yes	—	—	—	—
60 PDF variations	yes	yes	yes	—	—	—	—
α_S	yes	yes	yes	—	—	—	—
μ_F (binned in p_T^W)	yes	—	yes	—	—	—	—
μ_R (binned in p_T^W)	yes	—	yes	—	—	—	—
μ_{F+R} (binned in p_T^W)	yes	—	yes	—	—	—	—
W boson mass	yes	—	—	—	—	—	—
μ_F	—	yes	—	—	—	—	—
μ_R	—	yes	—	—	—	—	—
μ_{F+R}	—	yes	—	—	—	—	—
μ momentum scale (syst)	yes	yes	yes	—	—	—	—
μ momentum scale (stat)	yes	yes	yes	—	—	—	—
e momentum scale (syst)	yes	yes	yes	—	—	—	—
e momentum scale (stat)	yes	yes	yes	—	—	—	—
Lepton misidentification vs. p_T^ℓ	—	—	—	yes	—	—	—
QED radiation	yes	—	—	—	—	—	—
Simulated sample size	yes	yes	yes	—	yes	yes	yes

- *MC sample size* — statistical uncertainty per bin of the template for all the samples,
- *statistical* — the statistical uncertainty in the data sample.

The impact of each group is the effect of the combined variation of all the parameters included in it. It is evaluated as $\sqrt{v^T C^{-1} v}$, where v (v^T) is (the transpose of) the matrix of the correlations between the measured parameter and the nuisance parameters within the group, and C is the subset of the covariance matrix corresponding to the nuisance parameters in the group. This is equivalent to computing the combined impact of the eigenvectors for the postfit nuisances within a group. These groups cover all the nuisance parameters included in the likelihood and are mutually exclusive. Figure 3 summarizes the relative impact of groups of systematic uncertainties for two illustrative measurements: the normalized cross sections and the charge

asymmetry for W_L , both for the combination of the muon and electron final states. The total uncertainty is not expected to be exactly equal to the sum in quadrature of the impacts due to remaining correlations between groups. The impact of uncertainties that are strongly correlated among all the rapidity bins mostly cancel when considering either the cross section normalized to the total cross section or in the charge asymmetry. In these plots, the groups of subleading uncertainties, with respect to the ones shown, are suppressed for simplicity.

In a similar manner, the effect of the statistical and systematic uncertainties is shown for the normalized double-differential cross section and for its charge asymmetry. For simplicity, the distribution is integrated over p_T^ℓ , and it is shown as a function of $|\eta^\ell|$ in Fig. 4.

The two most dominant sources of uncertainties are the uncertainty in the integrated luminosity and the uncertainty due to the limited size of the MC sample compared with the size of the recorded data set. The latter dominates for all normalized quantities, while the former is the largest contribution to the total uncertainty in most regions of the phase space for absolute quantities.

8 Results and interpretations

The template fit to the (p_T^ℓ, η^ℓ) distribution is performed on the four independent channels: $W^+ \rightarrow \mu^+ \nu$, $W^- \rightarrow \mu^- \bar{\nu}$, $W^+ \rightarrow e^+ \nu$, and $W^- \rightarrow e^- \bar{\nu}$. The observed events as a function of lepton η and p_T are shown in Figs. 5 (6) for the muon final state and Figs. 7 (8) for the electron final state for the positive (negative) charge. The upper distributions in these figures show the 1D projections in η^ℓ and p_T^ℓ . The lower distributions represent the 2D templates “unrolled” into one dimension, such that the integer bin number $\text{bin}_{\text{unrolled}} = 1 + \text{bin}_\eta + 48(50)\text{bin}_{p_T}$, with the integers $\text{bin}_\eta \in [0, 48(50)]$ and $\text{bin}_{p_T} \in [0, 18(14)]$ for the muon (electron) channel. In the projections, the sum in quadrature of the uncertainties in the 2D distribution is shown, neglecting any correlations. Therefore, these uncertainties are for illustration purposes only.

8.1 Cross section measurements

The $W^\pm \rightarrow \ell \nu$ cross section measurements are performed in both the muon and electron channels by using the negative log likelihood minimization in Eq. (5). This provides a cross-check of experimental consistency of the two decay modes and provides a method of reducing the impact of the statistical and systematic uncertainties when combining the measurements in the two channels and accounting for correlated and uncorrelated uncertainties.

8.1.1 Combination procedure

Measurements in different channels are combined by simultaneously minimizing the likelihood across channels, with common signal strengths and nuisance parameters as appropriate. Uncertainties that are correlated among channels are those corresponding to the integrated luminosity, the knowledge of specific process cross sections in the background normalizations when the process is estimated from simulation, and effects that are common to multiple processes. Uncertainties related to the estimate of the QCD background are considered uncorrelated between muon and electron channels, since they originate from the closure test of the estimate in the background-dominated regions, which are independent of each other. The estimate of the lepton misidentification probability ϵ_{pass} is also performed independently. The systematic uncertainty on ϵ_{pass} is 100% correlated between the two charges for each lepton flavor.

The statistical uncertainties in the efficiency correction factors are assumed as uncorrelated

among positive and negative charges, and among the channels, since they are derived from independent samples. The fully correlated part of the systematic uncertainty in the efficiency within a channel is assumed uncorrelated between muons and electrons since the dominant effects from the $Z \rightarrow \ell\ell$ line shape and the background sources are very different.

Most of the theoretical uncertainties are assumed 100% correlated among the four channels. They are uncertainties in the boson p_T spectrum modeling because of μ_F and μ_R uncertainties and the uncertainty in the knowledge of α_S . Another large group of nuisance parameters that are correlated among all the channels represent the effects of the PDF variations within the NNPDF3.0 set used on both the shape of the templates used and their normalization. The 60 nuisance parameters associated with the Hessian representation of the 100 PDF replicas, as well as the uncertainty in α_S , are 100% correlated among all the four lepton flavor and charge channels. These 60+1 systematic uncertainties are also fully correlated with the respective uncertainties considered for the Z and $W \rightarrow \tau\nu$ processes.

8.1.2 Differential cross sections in $|y_W|$

The measured $|y_W|$ -dependent cross section, for the left- and right-handed polarizations, is extracted from the fit in 10 bins of $|y_W|$ with a constant width of $\Delta y_W = 0.25$ in a range $|y_W| < 2.5$. The cross sections in the two additional bins, $2.5 < |y_W| < 2.75$ and $2.75 < |y_W| < 10$, that integrate over the kinematic region in which the detector acceptance is small, are fixed to the expectation from MADGRAPH5_aMC@NLO with a large 30% normalization uncertainty. To achieve a partial cancellation of uncertainties that are largely correlated among all $|y_W|$ bins, the cross sections are normalized to the fitted total W boson cross section integrating over all the rapidity bins within the acceptance. As stated before, the longitudinally polarized component is fixed to the MADGRAPH5_aMC@NLO prediction with a 30% normalization uncertainty. Therefore, it is not a freely floating parameter in the fit, and hence only the W_L and W_R components are shown in the following.

The measured W boson production cross sections, split into the left- and right-handed helicity states for the combination of the muon and the electron channels, are presented in Fig. 9, normalized to the total cross section in the whole rapidity range. The experimental distributions are compared with the theoretical prediction from MADGRAPH5_aMC@NLO. The central value from the MADGRAPH5_aMC@NLO prediction, where the p_T^W spectrum in simulation is weighted by the ratio of measured and predicted spectrum for DY production as described in Sec. 3, is also shown as a line within the error bands and denoted as MADGRAPH5_aMC@NLO*. It is evident that this weighting has a small impact on the rapidity spectrum, and the alternative expected distributions are well within the other theoretical uncertainties. The uncertainty shown in the theoretical prediction includes the contribution from the PDFs (NNPDF3.0 set), the envelope of the μ_F and μ_R variations, and the α_S .

The main systematic uncertainty in the signal cross section, the 2.5% uncertainty in the integrated luminosity [58], is fully correlated across all the rapidity bins, thus it cancels out when taking the ratio to the total W cross section. The ratio of the expected normalized cross section using the nominal MADGRAPH5_aMC@NLO simulation to the measured one in data is also presented. As described in Sec. 6.5, the fitted $|y_W|$ -dependent cross sections are used to simultaneously derive the differential charge asymmetry. This is presented in Fig. 10, differentially in $|y_W|$ and polarization.

There are significant correlated uncertainties between neighboring W boson rapidity bins. The correlations arising only from the overlap of the signal templates in the (p_T^ℓ, η^ℓ) plane, i.e., of a purely statistical nature, are in the range 50–80% for adjacent W boson rapidity bins ($\Delta|y_W| =$

1), raising with $|y_W|$, about 20% for $\Delta|y_W| = 2$, about 10% or less for $\Delta|y_W| = 3$, and negligible otherwise. An overall correlation sums up to these statistical correlations, originating from systematic uncertainties common to all the signal processes, such as the uncertainty in the integrated luminosity.

The cross section results differential in W boson rapidity are tested for statistical compatibility with a smooth functional shape, taking these correlations into account. Monte Carlo pseudo-experiments show that the results are quantitatively consistent with smooth third-order polynomial functions of $|y_W|$. This test is performed simultaneously in both helicity states, both charges, and all $|y_W|$ bins, taking into account the full covariance matrix of the fit.

Results are also shown as an unpolarized normalized cross section, i.e., by summing over all helicity states as a function of $|y_W|$ in Fig. 11. The unpolarized charge asymmetry as a function of $|y_W|$ is shown in Fig. 12.

In addition to these normalized and unpolarized cross sections, the results of the fits are also presented as absolute cross sections in Fig. 13, where the absolute unpolarized cross sections are shown for the combined flavor fit. Generally, good agreement is observed in the shape of the measured distribution with respect to the expectation, albeit with an offset of the order of a few percent.

After the fit with floating cross sections is performed, only a few nuisance parameters are significantly constrained. Mainly the nuisance parameters related to the normalization of the nonprompt-lepton background and its shape in η^ℓ and p_T^ℓ are constrained by the fit. Because of the large data sample, this effect is expected.

8.1.3 Double-differential cross sections in p_T^ℓ and $|\eta^\ell|$

Double-differential cross sections in p_T^ℓ and $|\eta^\ell|$ are measured from a fit to the observed data in the (p_T^ℓ, η^ℓ) plane. The underlying generated templates are unfolded to the dressed lepton definition in 18 bins of p_T^ℓ and 18 bins of $|\eta^\ell|$, as described in Sec. 6.3. These cross sections are shown in Fig. 14, normalized to the total cross section. These results come from the combination of the muon and electron final states, divided into two categories of the lepton charge. From the measured cross sections, the double-differential charge asymmetry is computed, where the uncertainty is computed from the full covariance matrix from the fit, and it is shown in Fig. 15.

The agreement of the measured normalized W boson cross sections and charge asymmetry with the prediction of MADGRAPH5_aMC@NLO is at the level of 1% in the central part of the lepton acceptance ($|\eta^\ell| < 1$). In the outer end cap sections of the detector, especially for lower p_T^ℓ , the agreement with the prediction becomes worse.

Although these normalized cross sections of the combined flavor fit represent the result with the smallest total uncertainty because of the cancellation of the fully correlated components, the absolute cross sections are also of interest. In particular, the agreement of the absolute cross sections measured in each flavor channel separately highlights the understanding of the experimental systematic uncertainties, which are largely uncorrelated between the two flavors. These plots are displayed in Fig. 16, where the measured absolute cross sections are shown separately for the muon, electron, and combined fits. Good agreement is found within the uncertainties in the regions with sufficient event count. Uncertainties become large in the high- $|\eta^\ell|$ region for the electron-only fit, rendering a precise comparison difficult.

From the results of this fit, the single-differential cross section is measured by integrating in one of the two dimensions, as a function of the other variable. Along with these cross sections,

the charge asymmetry differential in one dimension is extracted. This approach has the added value, with respect to a single-differential measurement, that it is independent of the modeling of the lepton kinematics in the variable that is integrated over. The resulting absolute cross sections for the combination of the two lepton flavors is shown as a function of η^ℓ for both W^+ and W^- in Fig. 17. The corresponding W charge asymmetry is shown in Fig. 18. This result can be directly compared with previous measurements of the W boson differential cross section and charge asymmetry as functions of η^ℓ performed at 7 and 8 TeV by the CMS and ATLAS Collaborations [12, 57].

As a further summary of this fit, the total W boson production cross section, integrated over the fiducial region, $26 < p_T^\ell < 56$ GeV and $|\eta^\ell| < 2.4$, is measured. The fiducial charge-integrated cross section is 8.47 ± 0.10 nb, which agrees well with the NLO prediction. The values for each charge, and their ratio to the theoretical prediction, are also shown in Fig. 19, as well as the ratio of the two charges to the prediction from MADGRAPH5_aMC@NLO.

8.2 Constraining the PDF nuisances through likelihood profiling

When the cross section parameters in the likelihood function of Eq. (5) are fixed to their expected values ($\mu_p = 1$) within their uncertainties, the fit has the statistical power to constrain the PDF nuisance parameters. This procedure corresponds to the PDF profiling method described in Ref. [12], with associated caveats about the interpretation of constraints far from the initial predictions. The constraints in this case are derived directly from the detector-level measurements rather than passing through an intermediate step of unfolded cross sections.

The input PDF and MC predictions are both accurate to NLO in QCD, with the MC prediction implicitly including resummation corrections through the parton shower. The theoretical uncertainties included in this procedure for missing higher orders in QCD correspond to the full model used for the measurement as described in Sec. 7.2. This is in contrast to typical global PDF fits or QCD analyses that are performed at NNLO accuracy, though at fixed order without resummation, and with the inclusion of missing higher order uncertainties only in dedicated studies at NLO so far [61, 62].

For each variation, the fit input value (prefit) is trivially represented by a parameter with mean zero and width one. The expected postfit values of these parameters all have mean zero, but a reduced uncertainty after the likelihood profiling procedure, i.e., width smaller than unity. Finally, the points representing the observed postfit values of the parameters may have a mean different from zero, indicating a pull of the associated systematic uncertainty, and a width smaller than 1.

Such a result can be obtained in both the helicity and the double-differential cross section fits, and they indeed provide a consistent set of PDF nuisance parameter values. The ones reported in this section, shown in Fig. 20, come from the former fit. These parameters correspond to the 60 orthogonalized Hessian PDF variations corresponding to the NNPDF3.0 replicas, plus α_s . All of the variants, i.e., prefit, postfit expected, and postfit observed, are shown. Postfit constraints of $\simeq 70\%$ of the prefit values are observed in some of the PDF nuisance parameters, Whereas the mean constraint is closer to $\simeq 90\%$. The postfit nuisance parameter values, with respect to the prefit values and uncertainties, give a χ^2 value of 117 for 61 degrees of freedom. This suggests that the PDF set used here at NLO QCD plus parton shower accuracy may not be sufficient to describe the data. It is possible that NNLO QCD accuracy combined with additional developments in fitting methodology incorporated in more recent PDF fits may improve the situation, and this can be studied in detail on the basis of the unfolded cross sections measured here.

8.3 Additional plots

Additional plots on the helicity and rapidity analysis are presented in Appendix A.1, and additional plots on the two-dimensional cross sections are presented in Appendix A.2.

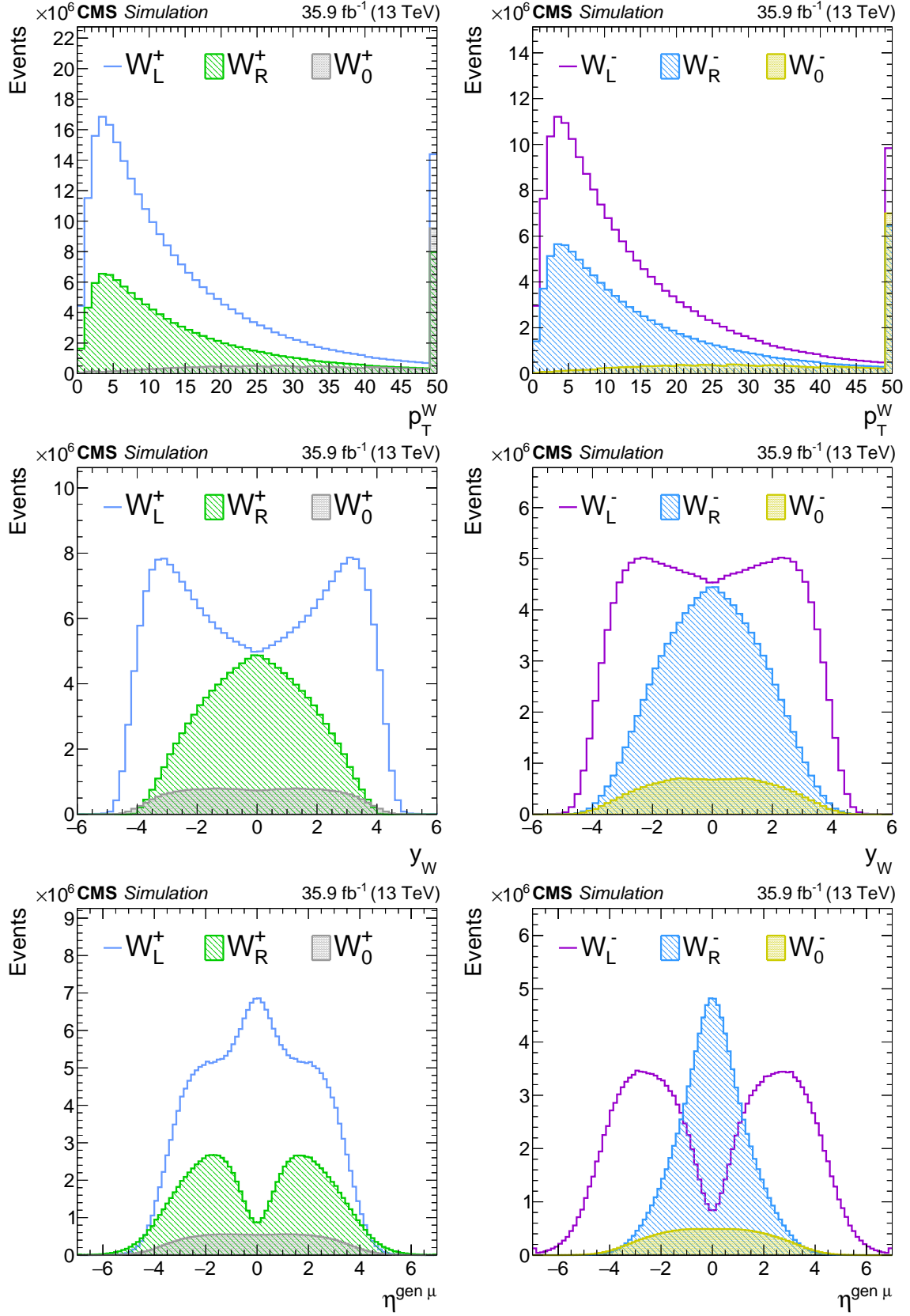


Figure 1: Generator-level distributions of the W boson p_T^W (top), $|y_W|$ (center), and the resulting η distribution of the charged lepton (bottom) after reweighting each of the helicity components for positively (left) and negatively (right) charged W bosons.

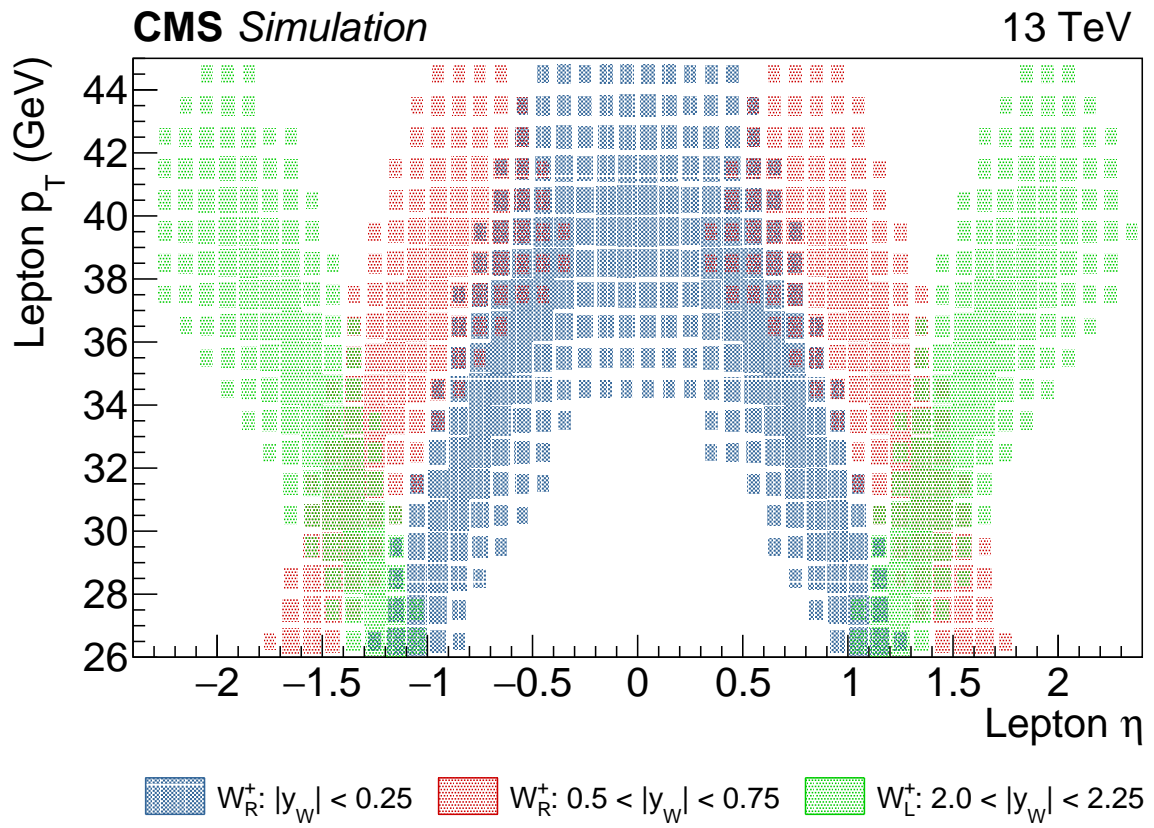


Figure 2: Distributions of 2D templates of p_T^ℓ versus η^ℓ for simulated positively charged W bosons events in different helicity or rapidity bins. Templates for the muon channel are shown. Blue: W_R^+ with $|y_W| < 0.25$, red: W_R^+ with $0.50 < |y_W| < 0.75$, and green: W_L^+ with $2.00 < |y_W| < 2.25$.

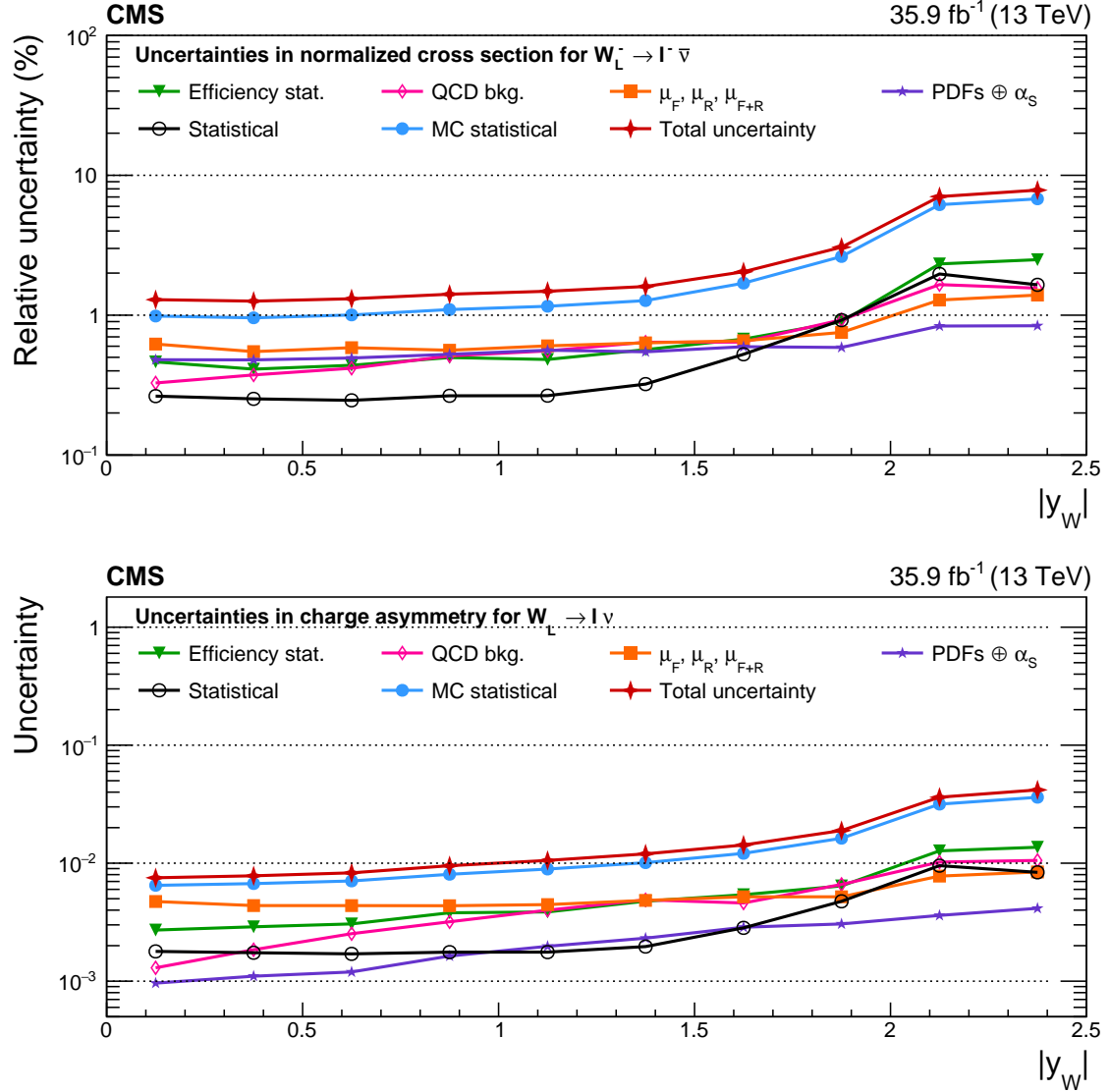


Figure 3: Upper: relative impact of groups of uncertainties (as defined in the text) on the normalized signal cross sections as functions of the W boson rapidity for the W_L^- case. Lower: absolute impact of uncertainties on the charge asymmetry of the W_L boson. All impacts are shown for the combination of the muon and electron channels in the helicity fit. The groups of uncertainties subleading to the ones shown are suppressed for simplicity.

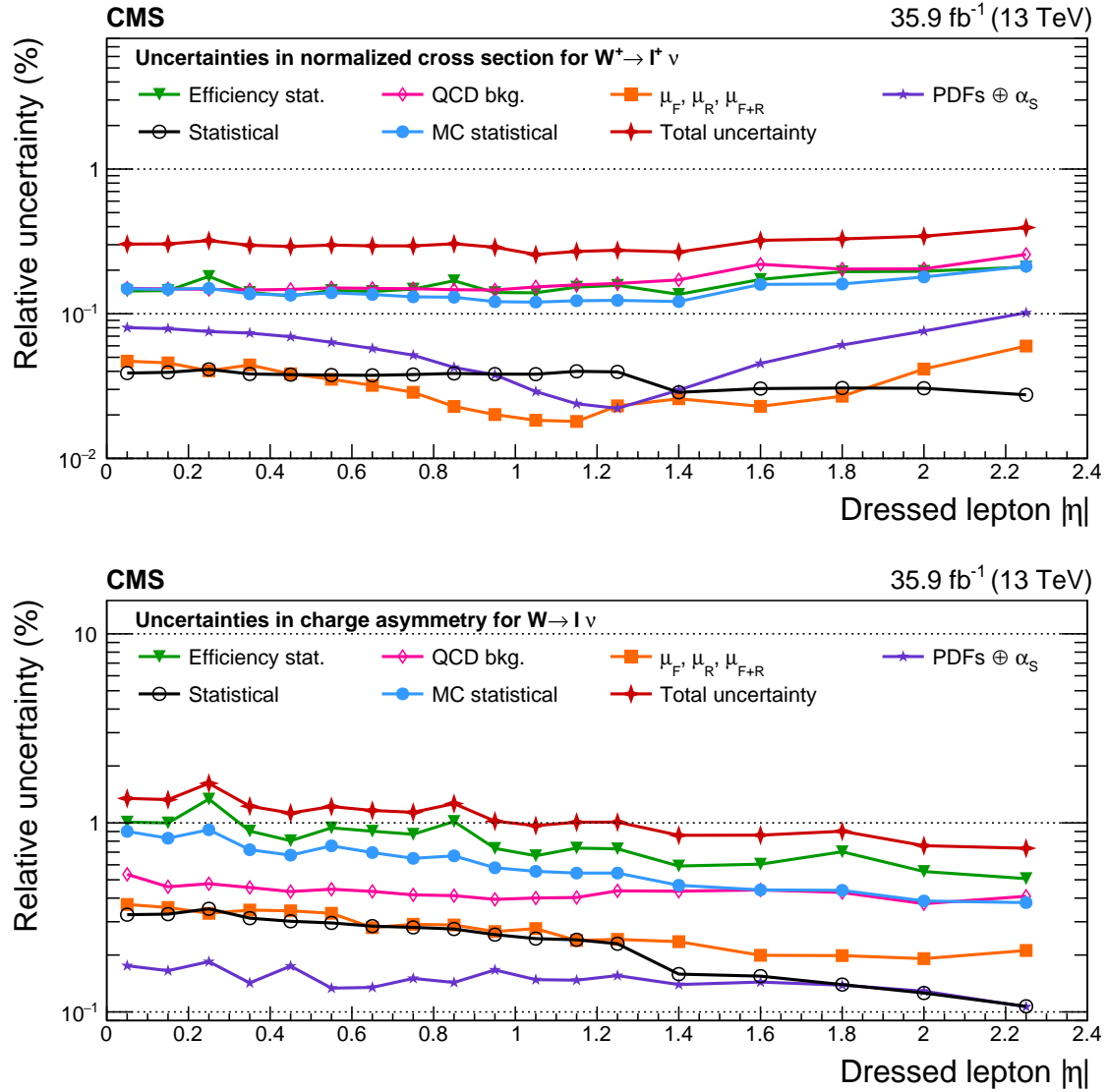


Figure 4: Upper: relative impact of groups of systematic uncertainties (as defined in the text) on the normalized cross sections for the W^+ case as functions of $|\eta^\ell|$. Lower: relative impact of uncertainties on charge asymmetry. All impacts are shown for the combination of the muon and electron channels in the double-differential cross section fit. The groups of uncertainties subleading to the ones shown are suppressed for simplicity.

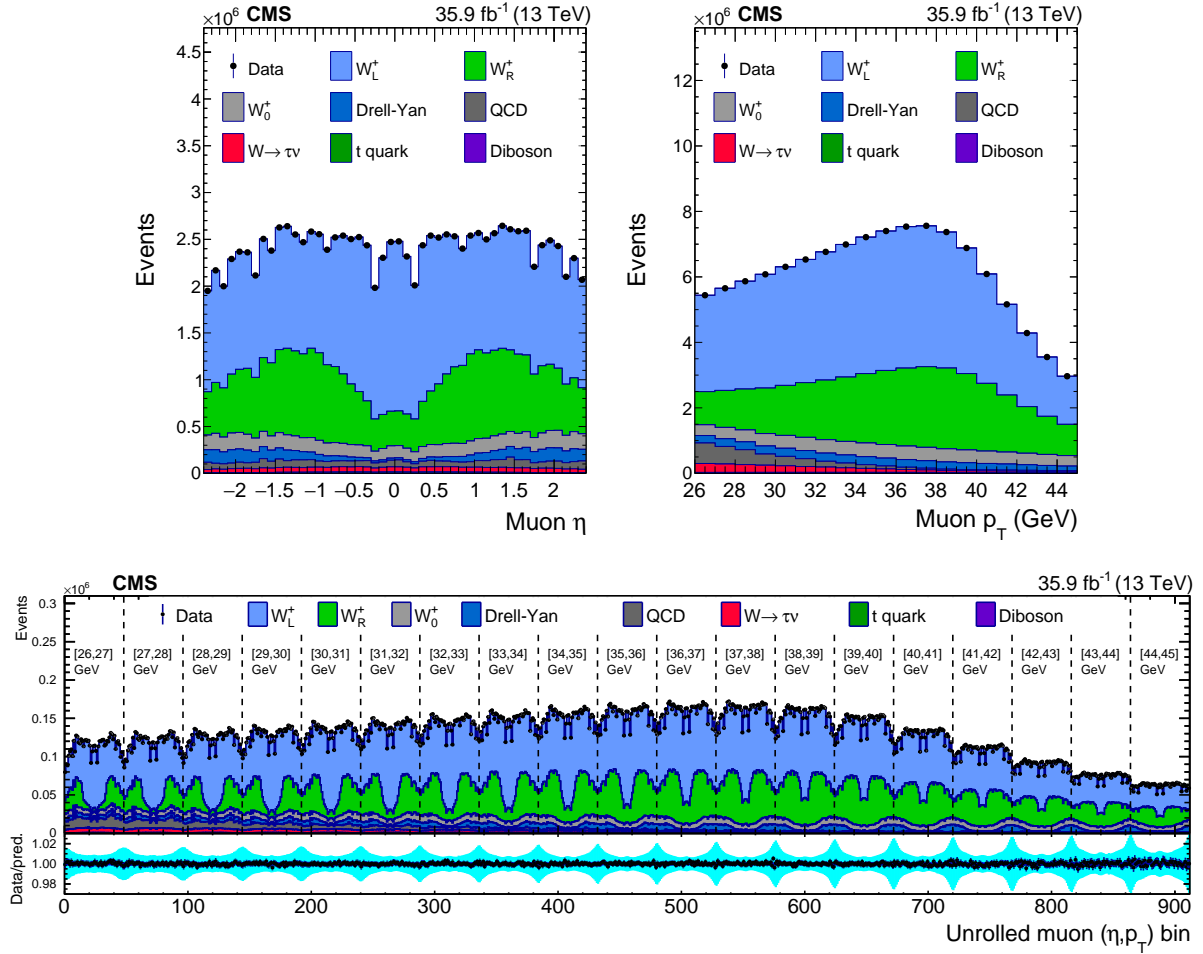


Figure 5: Distributions of η^μ (upper left), p_T^μ (upper right), and $\text{bin}_{\text{unrolled}}$ (lower) for $W^+ \rightarrow \mu^+ \nu$ events for observed data superimposed on signal plus background events. The signal and background processes are normalized to the result of the template fit. The cyan band over the data-to-prediction ratio represents the uncertainty in the total yield in each bin after the profiling process.

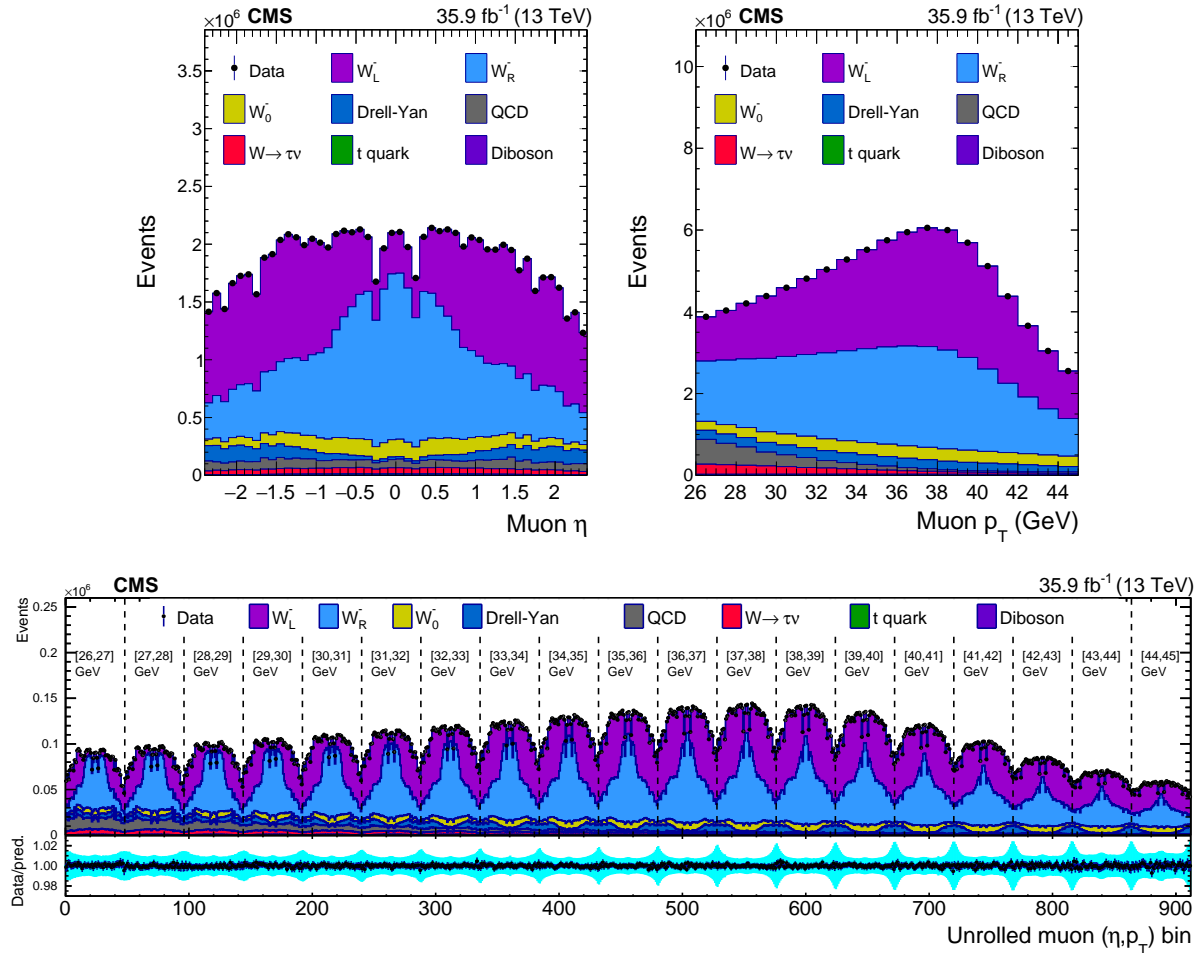


Figure 6: Distributions of η^μ (upper left), p_T^μ (upper right), and $\text{bin}_{\text{unrolled}}$ (lower) for $W^- \rightarrow \mu^- \bar{\nu}$ events for observed data superimposed on signal plus background events. The signal and background processes are normalized to the result of the template fit. The cyan band over the data-to-prediction ratio represents the uncertainty in the total yield in each bin after the profiling process.

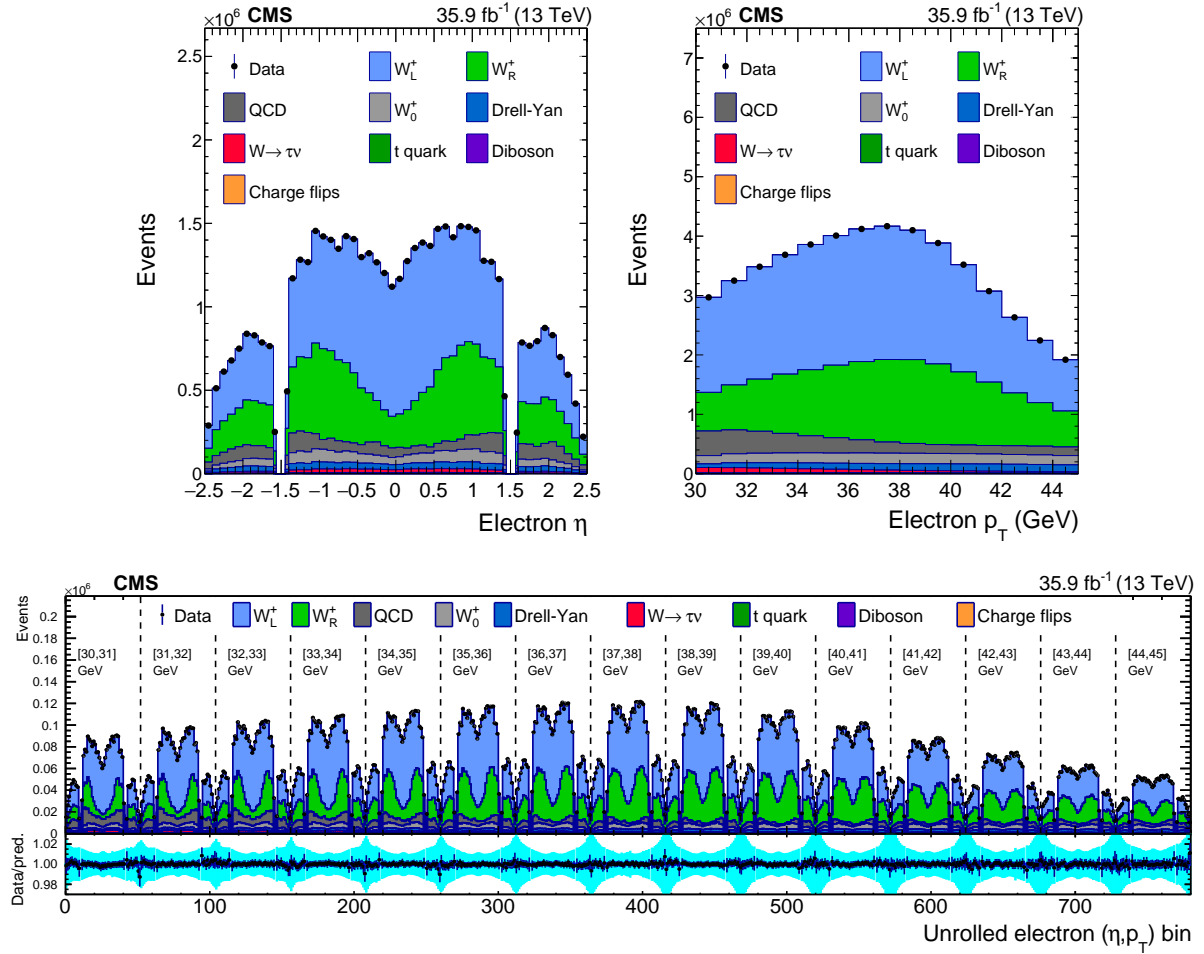


Figure 7: Distributions of η^e (upper left), p_T^e (upper right), and $\text{bin}_{\text{unrolled}}$ (lower) for $W^+ \rightarrow e^+ \nu$ events for observed data superimposed on signal plus background events. The signal and background processes are normalized to the result of the template fit. The cyan band over the data-to-prediction ratio represents the uncertainty in the total yield in each bin after the profiling process.

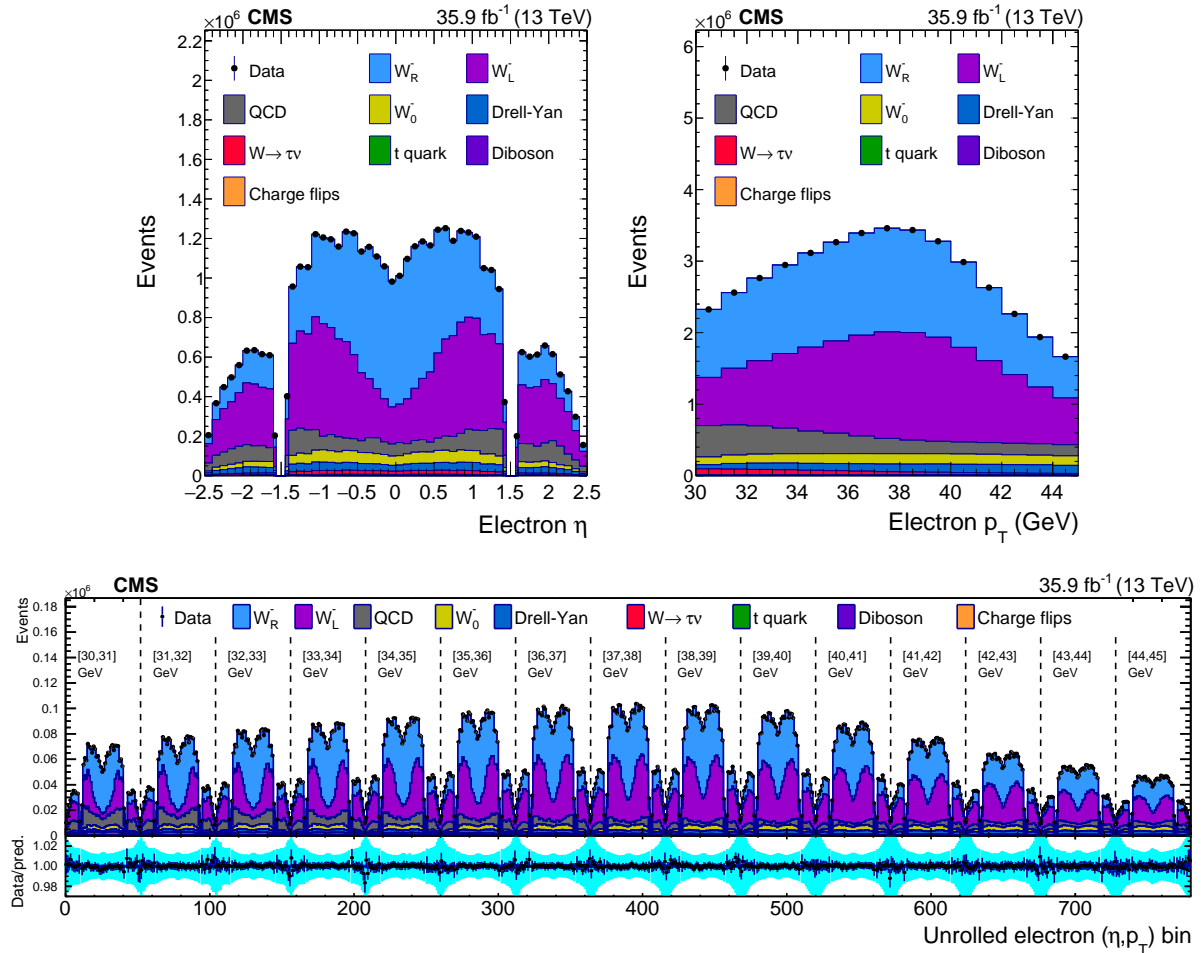


Figure 8: Distributions of η^e (upper left), p_T^e (upper right), and $\text{bin}_{\text{unrolled}}$ (lower) for $W^- \rightarrow e^- \bar{\nu}$ events for observed data superimposed on signal plus background events. The signal and background processes are normalized to the result of the template fit. The cyan band over the data-to-prediction ratio represents the uncertainty in the total yield in each bin after the profiling process.

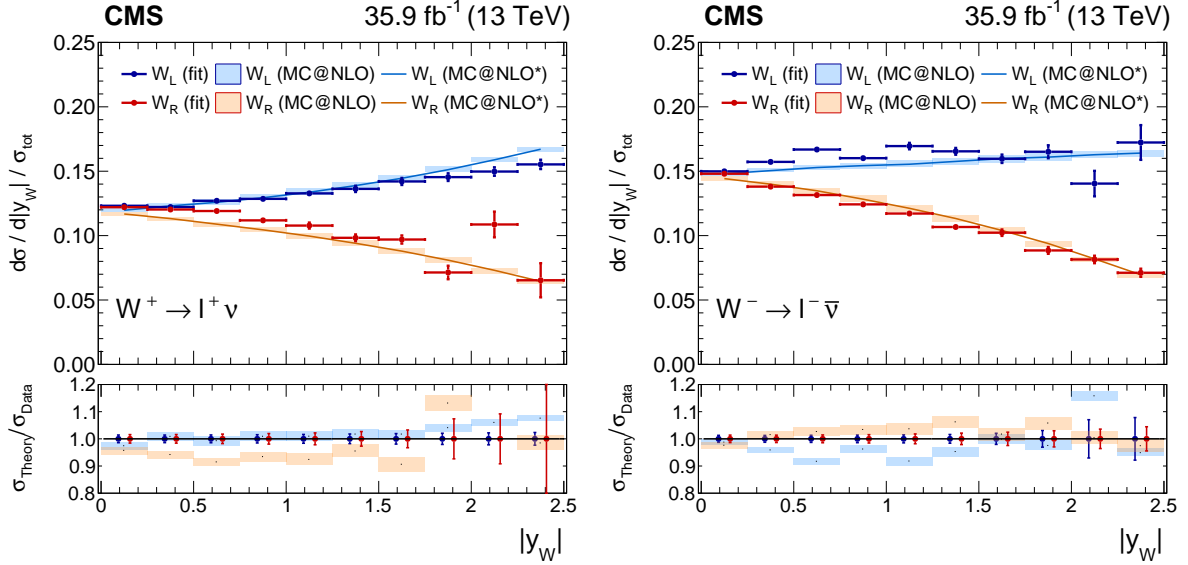


Figure 9: Measured normalized $W^+ \rightarrow \ell^+ \nu$ (left plot) or $W^- \rightarrow \ell^- \bar{\nu}$ (right plot) cross section as functions of $|y_W|$ for the left-handed and right-handed helicity states from the combination of the muon and electron channels, normalized to the total cross section. Also shown is the ratio of the prediction from MADGRAPH5_aMC@NLO to the data. The MADGRAPH5_aMC@NLO* spectrum stands for the prediction with the p_T^W weighting applied. The lightly filled band corresponds to the expected uncertainty from the PDF variations, μ_F and μ_R scales, and α_S .

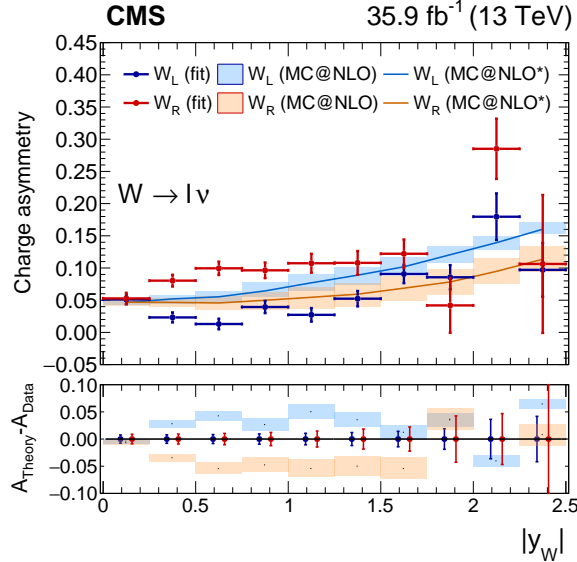


Figure 10: Measured W boson charge asymmetry as functions of $|y_W|$ for the left-handed and right-handed helicity states from the combination of the muon and electron channels. Also shown is the ratio of the prediction from MADGRAPH5_aMC@NLO to the data. The MADGRAPH5_aMC@NLO* spectrum stands for the prediction with the p_T^W weighting applied. The lightly filled band corresponds to the expected uncertainty from the PDF variations, μ_F and μ_R scales, and α_S .

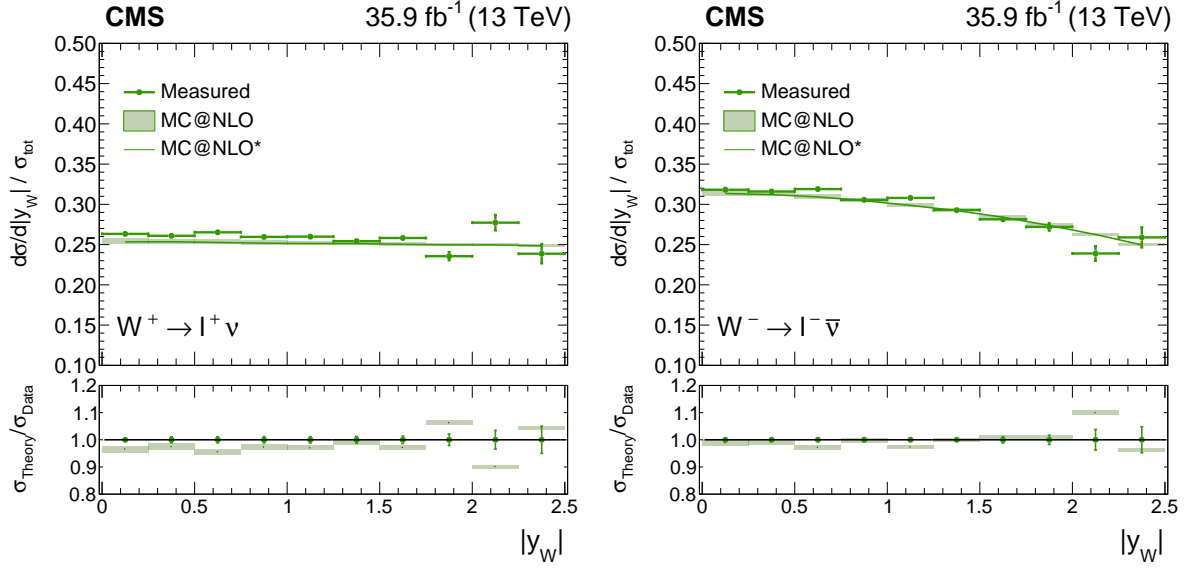


Figure 11: Measured normalized $W^+ \rightarrow \ell^+ \nu$ (left plot) and $W^- \rightarrow \ell^- \bar{\nu}$ (right plot) cross sections as a function of $|y_W|$ from the combination of the muon and electron channels, normalized to the total cross section, and integrated over the W polarization states. Also shown is the ratio of the prediction from MADGRAPH5_aMC@NLO to the data. The MADGRAPH5_aMC@NLO* spectrum stands for the prediction with the p_T^W weighting applied. The lightly filled band corresponds to the expected uncertainty from the PDF variations, μ_F and μ_R scales, and α_S .

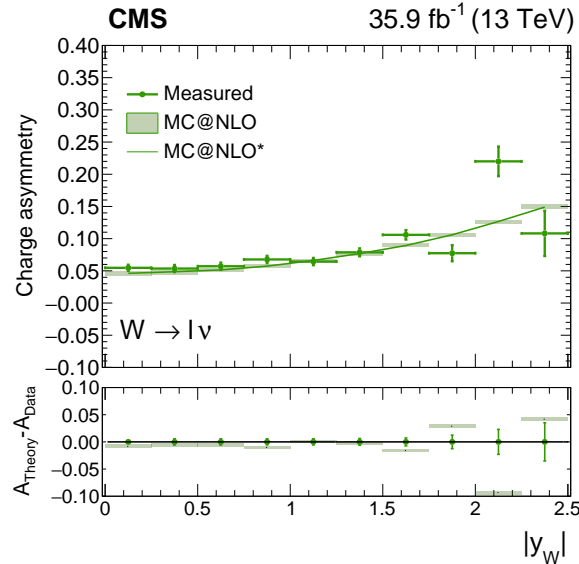


Figure 12: Measured W charge asymmetry as a function of $|y_W|$ from the combination of the muon and electron channels, integrated over the W polarization states. Also shown is the ratio of the prediction from MADGRAPH5_aMC@NLO to the data. The MADGRAPH5_aMC@NLO* spectrum stands for the prediction with the p_T^W weighting applied. The lightly filled band corresponds to the expected uncertainty from the PDF variations, μ_F and μ_R scales, and α_S .

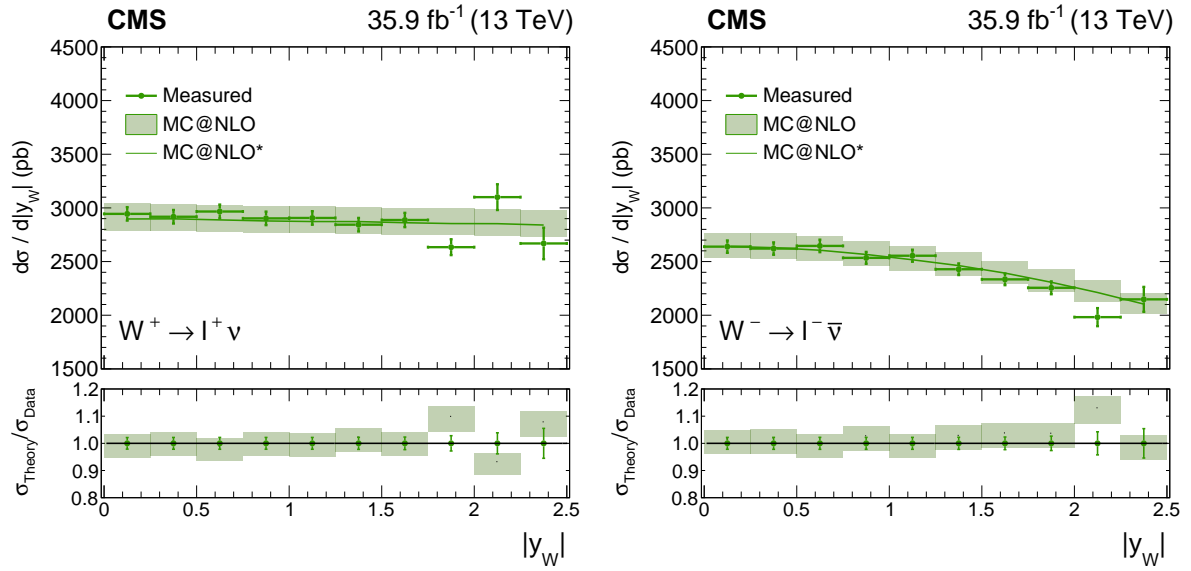


Figure 13: Measured absolute $W^+ \rightarrow \ell^+ \nu$ (left plot) or $W^- \rightarrow \ell^- \bar{\nu}$ (right plot) cross sections as functions of $|y_W|$ from the combined flavor fit. The ratio of the prediction from MADGRAPH5_aMC@NLO to the data is also shown. The MADGRAPH5_aMC@NLO* spectrum stands for the prediction with the p_T^W weighting applied. The lightly filled band corresponds to the expected uncertainty from the PDF variations, μ_F and μ_R scales, and α_S .

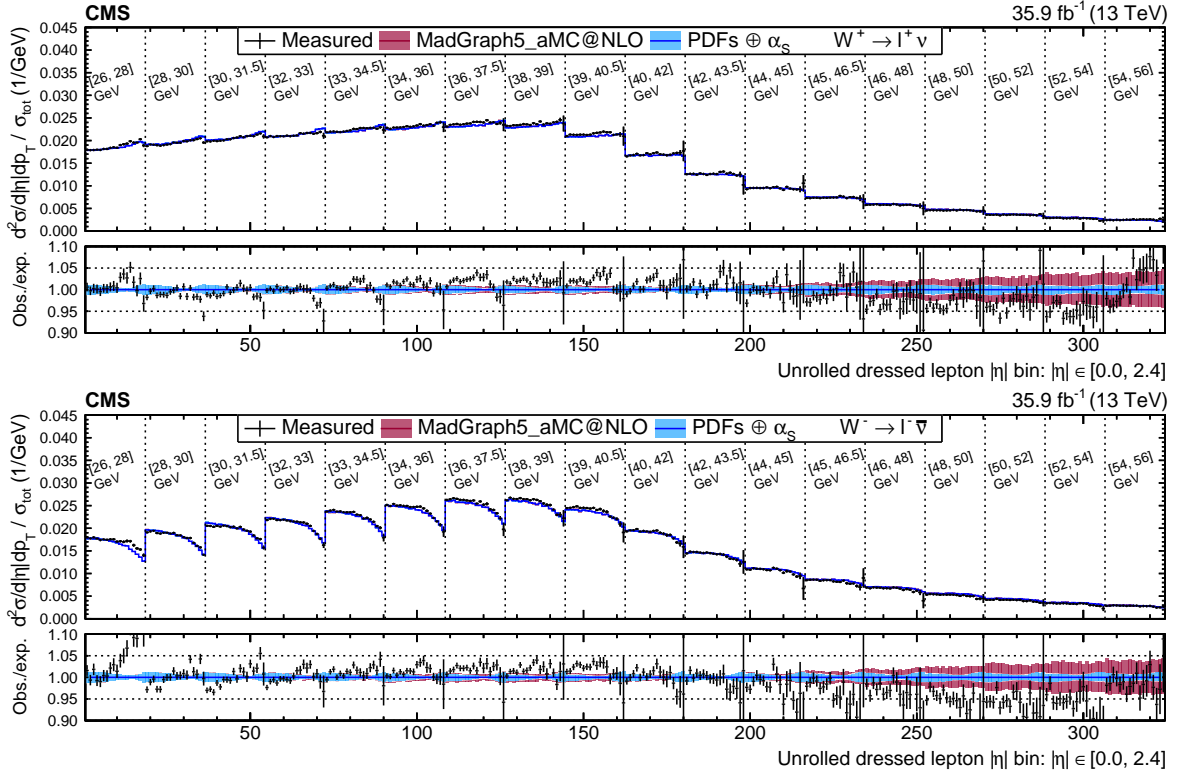


Figure 14: Normalized double-differential cross section as a function of p_T^ℓ and $|\eta^\ell|$, unrolled in a 1D histogram along $|\eta^\ell|$ for the positive (negative) charge on the upper (lower) plot. The lower panel in each plot shows the ratio of the observed and expected cross sections. The colored bands represent the prediction from MADGRAPH5_aMC@NLO with the expected uncertainty from the quadrature sum of the PDF $\oplus\alpha_S$ variations (blue) and the μ_F and μ_R scales (bordeaux).

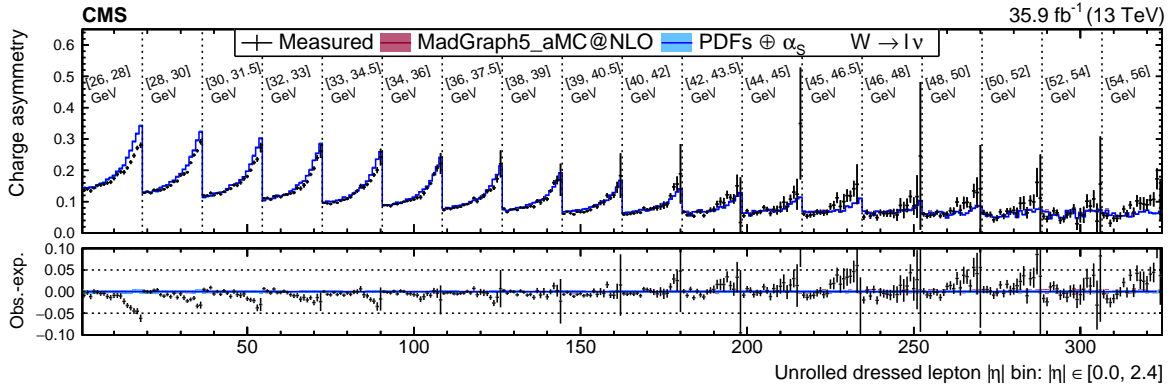


Figure 15: Double-differential W boson charge asymmetry as a function of p_T^ℓ and $|\eta^\ell|$, unrolled in a 1D histogram along $|\eta^\ell|$. The lower panel shows the difference of the observed and expected charge asymmetry. The colored bands represent the prediction from MADGRAPH5_aMC@NLO with the expected uncertainty from the quadrature sum of the PDF $\oplus\alpha_S$ variations (blue) and the μ_F and μ_R scales (bordeaux).

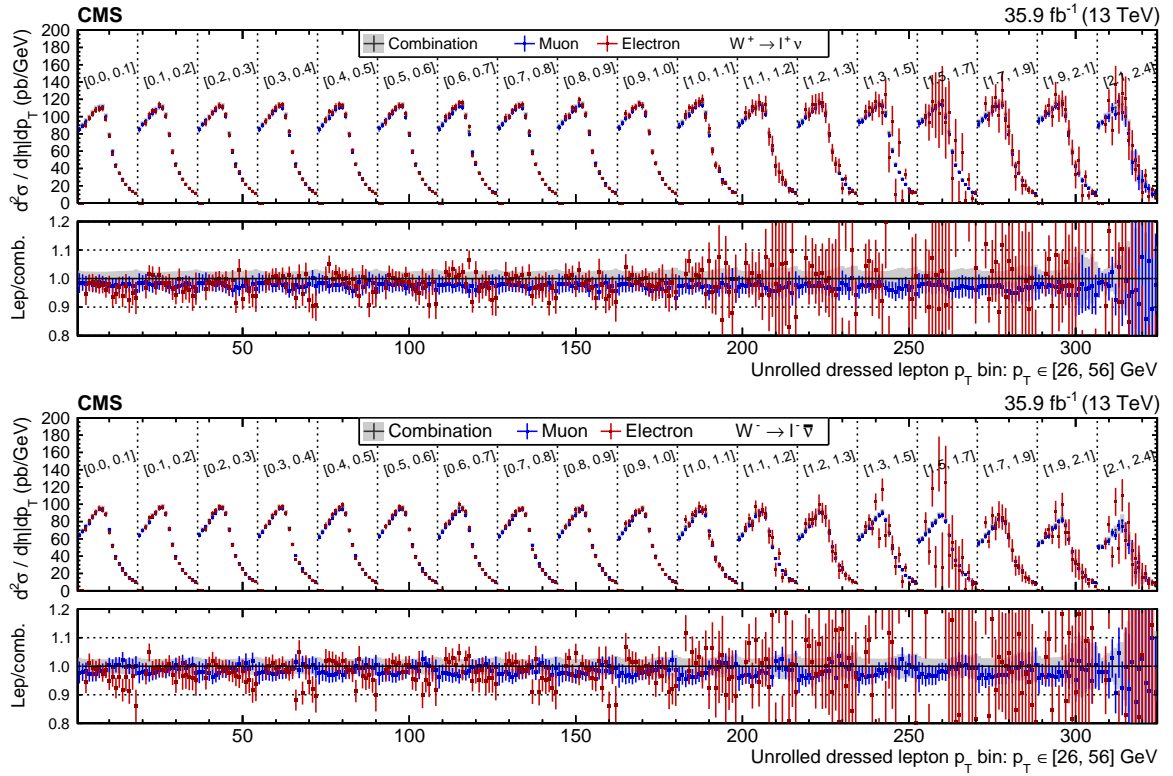


Figure 16: Absolute double-differential cross section as a function of p_T^ℓ and $|\eta^\ell|$, unrolled in a 1D histogram along p_T^ℓ in bins of $|\eta^\ell|$ for the positive (negative) charge on upper (lower) panel. The combined muon and electron fit is shown in green markers, the muon-only fit in blue markers, and the electron-only fit in red markers. The error bars correspond to the total uncertainty from the respective fits. The filled gray band in the lower panel represents the total uncertainty from the combined fit.

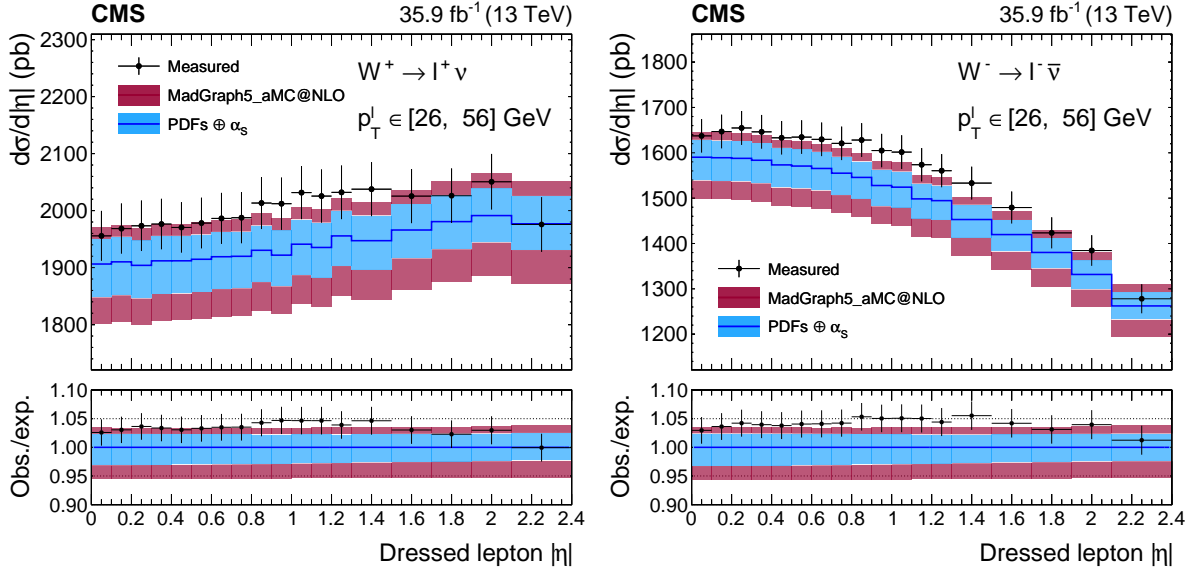


Figure 17: Absolute differential cross section as a function of $|\eta^\ell|$ for the $W^+ \rightarrow \ell^+ \nu$ (left) and $W^- \rightarrow \ell^- \bar{\nu}$ channel (right). The measurement is the result of the combination of the muon and electron channels. The lower panel in each plot shows the ratio of observed and expected cross sections. The colored bands represent the prediction from MADGRAPH5_aMC@NLO with the expected uncertainty from the quadrature sum of the $\text{PDF} \oplus \alpha_s$ variations (blue) and the μ_F and μ_R scales (bordeaux).

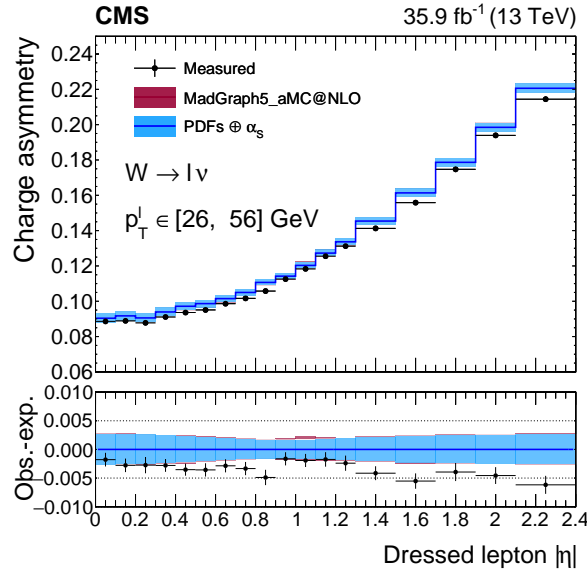


Figure 18: Absolute differential W boson charge asymmetry as a function of $|\eta^\ell|$. The measurement is the result of the combination of the muon and electron channels. The lower panel shows the difference of observed and expected charge asymmetry. The colored bands represent the prediction from MADGRAPH5_aMC@NLO with the expected uncertainty from the quadrature sum of the $\text{PDF} \oplus \alpha_s$ variations (blue) and the μ_F and μ_R scales (bordeaux).

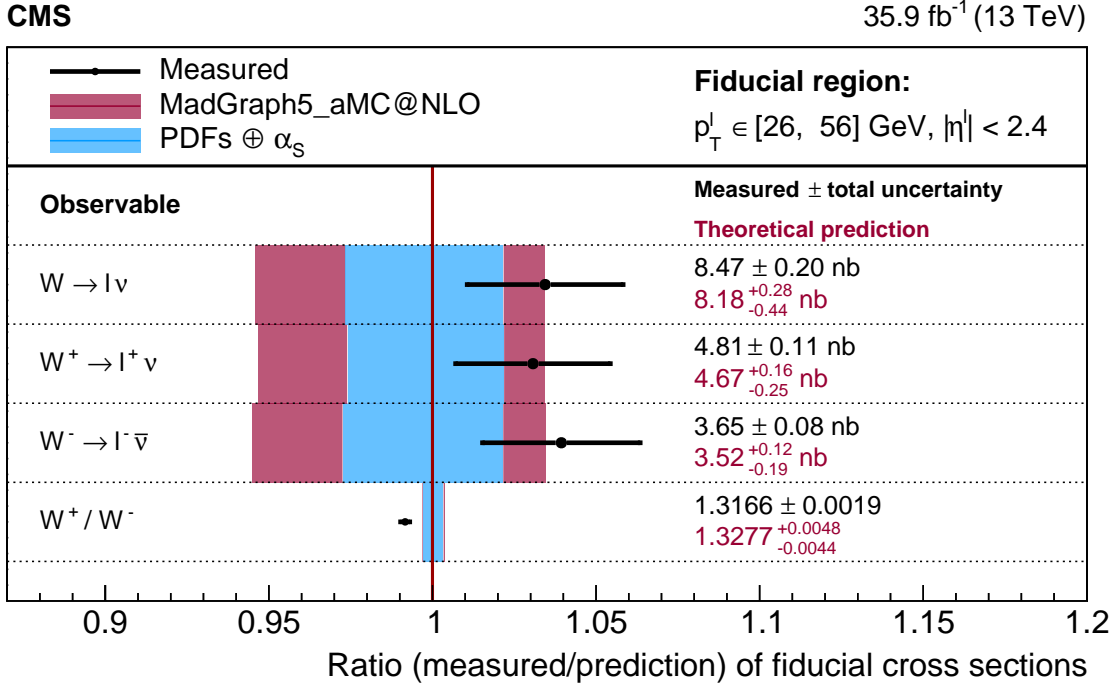


Figure 19: Ratio of the measured over predicted absolute inclusive cross section in the fiducial region $26 < p_T^\ell < 56 \text{ GeV}$ and $|\eta^\ell| < 2.5$, charge-integrated, charge-dependent, and the ratio for W^+ and W^- . The measurement is the result of the combination of the muon and electron channels. The colored bands represent the prediction from MADGRAPH5_aMC@NLO with the expected uncertainty from the quadrature sum of the PDF \oplus α_s variations (blue) and the μ_F and μ_R scales (bordeaux).

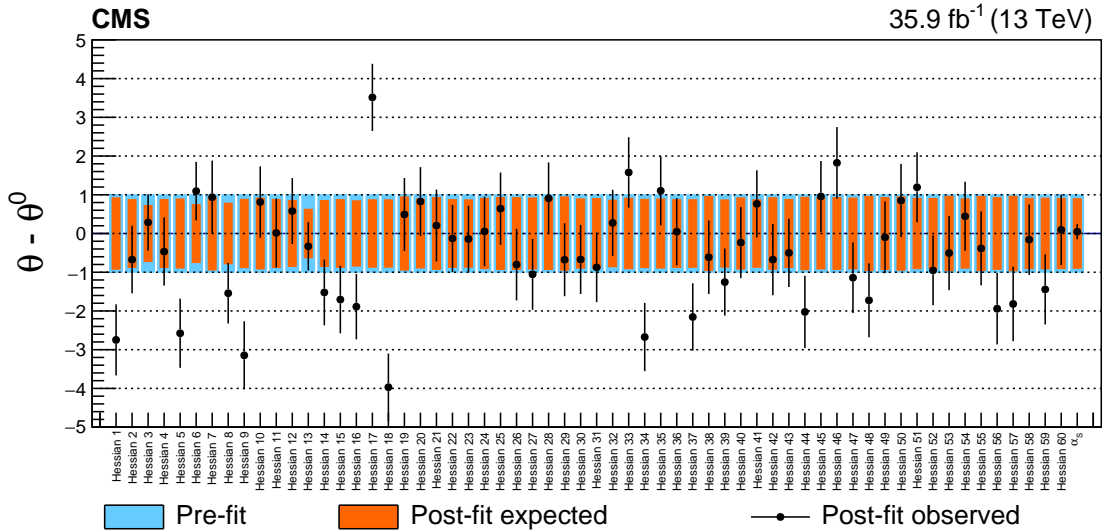


Figure 20: Pulls and constraints of the 60 Hessian variations of the NNPDF3.0 PDF set, and of the α_s parameter, from the combined fit of muon and electron channels. The underlying fit is performed by fixing the W boson cross sections to their expectation in all helicity and charge processes. The cyan band represents the input values (which all have zero mean and width one), the orange bands show the postfit expected values, and black points represent the observed pulls and constraint values.

9 Summary

The differential W boson cross sections as functions of the W boson rapidity, $|y_W|$, and for the two charges separately, $W^+ \rightarrow \ell^+ \nu$ and $W^- \rightarrow \ell^- \bar{\nu}$, are measured in the W boson helicity states. Double-differential cross sections of the W boson are measured as a function of the charged-lepton transverse momentum p_T^ℓ and absolute pseudorapidity $|\eta^\ell|$. For both W^+ and W^- bosons, the differential charge asymmetry is also extracted.

The measurement is based on data taken in proton-proton collisions at the LHC at a center-of-mass energy of $\sqrt{s} = 13$ TeV, corresponding to an integrated luminosity of 35.9 fb^{-1} . Differential cross sections are presented, both absolute and normalized to the total production cross section within a given acceptance. For the helicity measurement, the range $|y_W| < 2.5$ is presented, whereas for the double-differential cross section the range $|\eta^\ell| < 2.4$ and $26 < p_T^\ell < 56$ GeV is used. The measurement is performed using both the muon and electron channels, combined together considering all sources of correlated and uncorrelated uncertainties.

The precision in the measurement as a function of $|y_W|$, using a combination of the two channels, is about 2% in central $|y_W|$ bins and 5 to 20%, depending on the charge-polarization combination, in the outermost acceptance bins. The precision of the double-differential cross section, relative to the total, is about 1% in the central part of the detector of $|\eta^\ell| < 1$ and better than 2.5% up to $|\eta^\ell| < 2$ for each of the two W boson charges.

Charge asymmetries are also measured, differentially in $|y_W|$ and polarization, as well as in p_T^ℓ and $|\eta^\ell|$. The uncertainties in these asymmetries range from 0.1% in high-acceptance bins to roughly 2.5% in regions of phase space with lower detector acceptance. Furthermore, fiducial cross sections are presented by integrating the two-dimensional differential cross sections over the full acceptance of the analysis.

The measurement of the W boson polarized cross sections as functions of $|y_W|$ is used to constrain the parameters related to parton distribution functions in a simultaneous fit of the two channels and the two W boson charges. The constraints are derived at the detector level on 60 uncorrelated eigenvalues of the NNPDF3.0 set of PDFs within the MADGRAPH5_aMC@NLO event generator, and show a total constraint down to $\simeq 70\%$ of the prefit uncertainties for certain variations of the PDF nuisance parameters.

Acknowledgments

We congratulate our colleagues in the CERN accelerator departments for the excellent performance of the LHC and thank the technical and administrative staffs at CERN and at other CMS institutes for their contributions to the success of the CMS effort. In addition, we gratefully acknowledge the computing centers and personnel of the Worldwide LHC Computing Grid for delivering, so effectively, the computing infrastructure essential to our analyses. Finally, we acknowledge the enduring support for the construction and operation of the LHC and the CMS detector provided by the following funding agencies: the Austrian Federal Ministry of Education, Science and Research and the Austrian Science Fund; the Belgian Fonds de la Recherche Scientifique, and Fonds voor Wetenschappelijk Onderzoek; the Brazilian Funding Agencies (CNPq, CAPES, FAPERJ, FAPERGS, and FAPESP); the Bulgarian Ministry of Education and Science; CERN; the Chinese Academy of Sciences, Ministry of Science and Technology, and National Natural Science Foundation of China; the Colombian Funding Agency (COLCIENCIAS); the Croatian Ministry of Science, Education and Sport, and the Croatian Science Foundation; the Research and Innovation Foundation, Cyprus; the Secretariat for Higher

Education, Science, Technology and Innovation, Ecuador; the Ministry of Education and Research, Estonian Research Council via PRG780, PRG803 and PRG445 and European Regional Development Fund, Estonia; the Academy of Finland, Finnish Ministry of Education and Culture, and Helsinki Institute of Physics; the Institut National de Physique Nucléaire et de Physique des Particules / CNRS, and Commissariat à l'Énergie Atomique et aux Énergies Alternatives / CEA, France; the Bundesministerium für Bildung und Forschung, the Deutsche Forschungsgemeinschaft (DFG) under Germany's Excellence Strategy – EXC 2121 “Quantum Universe” – 390833306, and Helmholtz-Gemeinschaft Deutscher Forschungszentren, Germany; the General Secretariat for Research and Technology, Greece; the National Research, Development and Innovation Fund, Hungary; the Department of Atomic Energy and the Department of Science and Technology, India; the Institute for Studies in Theoretical Physics and Mathematics, Iran; the Science Foundation, Ireland; the Istituto Nazionale di Fisica Nucleare, Italy; the Ministry of Science, ICT and Future Planning, and National Research Foundation (NRF), Republic of Korea; the Ministry of Education and Science of the Republic of Latvia; the Lithuanian Academy of Sciences; the Ministry of Education, and University of Malaya (Malaysia); the Ministry of Science of Montenegro; the Mexican Funding Agencies (BUAP, CINVESTAV, CONACYT, LNS, SEP, and UASLP-FAI); the Ministry of Business, Innovation and Employment, New Zealand; the Pakistan Atomic Energy Commission; the Ministry of Science and Higher Education and the National Science Center, Poland; the Fundação para a Ciência e a Tecnologia, Portugal; JINR, Dubna; the Ministry of Education and Science of the Russian Federation, the Federal Agency of Atomic Energy of the Russian Federation, Russian Academy of Sciences, the Russian Foundation for Basic Research, and the National Research Center “Kurchatov Institute”; the Ministry of Education, Science and Technological Development of Serbia; the Secretaría de Estado de Investigación, Desarrollo e Innovación, Programa Consolidar-Ingenio 2010, Plan Estatal de Investigación Científica y Técnica y de Innovación 2017–2020, research project IDI-2018-000174 del Principado de Asturias, and Fondo Europeo de Desarrollo Regional, Spain; the Ministry of Science, Technology and Research, Sri Lanka; the Swiss Funding Agencies (ETH Board, ETH Zurich, PSI, SNF, UniZH, Canton Zurich, and SER); the Ministry of Science and Technology, Taipei; the Thailand Center of Excellence in Physics, the Institute for the Promotion of Teaching Science and Technology of Thailand, Special Task Force for Activating Research and the National Science and Technology Development Agency of Thailand; the Scientific and Technical Research Council of Turkey, and Turkish Atomic Energy Authority; the National Academy of Sciences of Ukraine; the Science and Technology Facilities Council, UK; the US Department of Energy, and the US National Science Foundation.

Individuals have received support from the Marie Curie program and the European Research Council and Horizon 2020 Grant, Contracts No. 675440, 752730, and 765710 (European Union); the Leventis Foundation; the A.P. Sloan Foundation; the Alexander von Humboldt Foundation; the Belgian Federal Science Policy Office; the Fonds pour la Formation à la Recherche dans l'Industrie et dans l'Agriculture (FRIA-Belgium); the Agentschap voor Innovatie door Wetenschap en Technologie (IWT-Belgium); the F.R.S.-FNRS and FWO (Belgium) under the “Excellence of Science – EOS” – be.h project n. 30820817; the Beijing Municipal Science & Technology Commission, Grant No. Z191100007219010; the Ministry of Education, Youth and Sports (MEYS) of the Czech Republic; the Lendület (“Momentum”) Program and the János Bolyai Research Scholarship of the Hungarian Academy of Sciences, the New National Excellence Program ÚNKP, the NKFI research Grants No. 123842, 123959, 124845, 124850, 125105, 128713, 128786, and 129058 (Hungary); the Council of Scientific and Industrial Research, India; the HOMING PLUS program of the Foundation for Polish Science, cofinanced from European Union, Regional Development Fund, the Mobility Plus program of the Ministry of Science and Higher Education, the National Science Center (Poland), Contracts No.

Harmonia 2014/14/M/ST2/00428, Opus 2014/13/B/ST2/02543, 2014/15/B/ST2/03998, and 2015/19/B/ST2/02861, Sonata-bis 2012/07/E/ST2/01406; the National Priorities Research Program by Qatar National Research Fund; the Ministry of Science and Higher Education, project No. 02.a03.21.0005 (Russia); the Tomsk Polytechnic University Competitiveness Enhancement Program and “Nauka” Project FSWW-2020-0008 (Russia); the Programa de Excelencia María de Maeztu, and the Programa Severo Ochoa del Principado de Asturias; the Thalís and Aristeia programs cofinanced by EU-ESF, and the Greek NSRF; the Rachadapisek Sompot Fund for Postdoctoral Fellowship, Chulalongkorn University, and the Chulalongkorn Academic into Its 2nd Century Project Advancement Project (Thailand); the Kavli Foundation; the Nvidia Corporation; the SuperMicro Corporation; the Welch Foundation, Contract No. C-1845; and the Weston Havens Foundation (USA).

References

- [1] S. L. Glashow, “Partial symmetries of weak interactions”, *Nucl. Phys.* **22** (1961) 579, doi:10.1016/0029-5582(61)90469-2.
- [2] S. Weinberg, “A model of leptons”, *Phys. Rev. Lett.* **19** (1967) 1264, doi:10.1103/PhysRevLett.19.1264.
- [3] A. Salam and J. C. Ward, “Electromagnetic and weak interactions”, *Phys. Lett.* **13** (1964) 168, doi:10.1016/0031-9163(64)90711-5.
- [4] J. D. Bjorken and E. A. Paschos, “Inelastic electron-proton and γ -proton scattering and the structure of the nucleon”, *Phys. Rev.* **185** (1969) 1975, doi:10.1103/PhysRev.185.1975.
- [5] ATLAS Collaboration, “Measurement of the W-boson mass in pp collisions at $\sqrt{s} = 7$ TeV with the ATLAS detector”, *Eur. Phys. J. C* **78** (2018) 110, doi:10.1140/epjc/s10052-017-5475-4, arXiv:1701.07240. [Erratum:doi:10.1140/epjc/s10052-018-6354-3].
- [6] W. J. Stirling and A. D. Martin, “Parton distribution uncertainty in the measurement of M_W in proton - anti-proton collisions”, *Phys. Lett. B* **237** (1990) 551, doi:10.1016/0370-2693(90)91223-X.
- [7] ATLAS Collaboration, “Measurement of the Drell-Yan triple-differential cross section in pp collisions at $\sqrt{s} = 8$ TeV”, *JHEP* **12** (2017) 059, doi:10.1007/JHEP12(2017)059, arXiv:1710.05167.
- [8] CMS Collaboration, “Measurement of the weak mixing angle using the forward-backward asymmetry of Drell-Yan events in pp collisions at 8 TeV”, *Eur. Phys. J. C* **78** (2018) 701, doi:10.1140/epjc/s10052-018-6148-7, arXiv:1806.00863.
- [9] CMS Collaboration, “Measurement of the differential Drell-Yan cross section in proton-proton collisions at $\sqrt{s} = 13$ TeV”, *JHEP* **12** (2019) 059, doi:10.1007/JHEP12(2019)059, arXiv:1812.10529.
- [10] CDF Collaboration, “Direct measurement of the W production charge asymmetry in $p\bar{p}$ collisions at $\sqrt{s} = 1.96$ TeV”, *Phys. Rev. Lett.* **102** (2009) 181801, doi:10.1103/PhysRevLett.102.181801, arXiv:0901.2169.

-
- [11] D0 Collaboration, “Measurement of the muon charge asymmetry in $p\bar{p} \rightarrow W+X \rightarrow \mu\nu + X$ events at $\sqrt{s} = 1.96$ TeV”, *Phys. Rev. D* **88** (2013) 091102, doi:10.1103/PhysRevD.88.091102, arXiv:1309.2591.
- [12] ATLAS Collaboration, “Precision measurement and interpretation of inclusive W^+ , W^- and Z/γ^* production cross sections with the ATLAS detector”, *Eur. Phys. J. C* **77** (2017) 367, doi:10.1140/epjc/s10052-017-4911-9, arXiv:1612.03016.
- [13] ATLAS Collaboration, “Measurement of the cross-section and charge asymmetry of W bosons produced in proton-proton collisions at $\sqrt{s} = 8$ TeV with the ATLAS detector”, *Eur. Phys. J. C* **79** (2019) 760, doi:10.1140/epjc/s10052-019-7199-0, arXiv:1904.05631.
- [14] CMS Collaboration, “Measurement of the electron charge asymmetry in inclusive W production in pp collisions at $\sqrt{s} = 7$ TeV”, *Phys. Rev. Lett.* **109** (2012) 111806, doi:10.1103/PhysRevLett.109.111806, arXiv:1206.2598.
- [15] CMS Collaboration, “Measurement of the muon charge asymmetry in inclusive $pp \rightarrow W+X$ production at $\sqrt{s} = 7$ TeV and an improved determination of light parton distribution functions”, *Phys. Rev. D* **90** (2014) 032004, doi:10.1103/PhysRevD.90.032004, arXiv:1312.6283.
- [16] CMS Collaboration, “Measurement of the differential cross section and charge asymmetry for inclusive $pp \rightarrow W^\pm + X$ production at $\sqrt{s} = 8$ TeV”, *Eur. Phys. J. C* **76** (2016) 469, doi:10.1140/epjc/s10052-016-4293-4, arXiv:1603.01803.
- [17] LHCb Collaboration, “Inclusive W and Z production in the forward region at $\sqrt{s} = 7$ TeV”, *JHEP* **06** (2012) 058, doi:10.1007/JHEP06(2012)058, arXiv:1204.1620.
- [18] LHCb Collaboration, “Measurement of forward W and Z boson production in pp collisions at $\sqrt{s} = 8$ TeV”, *JHEP* **01** (2016) 155, doi:10.1007/JHEP01(2016)155, arXiv:1511.08039.
- [19] CMS Collaboration, “Measurement of associated production of a W boson and a charm quark in proton-proton collisions at $\sqrt{s} = 13$ TeV”, *Eur. Phys. J. C* **79** (2019) 269, doi:10.1140/epjc/s10052-019-6752-1, arXiv:1811.10021.
- [20] ATLAS Collaboration, “Measurement of the production of a W boson in association with a charm quark in pp collisions at $\sqrt{s} = 7$ TeV with the ATLAS detector”, *JHEP* **05** (2014) 068, doi:10.1007/JHEP05(2014)068, arXiv:1402.6263.
- [21] LHCb Collaboration, “Study of W boson production in association with beauty and charm”, *Phys. Rev. D* **92** (2015) 052001, doi:10.1103/PhysRevD.92.052001, arXiv:1505.04051.
- [22] CDF Collaboration, “Observation of the production of a W boson in association with a single charm quark”, *Phys. Rev. Lett.* **110** (2013) 071801, doi:10.1103/PhysRevLett.110.071801, arXiv:1209.1921.
- [23] D0 Collaboration, “Measurement of the ratio of the $p\bar{p} \rightarrow W^+c^-$ jet cross section to the inclusive $p\bar{p} \rightarrow W + \text{jets}$ cross section”, *Phys. Lett. B* **666** (2008) 23, doi:10.1016/j.physletb.2008.06.067, arXiv:0803.2259.

- [24] CDF Collaboration, “Measurement of the polar-angle distribution of leptons from W boson decay as a function of the W transverse momentum in $p\bar{p}$ collisions at $\sqrt{s} = 1.8\text{TeV}$ ”, *Phys. Rev. D* **70** (2004) 032004, doi:10.1103/PhysRevD.70.032004.
- [25] D0 Collaboration, “Measurement of the angular distribution of electrons from $W \rightarrow e\nu$ decays observed in $p\bar{p}$ collisions at $\sqrt{s} = 1.8\text{TeV}$ ”, *Phys. Rev. D* **63** (2001) 072001, doi:10.1103/PhysRevD.63.072001.
- [26] ATLAS Collaboration, “Measurement of the polarisation of W bosons produced with large transverse momentum in pp collisions at $\sqrt{s} = 7\text{TeV}$ with the ATLAS experiment”, *Eur. Phys. J. C* **72** (2012) 2001, doi:10.1140/epjc/s10052-012-2001-6, arXiv:1203.2165.
- [27] CMS Collaboration, “Measurement of the polarization of W bosons with large transverse momenta in $W + \text{jets}$ events at the LHC”, *Phys. Rev. Lett.* **107** (2011) 021802, doi:10.1103/PhysRevLett.107.021802.
- [28] E. Manca, O. Cerri, N. Foppiani, and G. Rolandi, “About the rapidity and helicity distributions of the W bosons produced at LHC”, *JHEP* **12** (2017) 130, doi:10.1007/JHEP12(2017)130, arXiv:1707.09344.
- [29] CMS Collaboration, “The CMS experiment at the CERN LHC”, *JINST* **3** (2008) S08004, doi:10.1088/1748-0221/3/08/S08004.
- [30] CMS Collaboration, “The CMS trigger system”, *JINST* **12** (2017) P01020, doi:10.1088/1748-0221/12/01/P01020, arXiv:1609.02366.
- [31] J. Alwall et al., “The automated computation of tree-level and next-to-leading order differential cross sections, and their matching to parton shower simulations”, *JHEP* **07** (2014) 079, doi:10.1007/JHEP07(2014)079, arXiv:1405.0301.
- [32] P. Nason, “A new method for combining NLO QCD with shower Monte Carlo algorithms”, *JHEP* **11** (2004) 040, doi:10.1088/1126-6708/2004/11/040, arXiv:hep-ph/0409146.
- [33] S. Frixione, P. Nason, and C. Oleari, “Matching NLO QCD computations with parton shower simulations: the POWHEG method”, *JHEP* **11** (2007) 070, doi:10.1088/1126-6708/2007/11/070, arXiv:0709.2092.
- [34] S. Alioli, P. Nason, C. Oleari, and E. Re, “A general framework for implementing NLO calculations in shower Monte Carlo programs: the POWHEG BOX”, *JHEP* **06** (2010) 043, doi:10.1007/JHEP06(2010)043, arXiv:1002.2581.
- [35] T. Sjöstrand et al., “An introduction to PYTHIA 8.2”, *Comput. Phys. Commun.* **191** (2015) 159, doi:10.1016/j.cpc.2015.01.024, arXiv:1410.3012.
- [36] CMS Collaboration, “Event generator tunes obtained from underlying event and multiparton scattering measurements”, *Eur. Phys. J. C* **76** (2016) 155, doi:10.1140/epjc/s10052-016-3988-x, arXiv:1512.00815.
- [37] NNPDF Collaboration, “Parton distributions for the LHC Run II”, *JHEP* **04** (2015) 040, doi:10.1007/JHEP04(2015)040, arXiv:1410.8849.

-
- [38] CMS Collaboration, “Measurements of differential Z boson production cross sections in proton-proton collisions at $\sqrt{s} = 13$ TeV”, *JHEP* **12** (2019) 061, doi:10.1007/JHEP12(2019)061, arXiv:1909.04133.
 - [39] GEANT4 Collaboration, “GEANT4 – a simulation toolkit”, *Nucl. Instrum. Meth. A* **506** (2003) 250, doi:10.1016/S0168-9002(03)01368-8.
 - [40] CMS Collaboration, “Particle-flow reconstruction and global event description with the CMS detector”, *JINST* **12** (2017) P10003, doi:10.1088/1748-0221/12/10/P10003, arXiv:1706.04965.
 - [41] CMS Collaboration, “Muon identification and isolation efficiency on full 2016 dataset”, CMS Detector Performance Note CMS-DP-2017-007, CERN, 2017.
 - [42] CMS Collaboration, “Energy calibration and resolution of the CMS electromagnetic calorimeter in pp collisions at $\sqrt{s} = 7$ TeV”, *JINST* **8** (2013) P09009, doi:10.1088/1748-0221/8/09/P09009, arXiv:1306.2016.
 - [43] CMS Collaboration, “Performance of electron reconstruction and selection with the CMS detector in proton-proton collisions at $\sqrt{s} = 8$ TeV”, *JINST* **10** (2015) P06005, doi:10.1088/1748-0221/10/06/P06005, arXiv:1502.02701.
 - [44] CMS Collaboration, “Electron and photon performance in CMS with the full 2017 data sample and additional 2016 highlights for the CALOR 2018 conference”, Technical Report CMS-DP-2018-017, CERN, 2018.
 - [45] CMS Collaboration, “Performance of missing transverse momentum reconstruction in proton-proton collisions at $\sqrt{s} = 13$ TeV using the CMS detector”, *JINST* **14** (2019) P07004, doi:10.1088/1748-0221/14/07/P07004, arXiv:1903.06078.
 - [46] CMS Collaboration, “Measurements of inclusive W and Z cross sections in pp collisions at $\sqrt{s} = 7$ TeV”, *JHEP* **01** (2011) 080, doi:10.1007/JHEP01(2011)080, arXiv:1012.2466.
 - [47] Bern, Z. and Diana, G. and Dixon, L. J. and Cordero, F. Febres and Forde, D. and Gleisberg, T. and Höche, S. and Ita, H. and Kosower, D. A. and Maître, D. and Ozeren, K., “Left-handed W bosons at the LHC”, *Phys. Rev. D* **84** (2011) 034008, doi:10.1103/PhysRevD.84.034008, arXiv:1103.5445.
 - [48] J. C. Collins and D. E. Soper, “Angular distribution of dileptons in high-energy hadron collisions”, *Phys. Rev. D* **16** (1977) 2219, doi:10.1103/PhysRevD.16.2219.
 - [49] R. K. Ellis, W. J. Stirling, and B. R. Webber, “QCD and collider physics”, *Camb. Monogr. Part. Phys. Nucl. Phys. Cosmol.* **8** (1996) 1, doi:10.1017/CBO9780511628788.
 - [50] M. Abadi et al., “TensorFlow: Large-scale machine learning on heterogeneous systems”, 2015. Software available from tensorflow.org. <https://www.tensorflow.org/>.
 - [51] ATLAS and CMS Collaborations, LHC Higgs Combination Group, “Procedure for the LHC Higgs boson search combination in summer 2011”, technical report, CERN, 2011.
 - [52] A. Bodek et al., “Extracting muon momentum scale corrections for hadron collider experiments”, *Eur. Phys. J. C* **72** (2012) 2194, doi:10.1140/epjc/s10052-012-2194-8, arXiv:1208.3710.

- [53] B. Efron, "Bootstrap methods: Another look at the jackknife", *Ann. Statist.* **7** (1979) 1, doi:10.1214/aos/1176344552.
- [54] S. Carrazza et al., "An unbiased Hessian representation for Monte Carlo PDFs", *Eur. Phys. J. C* **75** (2015) 369, doi:10.1140/epjc/s10052-015-3590-7, arXiv:1505.06736.
- [55] M. J. Oreglia, "A study of the reactions $\psi' \rightarrow \gamma\gamma\psi$ ". PhD thesis, Stanford University, 1980. SLAC Report SLAC-R-236.
- [56] J. E. Gaiser, "Charmonium spectroscopy from radiative decays of the J/ψ and ψ' ". PhD thesis, Stanford University, 1982. SLAC Report SLAC-R-255.
- [57] CMS Collaboration, "Measurement of the lepton charge asymmetry in inclusive W production in pp collisions at $\sqrt{s} = 7$ TeV", *JHEP* **04** (2011) 050, doi:10.1007/JHEP04(2011)050, arXiv:1103.3470.
- [58] CMS Collaboration, "CMS luminosity measurements for the 2016 data taking period", Technical Report CMS-PAS-LUM-17-001, CERN, 2017.
- [59] P. Golonka and Z. Was, "PHOTOS Monte Carlo: a precision tool for QED corrections in Z and W decays", *Eur. Phys. J. C* **45** (2006) 97, doi:10.1140/epjc/s2005-02396-4, arXiv:hep-ph/0506026.
- [60] R. J. Barlow and C. Beeston, "Fitting using finite Monte Carlo samples", *Comput. Phys. Commun.* **77** (1993) 219, doi:10.1016/0010-4655(93)90005-W.
- [61] NNPDF Collaboration, "A first determination of parton distributions with theoretical uncertainties", *Eur. Phys. J. C* **79** (2019) 838, doi:10.1140/epjc/s10052-019-7364-5, arXiv:1905.04311.
- [62] NNPDF Collaboration, "Parton distributions with theory uncertainties: general formalism and first phenomenological studies", *Eur. Phys. J. C* **79** (2019) 931, doi:10.1140/epjc/s10052-019-7401-4, arXiv:1906.10698.
- [63] R. Gavin, Y. Li, F. Petriello, and S. Quackenbush, "FEWZ 2.0: A code for hadronic Z production at next-to-next-to-leading order", *Comput. Phys. Commun.* **182** (2011) 2388, doi:10.1016/j.cpc.2011.06.008, arXiv:1011.3540.
- [64] Tie-Jiun Hou and Jun Gao and T. J. Hobbs and Keping Xie and Sayipjamal Dulat and Marco Guzzi and Joey Huston and Pavel Nadolsky and Jon Pumplin and Carl Schmidt and Ibrahim Sitiwaldi and Daniel Stump and C. P. Yuan, "New CTEQ global analysis of quantum chromodynamics with high-precision data from the LHC", (2019). arXiv:1912.10053.

A Additional material

This Appendix includes the plots and figures that shall be provided as additional material in addition to those already featured in the body of the text.

A.1 Helicity and rapidity analysis

Figure A.1 shows the absolute polarized cross sections as functions of $|y_W|$ from the combined muon and electron fit for both charges of the W boson.

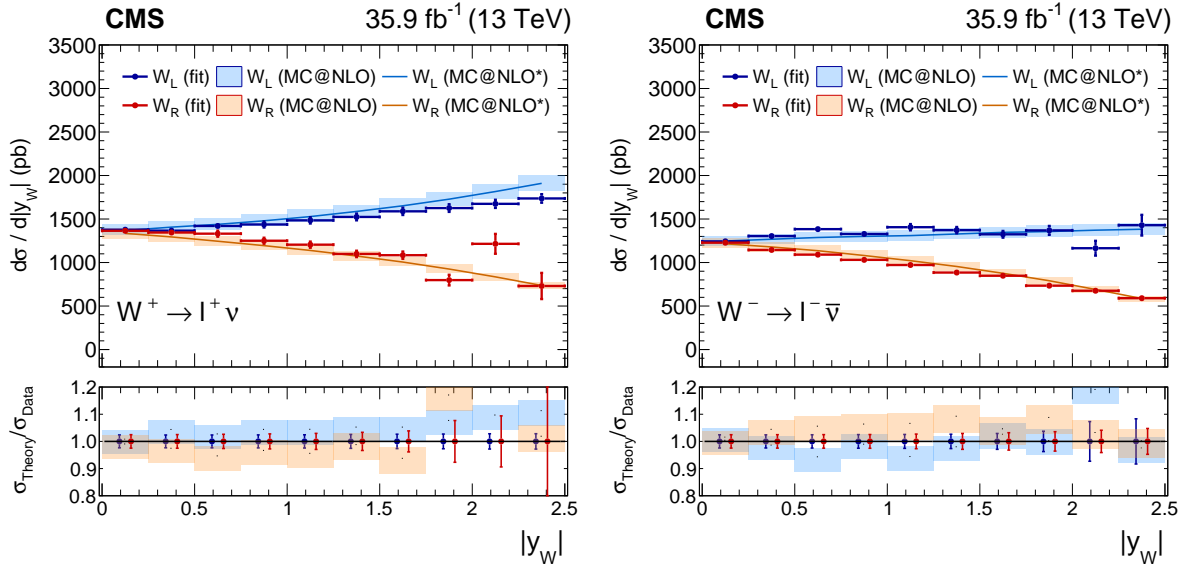


Figure A.1: Measured absolute $W^+ \rightarrow \ell^+ \nu$ (left) and $W^- \rightarrow \ell^- \bar{\nu}$ (right) cross section as a function of $|y_W|$ for the left-handed and right-handed helicity states from the combination of muon and electron channels. The ratio of the prediction from MADGRAPH5_aMC@NLO to the data is also shown. The lightly-filled band corresponds to the expected uncertainty from the PDF variations, μ_F and μ_R scales, and α_S .

Figures A.2 and A.3 show again the absolute unpolarized cross sections as functions of the W boson rapidity for the positively and negatively charged W bosons. These figures, however, also show the comparison between the two lepton flavors, i.e., performing the fits separately once in the muon-only, once in the electron-only, and once in the flavor combination shows the experimental agreement of the different flavor channels. We show that the single-flavor fits agree within their uncertainty with each other, as well as with the combined-flavor fit. The correlation structure of the three different fits cannot be trivially displayed in the ratios of the flavors shown in the lower panels of Figs. A.2 and A.3.

The comparison of the measured unpolarized W boson charge asymmetry as a function of $|y_W|$ with the prediction from another matrix-element generator, FEWZ 2.0 [63], is shown in Fig. A.4. The calculation is coupled with either the NNPDF3.1 NNLO PDF set or the CT18 [64] NNLO PDF set.

Figures A.5 and A.6 show the distribution of the A_4 coefficient extracted as a function of $|y_W|$ from the combined fit to the muon and electron channels for the positively and negatively charged W bosons, respectively.

Figure A.7 shows the correlation coefficients between the different signal processes split into their helicity components from the combined muon and electron channel fit for the two charges

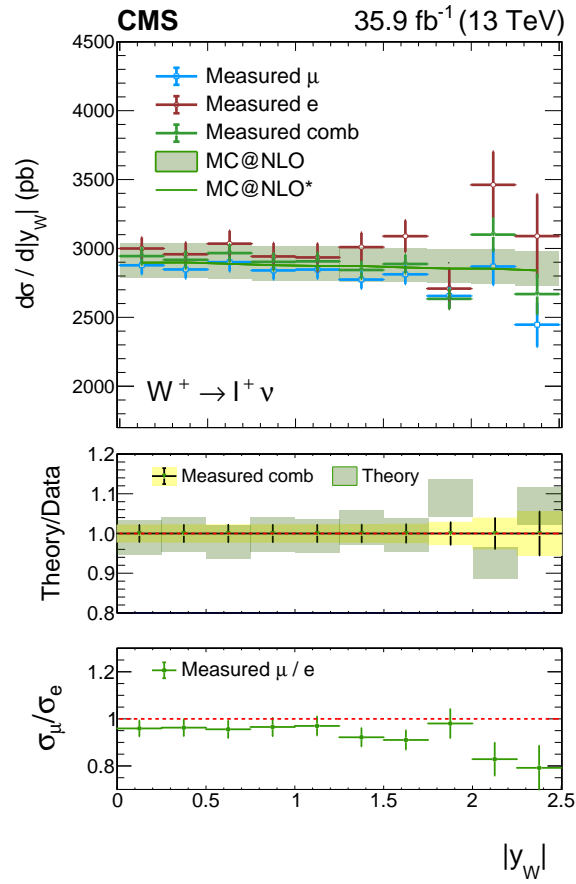


Figure A.2: Measured absolute $W^+ \rightarrow \ell^+ \nu$ cross section as a function of $|y_W|$ from three distinct fits: the combination of muon and electron channels (green), the muon-only fit (blue), and the electron-only fit (red). The ratio of the prediction from MADGRAPH5_aMC@NLO to the data is also shown. The lightly-filled band corresponds to the expected uncertainty from the PDF variations, μ_F and μ_R scales, and α_S .

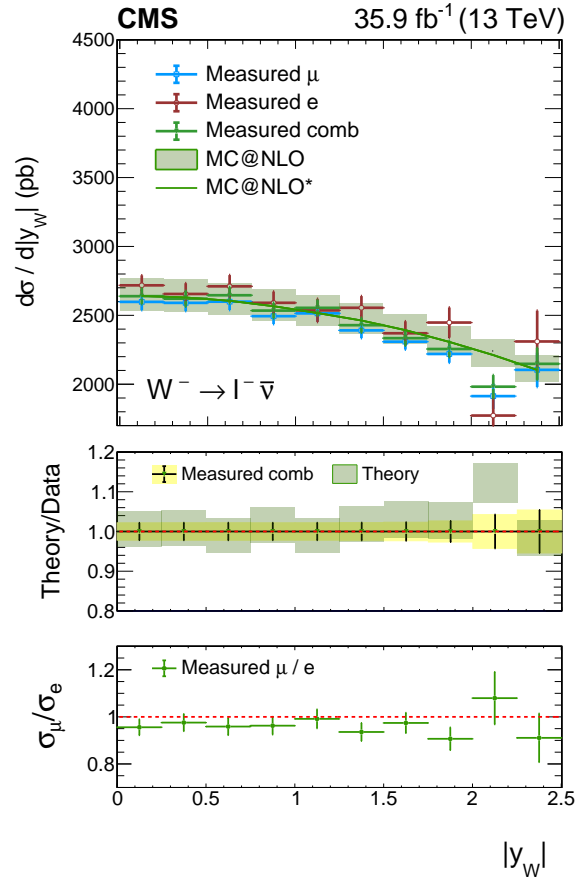


Figure A.3: Measured absolute $W^- \rightarrow \ell^- \bar{\nu}$ cross section as a function of $|y_W|$ from three distinct fits: the combination of muon and electron channels (green), the muon-only fit (blue), and the electron-only fit (red). The ratio of the prediction from MADGRAPH5_aMC@NLO to the data is also shown. The lightly-filled band corresponds to the expected uncertainty from the PDF variations, μ_F and μ_R scales, and α_S .

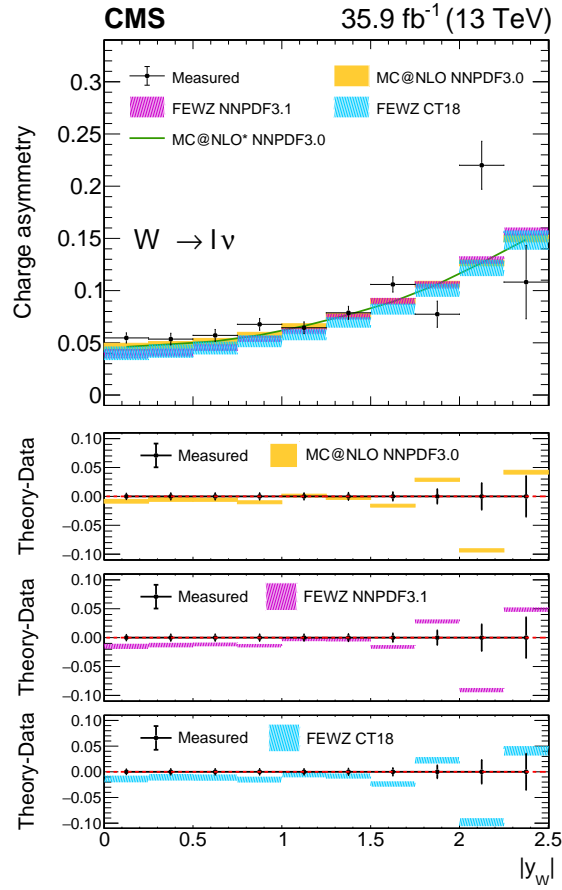


Figure A.4: Measured W boson charge asymmetry as a function of $|y_W|$ from the combination of the muon and electron channels (black dots), compared with different theoretical predictions. The yellow band represents the default generator used in this analysis, MADGRAPH5_aMC@NLO with NNPDF3.0 PDF set, the pink band represents the FEWZ generator with NNPDF3.1 PDF set, and the cyan band represents the FEWZ generator with CT18 PDF set. The uncertainty bands of the prediction include PDF uncertainties only, which are dominant with respect to α_s or QCD scale variations for this quantity.

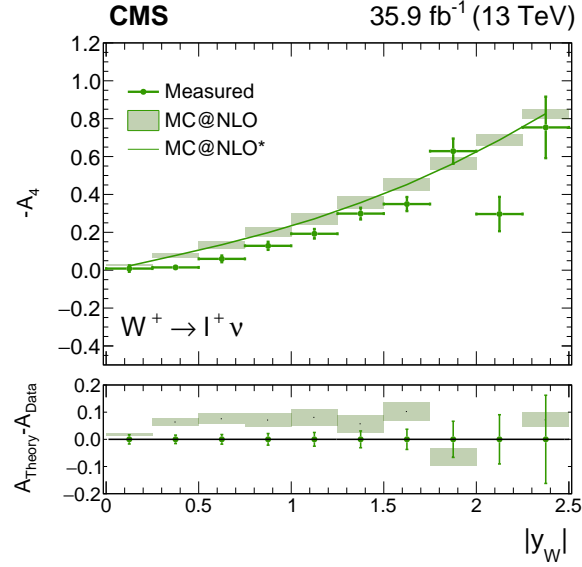


Figure A.5: Measured A_4 coefficient for $W^+ \rightarrow \ell^+ \nu$ extracted from the fit of the polarized cross sections to the combined muon and electron channel fit. Note that A_4 is negative in this case, and the plotted quantity is $-A_4$. The difference between the prediction from MADGRAPH5_aMC@NLO and the measured values is also shown. The lightly-filled band corresponds to the expected uncertainty from the PDF variations, μ_F and μ_R scales, and α_S .

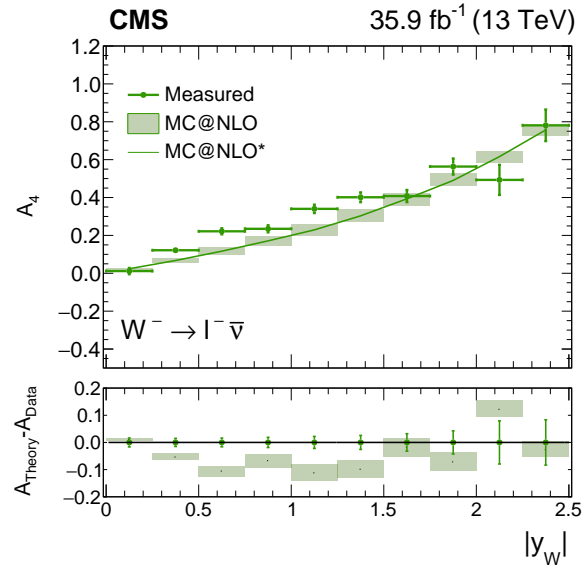


Figure A.6: Measured A_4 coefficient for $W^- \rightarrow \ell^- \bar{\nu}$ extracted from the fit of the polarized cross sections to the combined muon and electron channel fit. The difference between the prediction from MADGRAPH5_aMC@NLO and the measured values is also shown. The lightly-filled band corresponds to the expected uncertainty from the PDF variations, μ_F and μ_R scales, and α_S .

of the W boson. The numbering corresponds to the bins in $|y_W|$ of width 0.25 starting at zero. It is worthwhile to note here that the correlations of neighboring bins in rapidity are large, especially for each helicity. There are also nontrivial correlations across the helicity states.

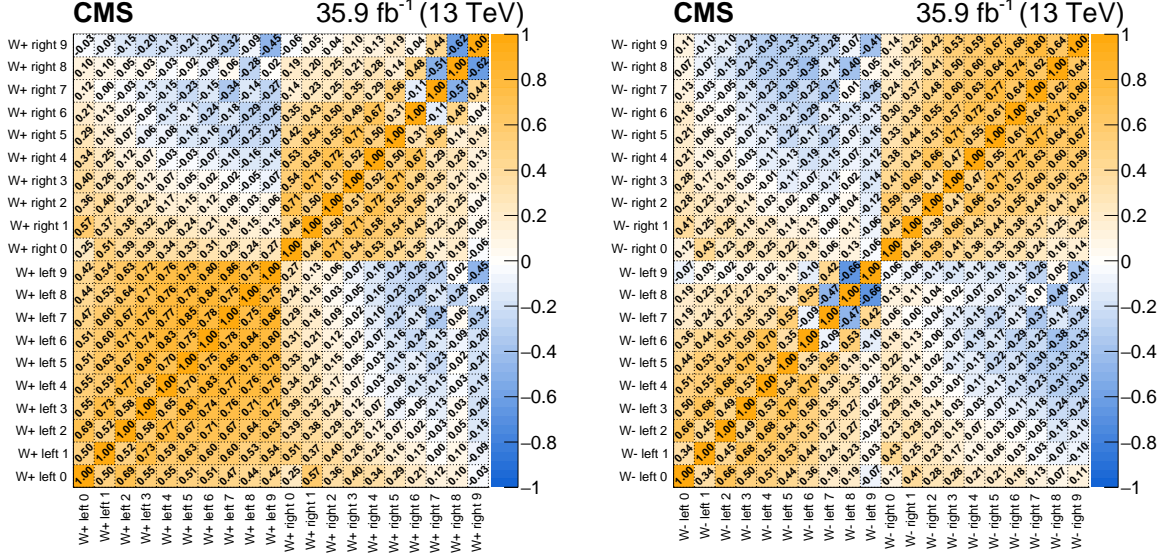


Figure A.7: Correlation coefficients between the helicity-dependent signal cross sections for $W^+ \rightarrow \ell^+ \nu$ (left) and $W^- \rightarrow \ell^- \bar{\nu}$ (right) extracted from the fit to the combined muon and electron channel fit.

Figure A.8 shows the correlation coefficients between the different PDF nuisance parameters in the combined muon and electron channel fit. The numbering of the PDF nuisances derives from the conversion of the NNPDF3.0 replicas to 60 orthogonal Hessian nuisance parameters and carries no physical meaning.

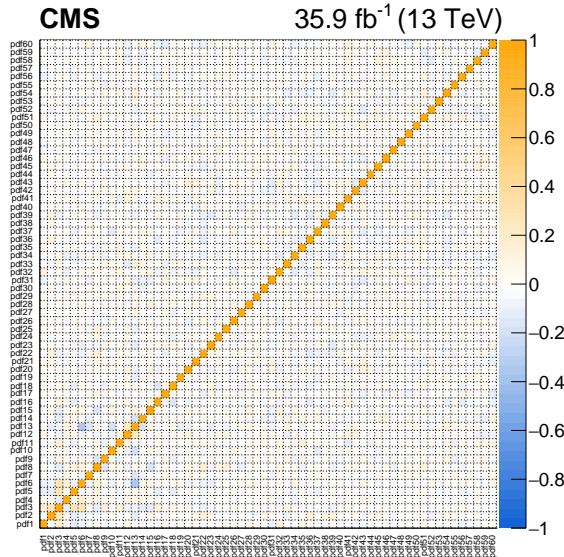


Figure A.8: Correlation coefficients between the 60 PDF nuisance parameters extracted from the fit to the combined muon and electron channel fit. The underlying fit is performed by fixing the W boson cross sections to their expectation in all helicity and charge processes.

Figure A.9 shows the post-fit pulls and their post-fit constraints of the nuisance parameters

associated with the μ_F and μ_R scale systematic uncertainties. The numbering corresponds to the bins in the p_T^W spectrum in increasing order. The numbers result from the combined fit to the muon and electron channels.

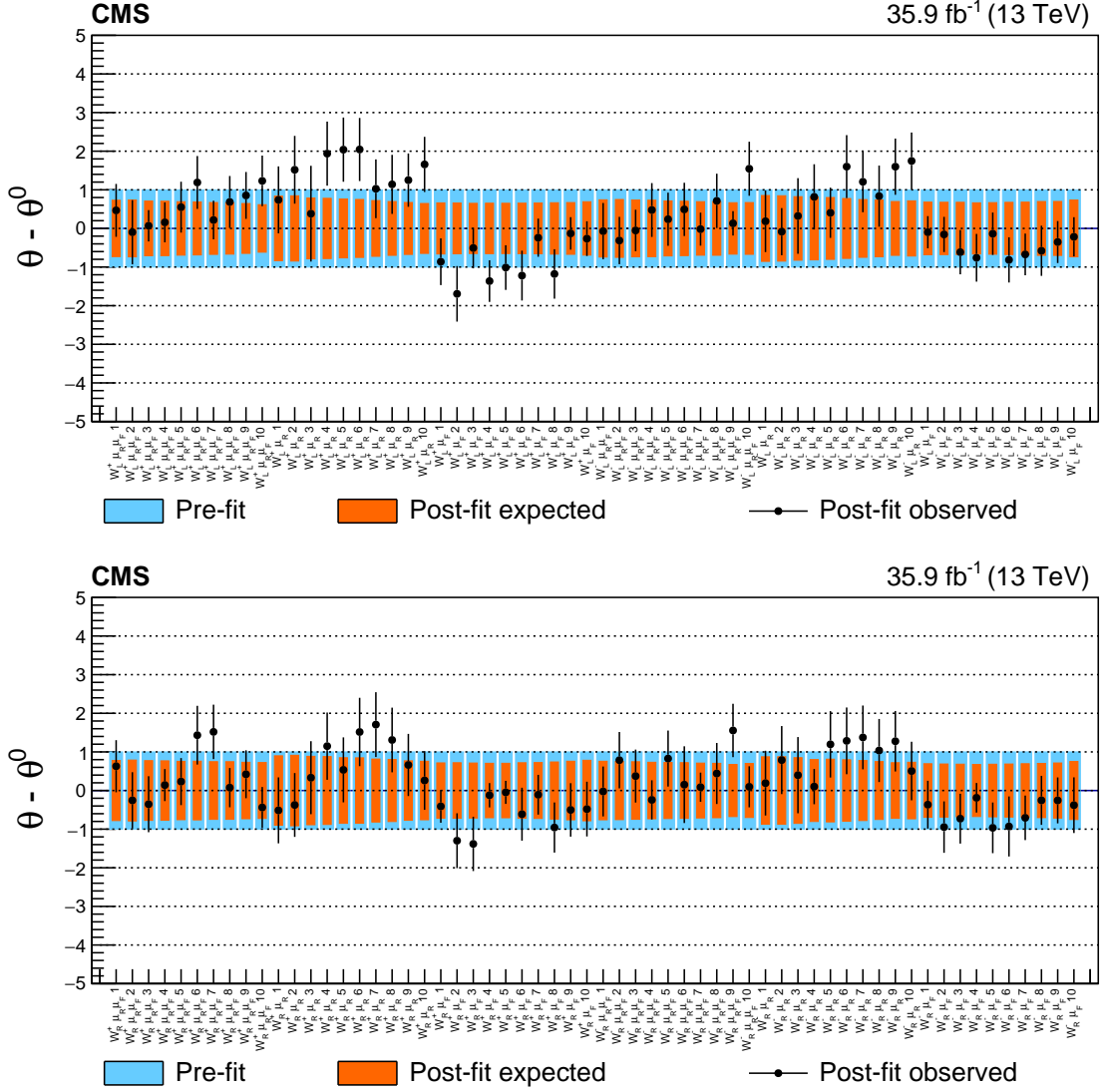


Figure A.9: Post-fit pulls and constraints of the nuisance parameters associated with the μ_F and μ_R scale systematic uncertainties. The numbering refers to bins in the p_T^W spectrum in increasing order. The nuisance parameters applied to the “left” polarization are shown on the upper panel while the ones associated with the “right” polarization are shown on the lower panel.

Figure A.10 shows the impacts of the nuisance parameter groups on the normalized polarized cross sections for W_R^+ , W_L^+ , and W_R^- .

Figure A.11 shows the impacts of the nuisance parameter groups on the absolute polarized cross sections for left-, and right-handed W bosons of positive charge. Figure A.12 shows the same impacts for negatively charged W bosons.

Figure A.13 shows the impacts of the nuisance parameter groups on the charge asymmetry for W_R bosons.

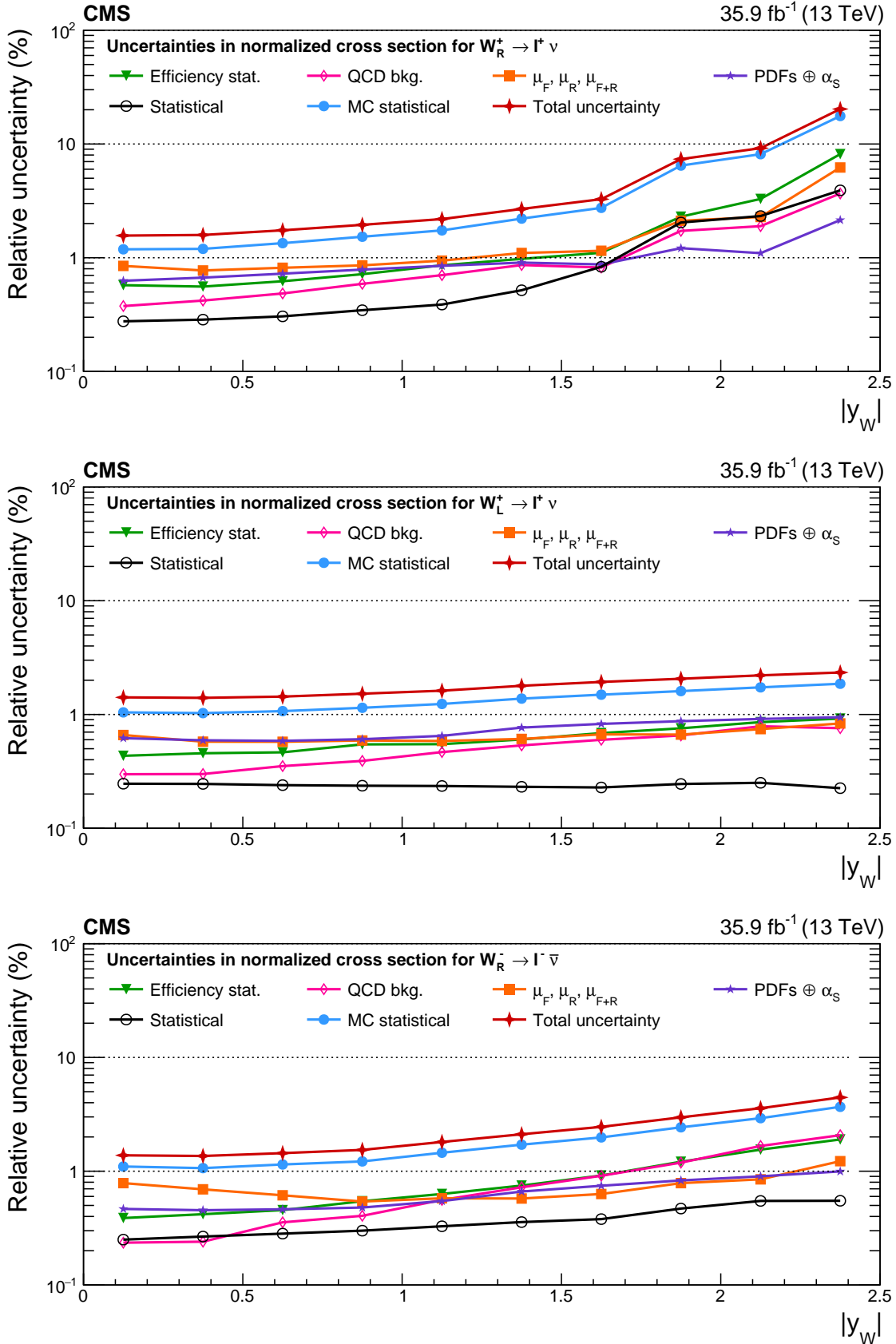


Figure A.10: Remaining impacts on the normalized polarized cross sections as functions of the W boson rapidity. Shown are the impacts of the nuisance groups for W_R^+ (upper), W_L^+ (middle), and W_R^- (lower) bosons in the helicity fit. The groups of uncertainties subleading to the ones shown are suppressed for simplicity.

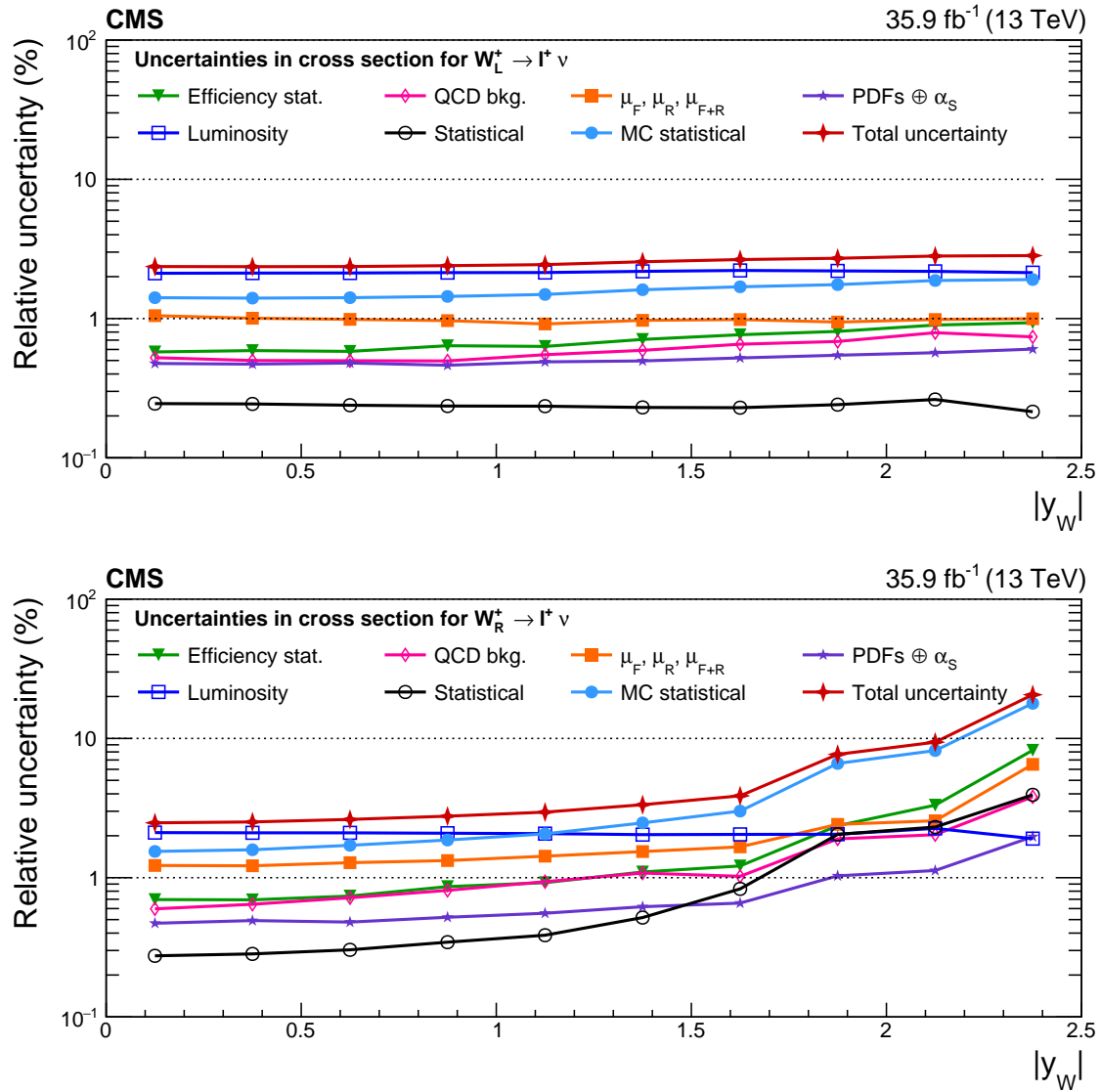


Figure A.11: Impacts on the absolute polarized cross sections as functions of the W boson rapidity. Shown are the impacts of the nuisance groups for W_L^+ (upper) and W_R^+ (lower) in the helicity fit. The groups of uncertainties subleading to the ones shown are suppressed for simplicity.

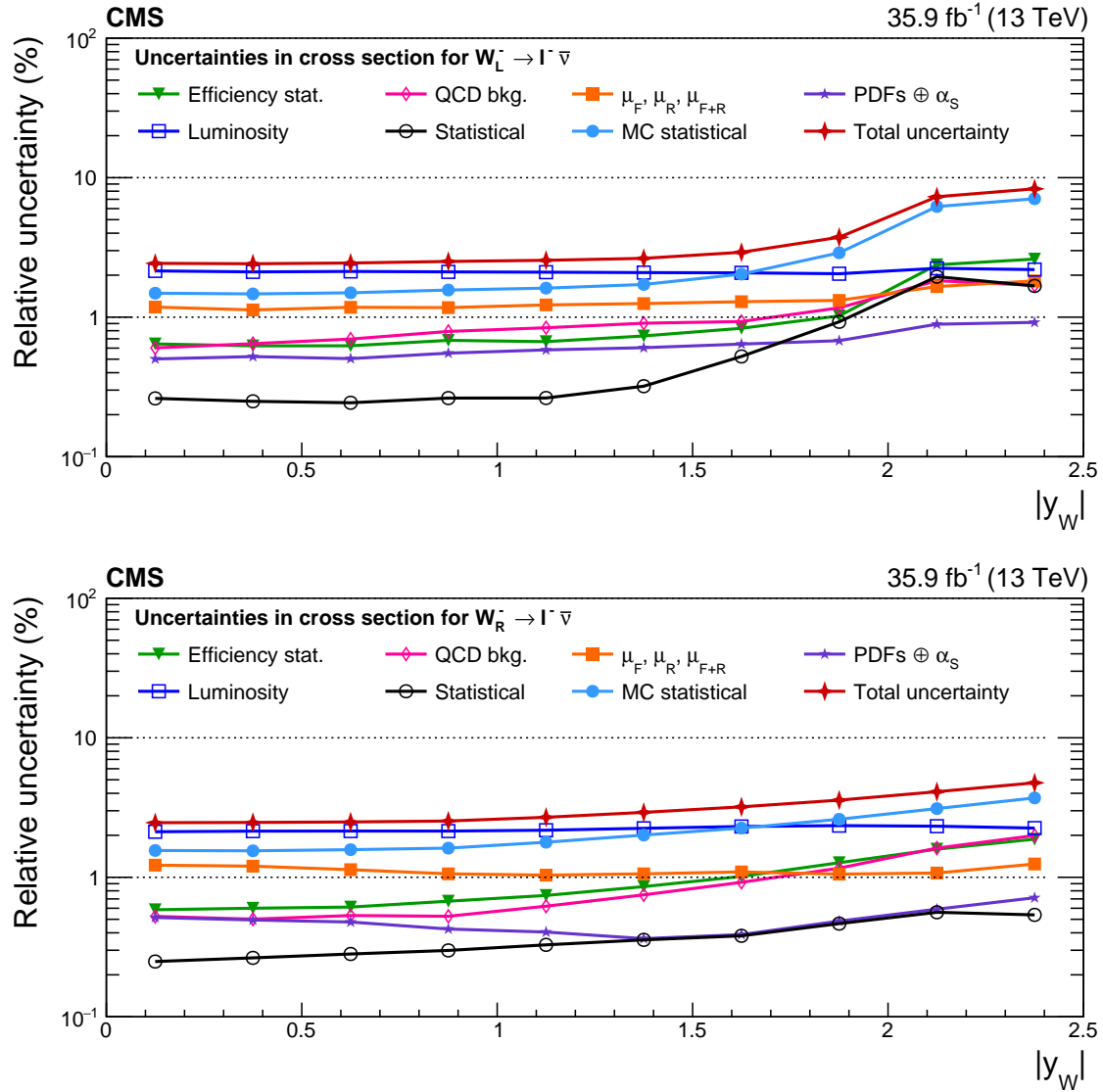


Figure A.12: Impacts on the absolute polarized cross sections as functions of the W boson rapidity. Shown are the impacts of the nuisance groups for W_L^- (upper) and W_R^- (lower) bosons in the helicity fit. The groups of uncertainties subleading to the ones shown are suppressed for simplicity.

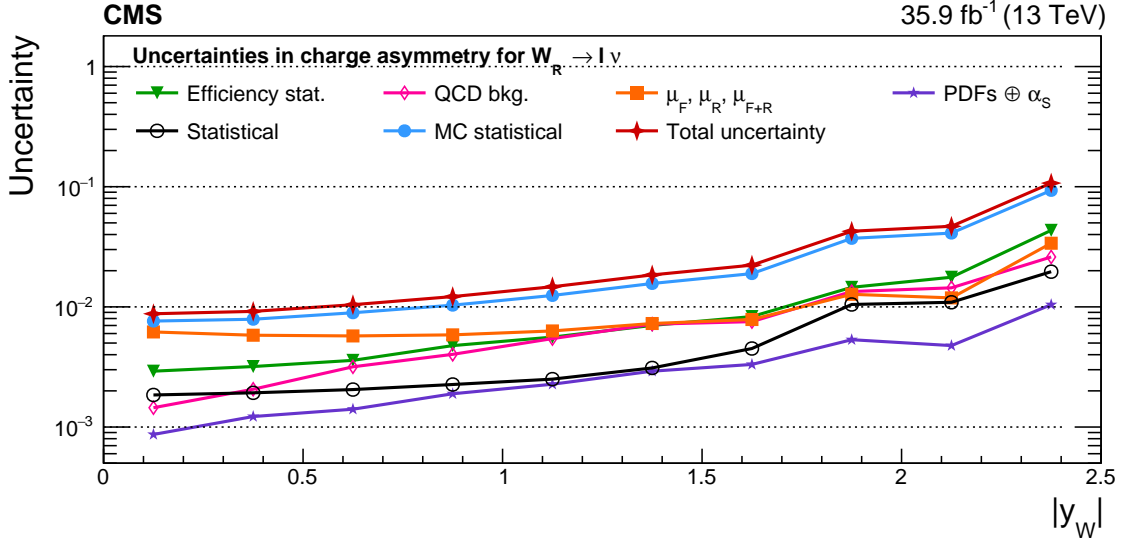


Figure A.13: Impacts on the charge asymmetry as functions of the W boson rapidity for W_R bosons in the helicity fit. The groups of uncertainties subleading to the ones shown are suppressed for simplicity.

Figure A.14 shows the impacts of the nuisance parameter groups on the unpolarized absolute W boson cross sections as a function of $|y_W|$ for both charges and the charge asymmetry. Figure A.15 shows the same impacts for the normalized W production cross sections.

Figure A.16 shows the impacts of the nuisance parameter groups on the A_4 coefficient as a function of $|y_W|$ for both charges of the W boson.

A.2 2D differential cross section

Figure A.17 shows the absolute cross sections for the combined muon and electron channel fit unrolled along p_T^ℓ , in bins of $|\eta^\ell|$ for both charges of the W boson. Figure A.18 and A.20 shows these same absolute cross sections and charge asymmetry, but integrated over all the bins in $|\eta^\ell|$.

Figures A.19 and A.21 show the normalized differential cross sections for both charges of the W boson as a function of p_T^ℓ and $|\eta^\ell|$, respectively. The charge asymmetry as a function of p_T^ℓ is also shown in Fig. A.19.

Figures A.22- A.25 show the remaining impacts of the 2D differential cross sections analysis, which were omitted in the main paper: the impacts on the normalized W cross sections as a function of $|\eta^\ell|$ for W bosons with negative charge in Fig. A.22; the impacts on the absolute cross sections for both charges as a function of p_T^ℓ in Fig. A.23; the impacts on the normalized W boson production cross sections as a function of p_T^ℓ for both charges, along with the impacts on the charge asymmetry, in Fig. A.24; and, finally, the impacts on the absolute W boson production cross sections as a function of p_T^ℓ , for both charges of the W boson in Fig. A.25.

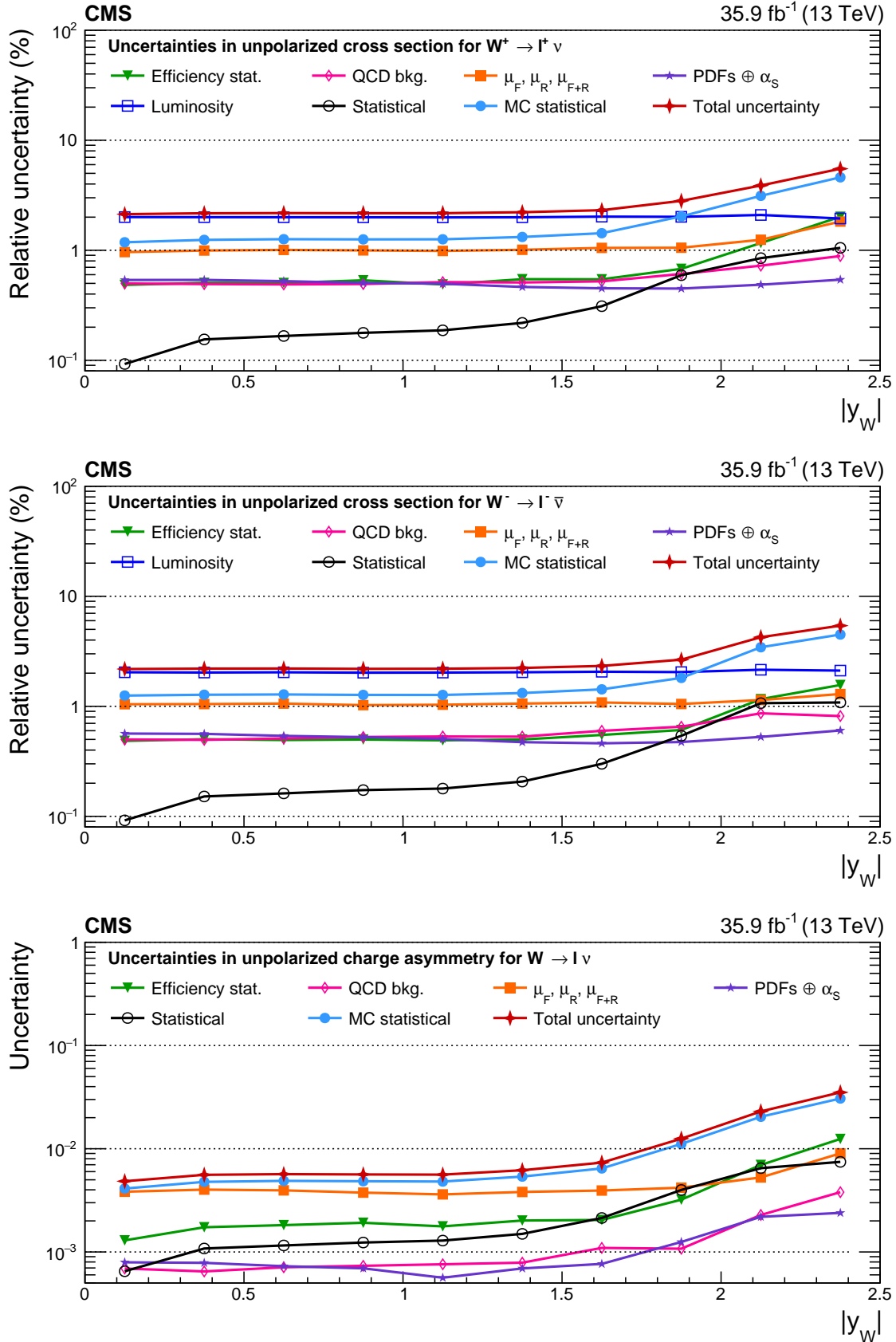


Figure A.14: Impacts on the unpolarized absolute cross sections as functions of the W boson rapidity for W^+ (upper), W^- (middle), and the unpolarized charge asymmetry (lower) bosons in the helicity fit. The groups of uncertainties subleading to the ones shown are suppressed for simplicity.

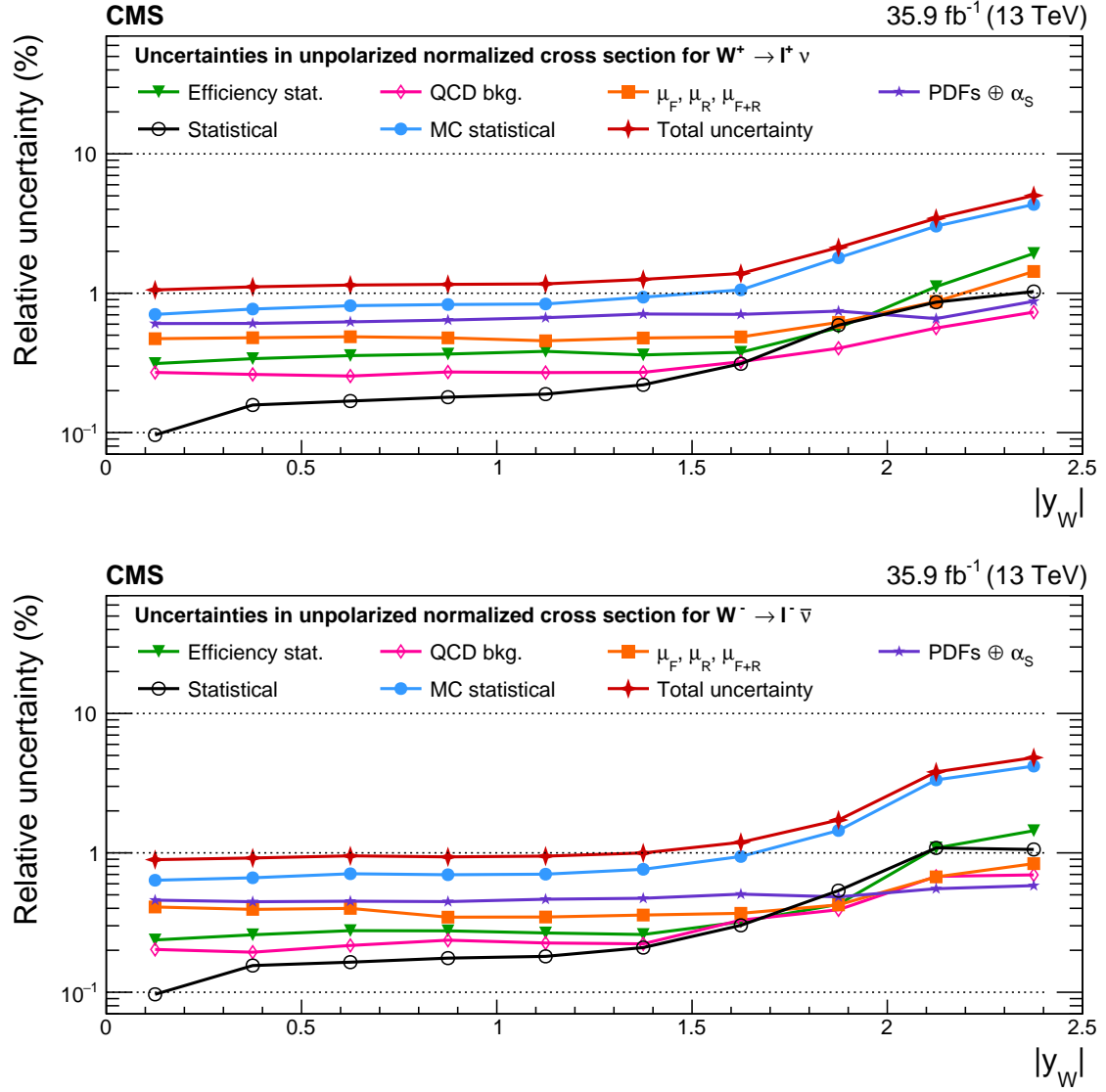


Figure A.15: Impacts on the unpolarized normalized cross sections as functions of the W boson rapidity for W^+ (upper) and W^- (lower) bosons in the helicity fit. The groups of uncertainties subleading to the ones shown are suppressed for simplicity.

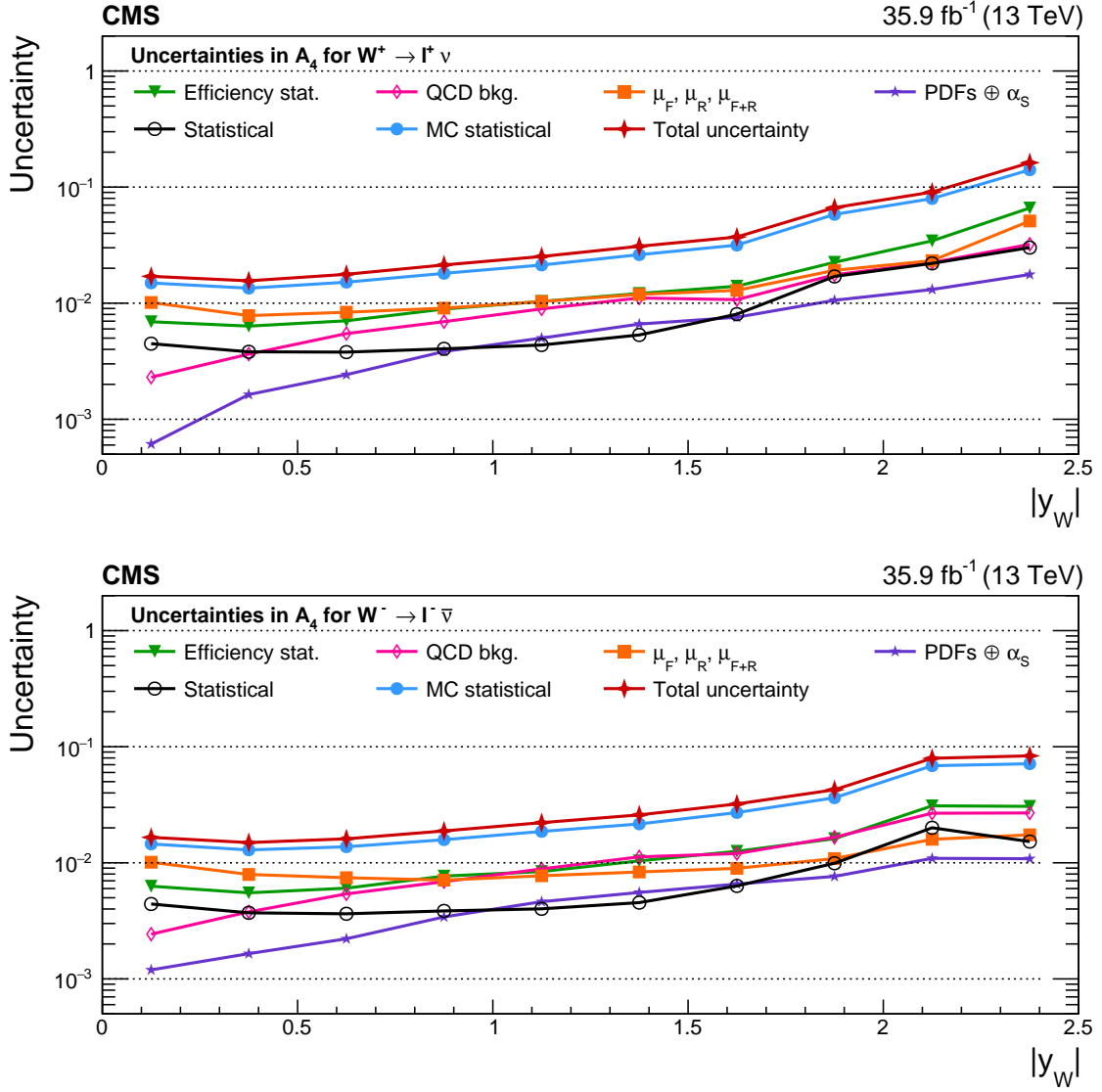


Figure A.16: Impacts on the A_4 coefficient as functions of the W boson rapidity for W^+ (upper) and W^- (lower) bosons in the helicity fit. The groups of uncertainties subleading to the ones shown are suppressed for simplicity.

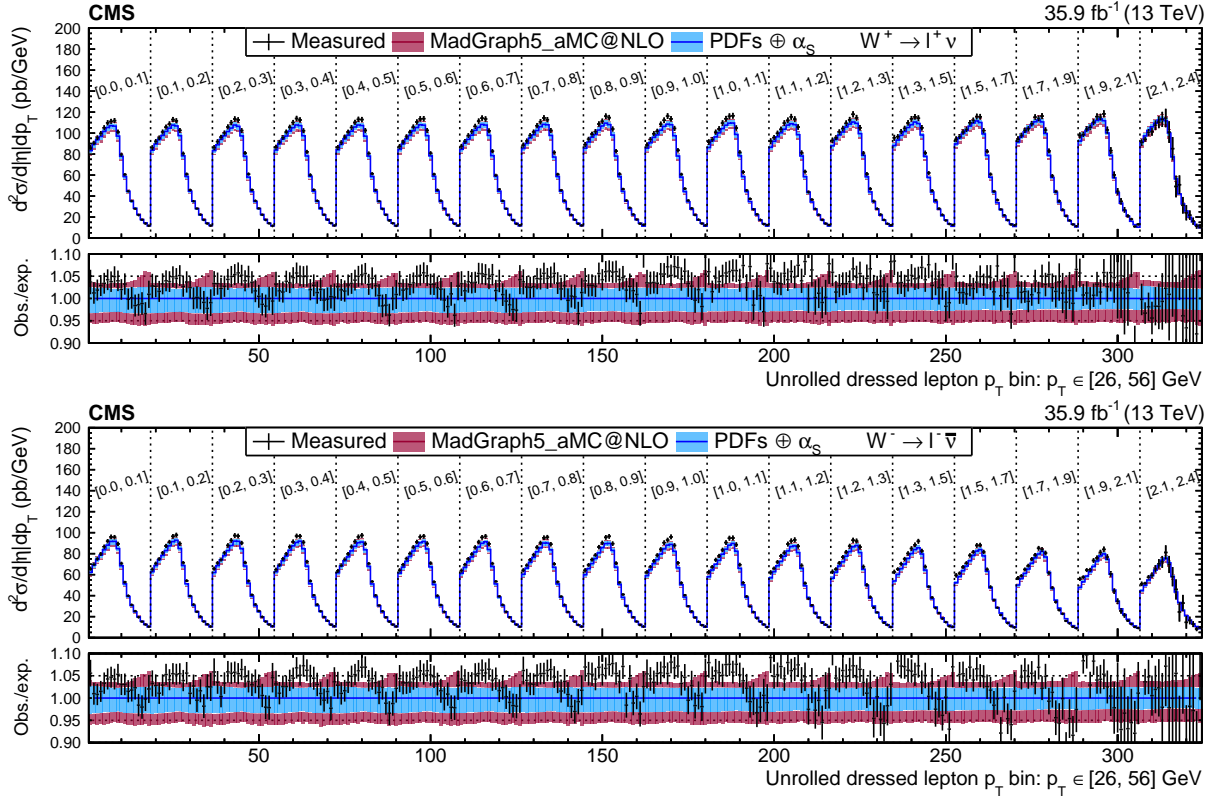


Figure A.17: Unrolled cross sections for the combined muon and electron channel fit unrolled along p_T^ℓ in bins of $|\eta^\ell|$ for W^+ (upper) and W^- (lower) bosons. The colored bands represent the prediction from MADGRAPH5_aMC@NLO with the expected uncertainty from the quadrature sum of the $\text{PDF} \oplus \alpha_s$ variations (blue) and the μ_F and μ_R scales (bordeaux).

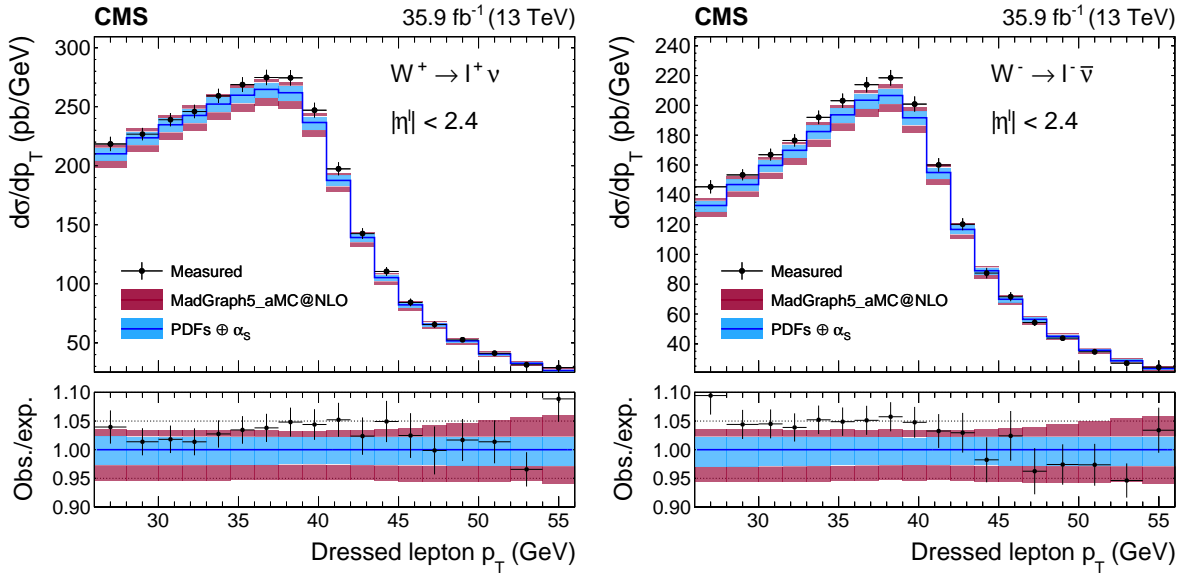


Figure A.18: Absolute cross sections as functions of p_T^ℓ , integrated over $|\eta^\ell|$ for W^+ (left) and W^- (right) bosons. The colored bands represent the prediction from MADGRAPH5_aMC@NLO with the expected uncertainty from the quadrature sum of the $\text{PDF} \oplus \alpha_s$ variations (blue) and the μ_F and μ_R scales (bordeaux).

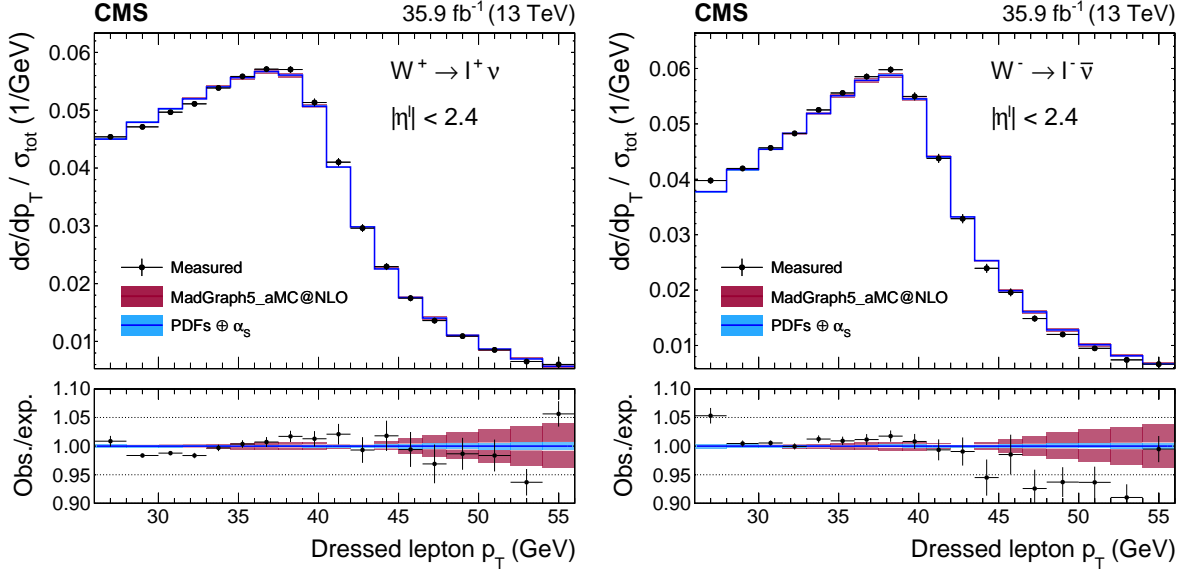


Figure A.19: Normalized cross sections as functions of p_T^ℓ , integrated over $|\eta^\ell|$ for W^+ (left) and W^- (right) bosons. The colored bands represent the prediction from MADGRAPH5_aMC@NLO with the expected uncertainty from the quadrature sum of the $\text{PDF} \oplus \alpha_s$ variations (blue) and the μ_F and μ_R scales (bordeaux).

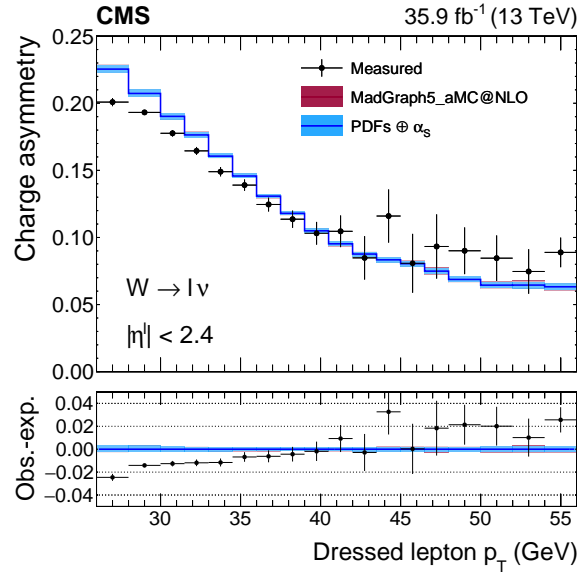


Figure A.20: W charge asymmetry as functions of p_T^ℓ , integrated over $|\eta^\ell|$. The colored bands represent the prediction from MADGRAPH5_aMC@NLO with the expected uncertainty from the quadrature sum of the $\text{PDF} \oplus \alpha_s$ variations (blue) and the μ_F and μ_R scales (bordeaux).

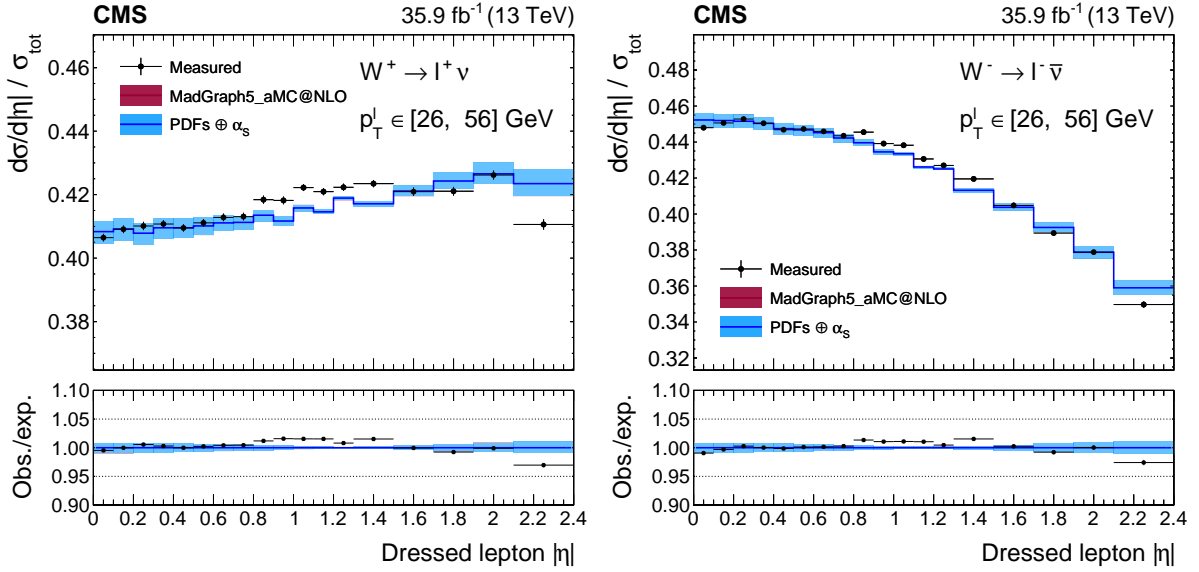


Figure A.21: Normalized cross sections as functions of $|\eta^\ell|$, integrated over p_T^ℓ for W^+ (left) and W^- (right) bosons. The colored bands represent the prediction from MADGRAPH5_aMC@NLO with the expected uncertainty from the quadrature sum of the PDF $\oplus \alpha_s$ variations (blue) and the μ_F and μ_R scales (bordeaux). The uncertainty band is almost entirely dominated by the PDF $\oplus \alpha_s$ variations, while the missing higher order QCD uncertainties almost perfectly cancel and are therefore invisible.

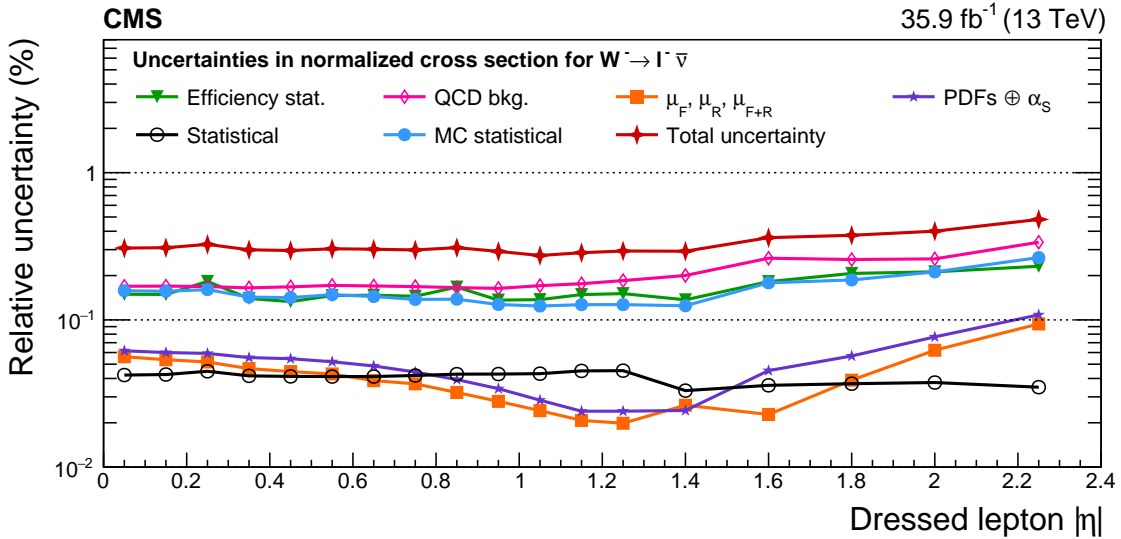


Figure A.22: Remaining impacts of the nuisance groups on the normalized cross sections as functions of $|\eta^\ell|$, integrated in p_T^ℓ , for W^- bosons in the double-differential cross section fit. The groups of uncertainties subleading to the ones shown are suppressed for simplicity.

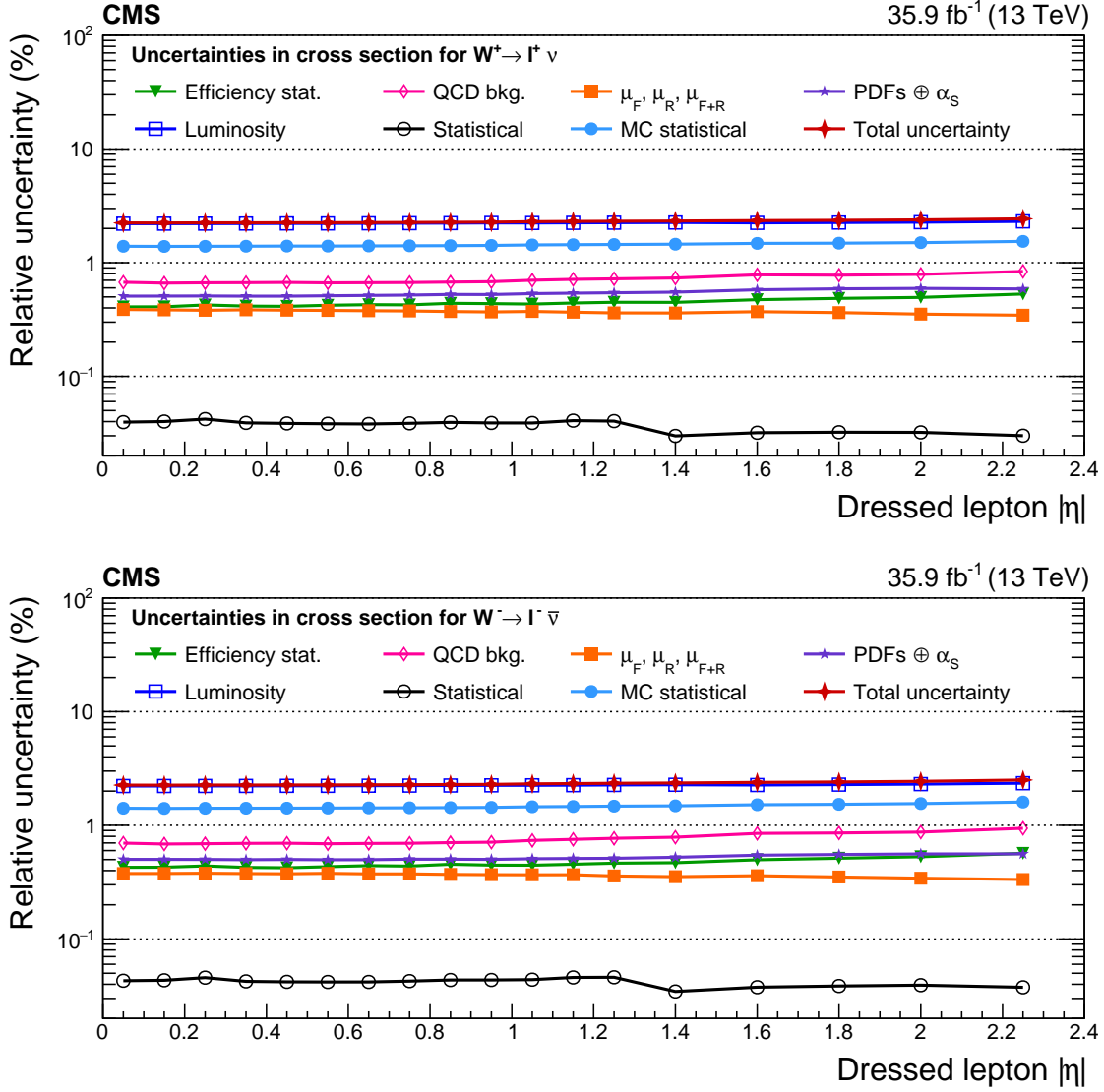


Figure A.23: Remaining impacts of the nuisance groups on the absolute cross sections as functions of $|\eta^\ell|$, integrated in p_T^ℓ , for W^+ (upper) and W^- (lower) bosons in the double-differential cross section fit. The groups of uncertainties subleading to the ones shown are suppressed for simplicity.

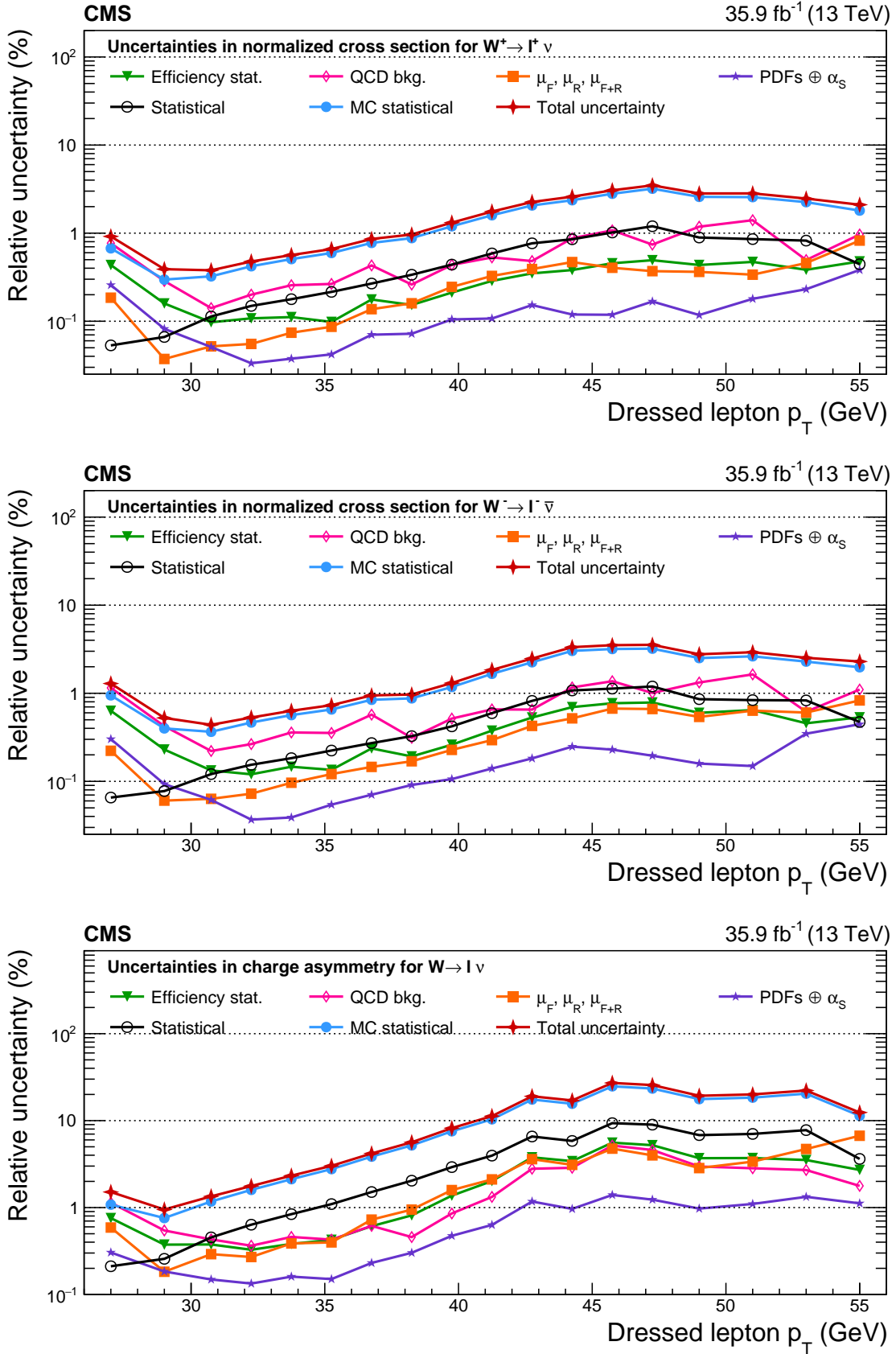


Figure A.24: Remaining impacts of the nuisance groups on the normalized cross sections as functions of p_T^ℓ , integrated over $|\eta^\ell|$, for W^+ (upper), W^- (middle) bosons, and the resulting charge asymmetry (lower) in the double-differential cross section fit. The groups of uncertainties subleading to the ones shown are suppressed for simplicity.

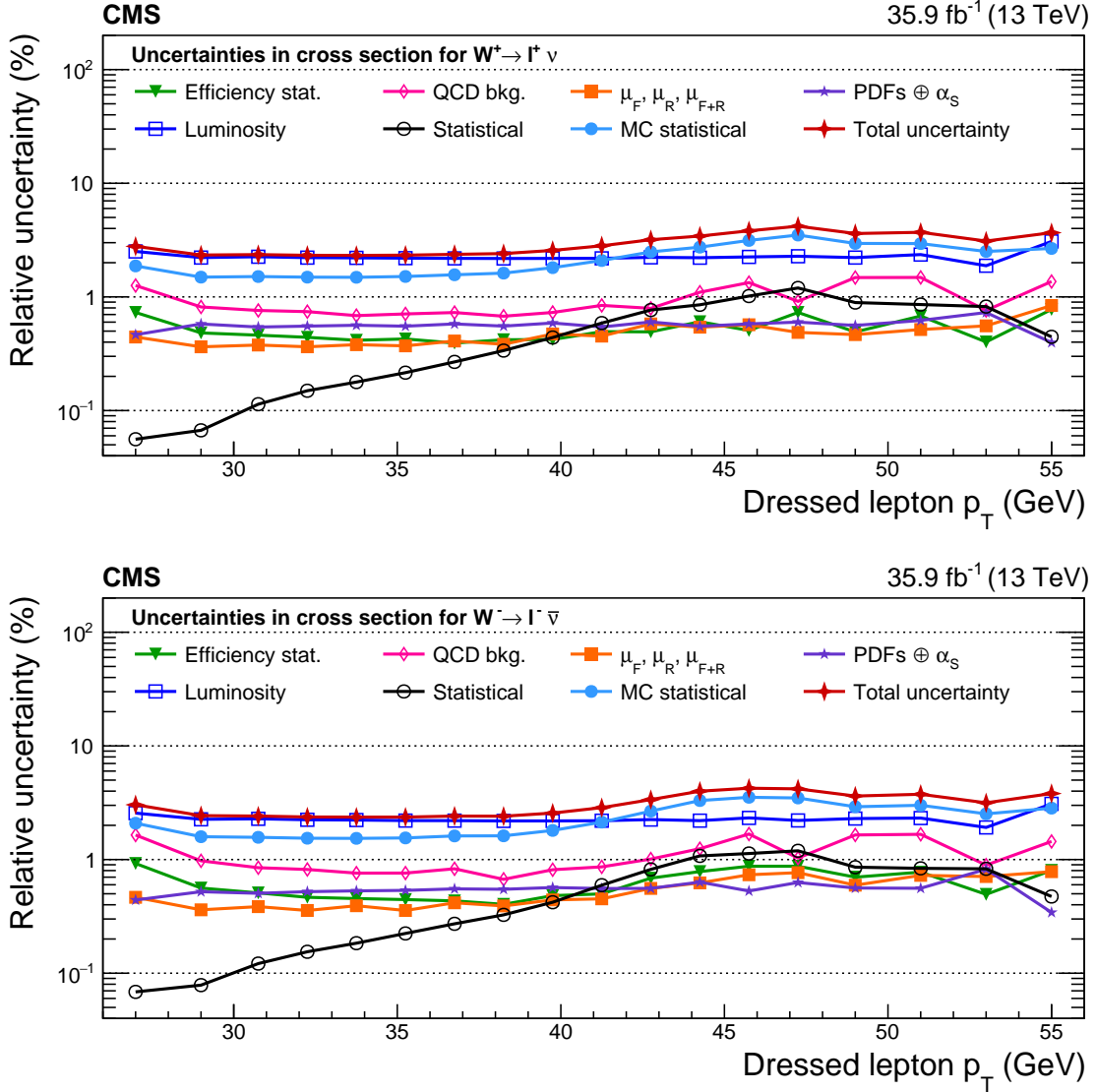


Figure A.25: Remaining impacts of the nuisance groups on the absolute cross sections as functions of p_T^ℓ , integrated over $|\eta^\ell|$, for W^+ (upper) and W^- (lower) bosons in the double-differential cross section fit. The groups of uncertainties subleading to the ones shown are suppressed for simplicity.

B The CMS Collaboration

Yerevan Physics Institute, Yerevan, Armenia

A.M. Sirunyan[†], A. Tumasyan

Institut für Hochenergiephysik, Wien, Austria

W. Adam, F. Ambrogio, T. Bergauer, M. Dragicevic, J. Erö, A. Escalante Del Valle, R. Frühwirth¹, M. Jeitler¹, N. Krammer, L. Lechner, D. Liko, T. Madlener, I. Mikulec, N. Rad, J. Schieck¹, R. Schöfbeck, M. Spanring, S. Templ, W. Waltenberger, C.-E. Wulz¹, M. Zarucki

Institute for Nuclear Problems, Minsk, Belarus

V. Chekhovsky, A. Litomin, V. Makarenko, J. Suarez Gonzalez

Universiteit Antwerpen, Antwerpen, Belgium

M.R. Darwish, E.A. De Wolf, D. Di Croce, X. Janssen, T. Kello², A. Lelek, M. Pieters, H. Rejeb Sfar, H. Van Haevermaet, P. Van Mechelen, S. Van Putte, N. Van Remortel

Vrije Universiteit Brussel, Brussel, Belgium

F. Blekman, E.S. Bols, S.S. Chhibra, J. D'Hondt, J. De Clercq, D. Lontkovskyi, S. Lowette, I. Marchesini, S. Moortgat, Q. Python, S. Tavernier, W. Van Doninck, P. Van Mulders

Université Libre de Bruxelles, Bruxelles, Belgium

D. Beghin, B. Bilin, B. Clerbaux, G. De Lentdecker, H. Delannoy, B. Dorney, L. Favart, A. Grebenyuk, A.K. Kalsi, I. Makarenko, L. Moureaux, L. Pétré, A. Popov, N. Postiau, E. Starling, L. Thomas, C. Vander Velde, P. Vanlaer, D. Vannerom, L. Wezenbeek

Ghent University, Ghent, Belgium

T. Cornelis, D. Dobur, I. Khvastunov³, M. Niedziela, C. Roskas, K. Skovpen, M. Tytgat, W. Verbeke, B. Vermassen, M. Vit

Université Catholique de Louvain, Louvain-la-Neuve, Belgium

G. Bruno, C. Caputo, P. David, C. Delaere, M. Delcourt, I.S. Donertas, A. Giammanco, V. Lemaître, J. Prisciandaro, A. Saggio, A. Taliércio, P. Vischia, S. Wuyckens, J. Zobec

Centro Brasileiro de Pesquisas Físicas, Rio de Janeiro, Brazil

G.A. Alves, G. Correia Silva, C. Hensel, A. Moraes

Universidade do Estado do Rio de Janeiro, Rio de Janeiro, Brazil

W.L. Aldá Júnior, E. Belchior Batista Das Chagas, W. Carvalho, J. Chinellato⁴, E. Coelho, E.M. Da Costa, G.G. Da Silveira⁵, D. De Jesus Damiao, S. Fonseca De Souza, H. Malbouisson, J. Martins⁶, D. Matos Figueiredo, M. Medina Jaime⁷, M. Melo De Almeida, C. Mora Herrera, L. Mundim, H. Nogima, P. Rebello Teles, L.J. Sanchez Rosas, A. Santoro, S.M. Silva Do Amaral, A. Sznajder, M. Thiel, E.J. Tonelli Manganote⁴, F. Torres Da Silva De Araujo, A. Vilela Pereira

Universidade Estadual Paulista ^a, Universidade Federal do ABC ^b, São Paulo, Brazil

C.A. Bernardes^a, L. Calligaris^a, T.R. Fernandez Perez Tomei^a, E.M. Gregores^b, D.S. Lemos^a, P.G. Mercadante^b, S.F. Novaes^a, Sandra S. Padula^a

Institute for Nuclear Research and Nuclear Energy, Bulgarian Academy of Sciences, Sofia, Bulgaria

A. Aleksandrov, G. Antchev, I. Atanasov, R. Hadjiiska, P. Iaydjiev, M. Misheva, M. Rodozov, M. Shopova, G. Sultanov

University of Sofia, Sofia, Bulgaria

M. Bonchev, A. Dimitrov, T. Ivanov, L. Litov, B. Pavlov, P. Petkov, A. Petrov

Beihang University, Beijing, China

W. Fang², X. Gao², L. Yuan

Department of Physics, Tsinghua University, Beijing, China

M. Ahmad, Z. Hu, Y. Wang

Institute of High Energy Physics, Beijing, China

E. Chapon, G.M. Chen⁸, H.S. Chen⁸, M. Chen, C.H. Jiang, D. Leggat, H. Liao, Z. Liu, A. Spiezia, J. Tao, J. Wang, E. Yazgan, H. Zhang, S. Zhang⁸, J. Zhao

State Key Laboratory of Nuclear Physics and Technology, Peking University, Beijing, China

A. Agapitos, Y. Ban, C. Chen, G. Chen, A. Levin, J. Li, L. Li, Q. Li, Y. Mao, S.J. Qian, D. Wang, Q. Wang

Sun Yat-Sen University, Guangzhou, China

Z. You

Zhejiang University, Hangzhou, China

M. Xiao

Universidad de Los Andes, Bogota, Colombia

C. Avila, A. Cabrera, C. Florez, C.F. González Hernández, A. Sarkar, M.A. Segura Delgado

Universidad de Antioquia, Medellin, Colombia

J. Mejia Guisao, J.D. Ruiz Alvarez, C.A. Salazar González, N. Vanegas Arbelaez

University of Split, Faculty of Electrical Engineering, Mechanical Engineering and Naval Architecture, Split, Croatia

D. Giljanović, N. Godinovic, D. Lelas, I. Puljak, T. Sculac

University of Split, Faculty of Science, Split, Croatia

Z. Antunovic, M. Kovac

Institute Rudjer Boskovic, Zagreb, Croatia

V. Brigljevic, D. Ferencek, D. Majumder, B. Mesic, M. Roguljic, A. Starodumov⁹, T. Susa

University of Cyprus, Nicosia, Cyprus

M.W. Ather, A. Attikis, E. Erodotou, A. Ioannou, G. Kole, M. Kolosova, S. Konstantinou, G. Mavromanolakis, J. Mousa, C. Nicolaou, F. Ptochos, P.A. Razis, H. Rykaczewski, H. Saka, D. Tsiakkouri

Charles University, Prague, Czech Republic

M. Finger¹⁰, M. Finger Jr.¹⁰, A. Kveton, J. Tomsa

Escuela Politecnica Nacional, Quito, Ecuador

E. Ayala

Universidad San Francisco de Quito, Quito, Ecuador

E. Carrera Jarrin

Academy of Scientific Research and Technology of the Arab Republic of Egypt, Egyptian Network of High Energy Physics, Cairo, Egypt

S. Abu Zeid¹¹, A. Ellithi Kamel¹², S. Khalil¹³

National Institute of Chemical Physics and Biophysics, Tallinn, Estonia

S. Bhowmik, A. Carvalho Antunes De Oliveira, R.K. Dewanjee, K. Ehataht, M. Kadastik, M. Raidal, C. Veelken

Department of Physics, University of Helsinki, Helsinki, Finland

P. Eerola, L. Forthomme, H. Kirschenmann, K. Osterberg, M. Voutilainen

Helsinki Institute of Physics, Helsinki, Finland

E. Brücken, F. Garcia, J. Havukainen, V. Karimäki, M.S. Kim, R. Kinnunen, T. Lampén, K. Lassila-Perini, S. Laurila, S. Lehti, T. Lindén, H. Siikonen, E. Tuominen, J. Tuominiemi

Lappeenranta University of Technology, Lappeenranta, Finland

P. Luukka, T. Tuuva

IRFU, CEA, Université Paris-Saclay, Gif-sur-Yvette, France

M. Besancon, F. Couderc, M. Dejardin, D. Denegri, J.L. Faure, F. Ferri, S. Ganjour, A. Givernaud, P. Gras, G. Hamel de Monchenault, P. Jarry, C. Leloup, B. Lenzi, E. Locci, J. Malcles, J. Rander, A. Rosowsky, M.Ö. Sahin, A. Savoy-Navarro¹⁴, M. Titov, G.B. Yu

Laboratoire Leprince-Ringuet, CNRS/IN2P3, Ecole Polytechnique, Institut Polytechnique de Paris, Paris, France

S. Ahuja, C. Amendola, F. Beaudette, M. Bonanomi, P. Busson, C. Charlot, B. Diab, G. Falmagne, R. Granier de Cassagnac, I. Kucher, A. Lobanov, C. Martin Perez, M. Nguyen, C. Ochando, P. Paganini, J. Rembser, R. Salerno, J.B. Sauvan, Y. Sirois, A. Zabi, A. Zghiche

Université de Strasbourg, CNRS, IPHC UMR 7178, Strasbourg, France

J.-L. Agram¹⁵, J. Andrea, D. Bloch, G. Bourgatte, J.-M. Brom, E.C. Chabert, C. Collard, J.-C. Fontaine¹⁵, D. Gelé, U. Goerlach, C. Grimault, A.-C. Le Bihan, P. Van Hove

Université de Lyon, Université Claude Bernard Lyon 1, CNRS-IN2P3, Institut de Physique Nucléaire de Lyon, Villeurbanne, France

E. Asilar, S. Beauceron, C. Bernet, G. Boudoul, C. Camen, A. Carle, N. Chanon, R. Chierici, D. Contardo, P. Depasse, H. El Mamouni, J. Fay, S. Gascon, M. Gouzevitch, B. Ille, Sa. Jain, I.B. Laktineh, H. Lattaud, A. Lesauvage, M. Lethuillier, L. Mirabito, L. Torterotot, G. Touquet, M. Vander Donckt, S. Viret

Georgian Technical University, Tbilisi, Georgia

T. Toriashvili¹⁶

Tbilisi State University, Tbilisi, Georgia

Z. Tsamalaidze¹⁰

RWTH Aachen University, I. Physikalisches Institut, Aachen, Germany

L. Feld, K. Klein, M. Lipinski, D. Meuser, A. Pauls, M. Preuten, M.P. Rauch, J. Schulz, M. Teroerde

RWTH Aachen University, III. Physikalisches Institut A, Aachen, Germany

D. Eliseev, M. Erdmann, P. Fackeldey, B. Fischer, S. Ghosh, T. Hebbeker, K. Hoepfner, H. Keller, L. Mastrolorenzo, M. Merschmeyer, A. Meyer, P. Millet, G. Mocellin, S. Mondal, S. Mukherjee, D. Noll, A. Novak, T. Pook, A. Pozdnyakov, T. Quast, M. Radziej, Y. Rath, H. Reithler, J. Roemer, A. Schmidt, S.C. Schuler, A. Sharma, S. Wiedenbeck, S. Zaleski

RWTH Aachen University, III. Physikalisches Institut B, Aachen, Germany

C. Dziwok, G. Flügge, W. Haj Ahmad¹⁷, O. Hlushchenko, T. Kress, A. Nowack, C. Pistone, O. Pooth, D. Roy, H. Sert, A. Stahl¹⁸, T. Ziemons

Deutsches Elektronen-Synchrotron, Hamburg, Germany

H. Aarup Petersen, M. Aldaya Martin, P. Asmuss, I. Babounikau, S. Baxter, K. Beernaert, O. Behnke, A. Bermúdez Martínez, A.A. Bin Anuar, K. Borrás¹⁹, V. Botta, D. Brunner,

A. Campbell, A. Cardini, P. Connor, S. Consuegra Rodríguez, C. Contreras-Campana, V. Danilov, A. De Wit, M.M. Defranchis, L. Didukh, C. Diez Pardos, D. Domínguez Damiani, G. Eckerlin, D. Eckstein, T. Eichhorn, A. Elwood, E. Eren, L.I. Estevez Banos, E. Gallo²⁰, A. Geiser, A. Giraldi, A. Grohsjean, M. Guthoff, M. Haranko, A. Harb, A. Jafari, N.Z. Jomhari, H. Jung, A. Kasem¹⁹, M. Kasemann, H. Kaveh, J. Keaveney, C. Kleinwort, J. Knolle, D. Krücker, W. Lange, T. Lenz, J. Lidrych, K. Lipka, W. Lohmann²¹, R. Mankel, I.-A. Melzer-Pellmann, J. Metwally, A.B. Meyer, M. Meyer, M. Missiroli, J. Mnich, A. Mussgiller, V. Myronenko, Y. Otari, D. Pérez Adán, S.K. Pflitsch, D. Pitzl, A. Raspereza, A. Saibel, M. Savitskyi, V. Scheurer, P. Schütze, C. Schwanenberger, R. Shevchenko, A. Singh, R.E. Sosa Ricardo, H. Tholen, N. Tonon, O. Turkot, A. Vagnerini, M. Van De Klundert, R. Walsh, D. Walter, Y. Wen, K. Wichmann, C. Wissing, S. Wuchterl, O. Zenaiev, R. Zlebcik

University of Hamburg, Hamburg, Germany

R. Aggleton, S. Bein, L. Benato, A. Benecke, K. De Leo, T. Dreyer, A. Ebrahimi, F. Feindt, A. Fröhlich, C. Garbers, E. Garutti, D. Gonzalez, P. Gunnellini, J. Haller, A. Hinzmann, A. Karavdina, G. Kasieczka, R. Klanner, R. Kogler, S. Kurz, V. Kutzner, J. Lange, T. Lange, A. Malara, J. Multhaupt, C.E.N. Niemeyer, A. Nigamova, K.J. Pena Rodriguez, A. Reimers, O. Rieger, P. Schleper, S. Schumann, J. Schwandt, J. Sonneveld, H. Stadie, G. Steinbrück, B. Vormwald, I. Zoi

Karlsruher Institut fuer Technologie, Karlsruhe, Germany

M. Akbiyik, M. Baselga, S. Baur, J. Bechtel, T. Berger, E. Butz, R. Caspart, T. Chwalek, W. De Boer, A. Dierlamm, K. El Morabit, N. Faltermann, K. Flöh, M. Giffels, A. Gottmann, F. Hartmann¹⁸, C. Heidecker, U. Husemann, M.A. Iqbal, I. Katkov²², S. Kudella, S. Maier, M. Metzler, S. Mitra, M.U. Mozer, D. Müller, Th. Müller, M. Musich, G. Quast, K. Rabbertz, J. Rauser, D. Savoie, D. Schäfer, M. Schnepf, M. Schröder, I. Shvetsov, H.J. Simonis, R. Ulrich, M. Wassmer, M. Weber, C. Wöhrmann, R. Wolf, S. Wozniowski

Institute of Nuclear and Particle Physics (INPP), NCSR Demokritos, Aghia Paraskevi, Greece

G. Anagnostou, P. Asenov, G. Daskalakis, T. Geralis, A. Kyriakis, D. Loukas, G. Paspalaki, A. Stakia

National and Kapodistrian University of Athens, Athens, Greece

M. Diamantopoulou, G. Karathanasis, P. Kontaxakis, A. Manousakis-katsikakis, A. Panagiotou, I. Papavergou, N. Saoulidou, K. Theofilatos, K. Vellidis, E. Vourliotis

National Technical University of Athens, Athens, Greece

G. Bakas, K. Kousouris, I. Papakrivopoulos, G. Tsipolitis, A. Zacharopoulou

University of Ioánnina, Ioánnina, Greece

I. Evangelou, C. Foudas, P. Giannaios, P. Katsoulis, P. Kokkas, S. Mallios, K. Manitaras, N. Manthos, I. Papadopoulos, J. Strologas, F.A. Triantis, D. Tsitsonis

MTA-ELTE Lendület CMS Particle and Nuclear Physics Group, Eötvös Loránd University, Budapest, Hungary

M. Bartók²³, R. Chudasama, M. Csanad, M.M.A. Gadallah, P. Major, K. Mandal, A. Mehta, G. Pasztor, O. Surányi, G.I. Veres

Wigner Research Centre for Physics, Budapest, Hungary

G. Bencze, C. Hajdu, D. Horvath²⁴, F. Sikler, V. Veszpremi, G. Vesztergombi[†]

Institute of Nuclear Research ATOMKI, Debrecen, Hungary

N. Beni, S. Czellar, J. Karancsi²³, J. Molnar, Z. Szillasi, D. Teyssier

Institute of Physics, University of Debrecen, Debrecen, Hungary

P. Raics, Z.L. Trocsanyi, B. Ujvari

Eszterhazy Karoly University, Karoly Robert Campus, Gyongyos, Hungary

T. Csorgo, S. Lökös, F. Nemes, T. Novak

Indian Institute of Science (IISc), Bangalore, India

S. Choudhury, J.R. Komaragiri, D. Kumar, L. Panwar, P.C. Tiwari

National Institute of Science Education and Research, HBNI, Bhubaneswar, India

S. Bahinipati²⁶, C. Kar, P. Mal, T. Mishra, V.K. Muraleedharan Nair Bindhu, A. Nayak²⁷, D.K. Sahoo²⁶, N. Sur, S.K. Swain

Panjab University, Chandigarh, India

S. Bansal, S.B. Beri, V. Bhatnagar, S. Chauhan, N. Dhingra²⁸, R. Gupta, A. Kaur, S. Kaur, P. Kumari, M. Lohan, M. Meena, K. Sandeep, S. Sharma, J.B. Singh, A.K. Virdi

University of Delhi, Delhi, India

A. Ahmed, A. Bhardwaj, B.C. Choudhary, R.B. Garg, M. Gola, S. Keshri, A. Kumar, M. Naimuddin, P. Priyanka, K. Ranjan, A. Shah, R. Sharma

Saha Institute of Nuclear Physics, HBNI, Kolkata, India

M. Bharti²⁹, R. Bhattacharya, S. Bhattacharya, D. Bhowmik, S. Dutta, S. Ghosh, B. Gomber³⁰, M. Maity³¹, K. Mondal, S. Nandan, P. Palit, A. Purohit, P.K. Rout, G. Saha, S. Sarkar, M. Sharan, B. Singh²⁹, S. Thakur²⁹

Indian Institute of Technology Madras, Madras, India

P.K. Behera, S.C. Behera, P. Kalbhor, A. Muhammad, R. Pradhan, P.R. Pujahari, A. Sharma, A.K. Sikdar

Bhabha Atomic Research Centre, Mumbai, India

D. Dutta, V. Jha, D.K. Mishra, P.K. Netrakanti, L.M. Pant, P. Shukla

Tata Institute of Fundamental Research-A, Mumbai, India

T. Aziz, M.A. Bhat, S. Dugad, R. Kumar Verma, U. Sarkar

Tata Institute of Fundamental Research-B, Mumbai, India

S. Banerjee, S. Bhattacharya, S. Chatterjee, P. Das, M. Guchait, S. Karmakar, S. Kumar, G. Majumder, K. Mazumdar, S. Mukherjee, N. Sahoo

Indian Institute of Science Education and Research (IISER), Pune, India

S. Dube, B. Kansal, A. Kapoor, K. Kothekar, S. Pandey, A. Rane, A. Rastogi, S. Sharma

Department of Physics, Isfahan University of Technology, Isfahan, Iran

H. Bakhshiansohi³²

Institute for Research in Fundamental Sciences (IPM), Tehran, Iran

S. Chenarani³³, S.M. Etesami, M. Khakzad, M. Mohammadi Najafabadi, M. Naseri

University College Dublin, Dublin, Ireland

M. Felcini, M. Grunewald

INFN Sezione di Bari ^a, Università di Bari ^b, Politecnico di Bari ^c, Bari, Italy

M. Abbrescia^{a,b}, R. Aly^{a,b,34}, C. Calabria^{a,b}, A. Colaleo^a, D. Creanza^{a,c}, L. Cristella^{a,b}, N. De Filippis^{a,c}, M. De Palma^{a,b}, A. Di Florio^{a,b}, A. Di Pilato^{a,b}, W. Elmetenawee^{a,b}, L. Fiore^a, A. Gelmi^{a,b}, G. Iaselli^{a,c}, M. Ince^{a,b}, S. Lezki^{a,b}, G. Maggi^{a,c}, M. Maggi^a, I. Margjeka^{a,b},

J.A. Merlin^a, G. Miniello^{a,b}, S. My^{a,b}, S. Nuzzo^{a,b}, A. Pompili^{a,b}, G. Pugliese^{a,c}, A. Ranieri^a, G. Selvaggi^{a,b}, L. Silvestris^a, F.M. Simone^{a,b}, R. Venditti^a, P. Verwilligen^a

INFN Sezione di Bologna ^a, Università di Bologna ^b, Bologna, Italy

G. Abbiendi^a, C. Battilana^{a,b}, D. Bonacorsi^{a,b}, L. Borghonovi^{a,b}, R. Campanini^{a,b}, P. Capiluppi^{a,b}, A. Castro^{a,b}, F.R. Cavallo^a, C. Ciocca^a, M. Cuffiani^{a,b}, G.M. Dallavalle^a, T. Diotallevi^{a,b}, F. Fabbri^a, A. Fanfani^{a,b}, E. Fontanesi^{a,b}, P. Giacomelli^a, L. Giommi^{a,b}, C. Grandi^a, L. Guiducci^{a,b}, F. Iemmi^{a,b}, S. Lo Meo^{a,35}, S. Marcellini^a, G. Masetti^a, F.L. Navarria^{a,b}, A. Perrotta^a, F. Primavera^{a,b}, T. Rovelli^{a,b}, G.P. Siroli^{a,b}, N. Tosi^a

INFN Sezione di Catania ^a, Università di Catania ^b, Catania, Italy

S. Albergo^{a,b,36}, S. Costa^{a,b}, A. Di Mattia^a, R. Potenza^{a,b}, A. Tricomi^{a,b,36}, C. Tuve^{a,b}

INFN Sezione di Firenze ^a, Università di Firenze ^b, Firenze, Italy

G. Barbagli^a, A. Cassese^a, R. Ceccarelli^{a,b}, V. Ciulli^{a,b}, C. Civinini^a, R. D'Alessandro^{a,b}, F. Fiori^a, E. Focardi^{a,b}, G. Latino^{a,b}, P. Lenzi^{a,b}, M. Lizzo^{a,b}, M. Meschini^a, S. Paoletti^a, R. Seidita^{a,b}, G. Sguazzoni^a, L. Viliani^a

INFN Laboratori Nazionali di Frascati, Frascati, Italy

L. Benussi, S. Bianco, D. Piccolo

INFN Sezione di Genova ^a, Università di Genova ^b, Genova, Italy

M. Bozzo^{a,b}, F. Ferro^a, R. Mulargia^{a,b}, E. Robutti^a, S. Tosi^{a,b}

INFN Sezione di Milano-Bicocca ^a, Università di Milano-Bicocca ^b, Milano, Italy

A. Benaglia^a, A. Beschi^{a,b}, F. Brivio^{a,b}, F. Cetorelli^{a,b}, V. Ciriolo^{a,b,18}, F. De Guio^{a,b}, M.E. Dinardo^{a,b}, P. Dini^a, S. Gennai^a, A. Ghezzi^{a,b}, P. Govoni^{a,b}, L. Guzzi^{a,b}, M. Malberti^a, S. Malvezzi^a, D. Menasce^a, F. Monti^{a,b}, L. Moroni^a, M. Paganoni^{a,b}, D. Pedrini^a, S. Ragazzi^{a,b}, T. Tabarelli de Fatis^{a,b}, D. Valsecchi^{a,b,18}, D. Zuolo^{a,b}

INFN Sezione di Napoli ^a, Università di Napoli 'Federico II' ^b, Napoli, Italy, Università della Basilicata ^c, Potenza, Italy, Università G. Marconi ^d, Roma, Italy

S. Buontempo^a, N. Cavallo^{a,c}, A. De Iorio^{a,b}, F. Fabozzi^{a,c}, F. Fienga^a, G. Galati^a, A.O.M. Iorio^{a,b}, L. Layer^{a,b}, L. Lista^{a,b}, S. Meola^{a,d,18}, P. Paolucci^{a,18}, B. Rossi^a, C. Sciacca^{a,b}, E. Voevodina^{a,b}

INFN Sezione di Padova ^a, Università di Padova ^b, Padova, Italy, Università di Trento ^c, Trento, Italy

P. Azzi^a, N. Bacchetta^a, D. Bisello^{a,b}, A. Boletti^{a,b}, A. Bragagnolo^{a,b}, R. Carlin^{a,b}, P. Checchia^a, P. De Castro Manzano^a, T. Dorigo^a, U. Dosselli^a, F. Gasparini^{a,b}, U. Gasparini^{a,b}, S.Y. Hoh^{a,b}, M. Margoni^{a,b}, A.T. Meneguzzo^{a,b}, M. Presilla^b, P. Ronchese^{a,b}, R. Rossin^{a,b}, F. Simonetto^{a,b}, G. Strong^a, A. Tiko^a, M. Tosi^{a,b}, H. YARAR^{a,b}, M. Zanetti^{a,b}, P. Zotto^{a,b}, A. Zucchetta^{a,b}

INFN Sezione di Pavia ^a, Università di Pavia ^b, Pavia, Italy

A. Braghieri^a, S. Calzaferri^{a,b}, D. Fiorina^{a,b}, P. Montagna^{a,b}, S.P. Ratti^{a,b}, V. Re^a, M. Ressegotti^{a,b}, C. Riccardi^{a,b}, P. Salvini^a, I. Vai^a, P. Vitulo^{a,b}

INFN Sezione di Perugia ^a, Università di Perugia ^b, Perugia, Italy

M. Biasini^{a,b}, G.M. Bilei^a, D. Ciangottini^{a,b}, L. Fanò^{a,b}, P. Lariccia^{a,b}, G. Mantovani^{a,b}, V. Mariani^{a,b}, M. Menichelli^a, A. Rossi^{a,b}, A. Santocchia^{a,b}, D. Spiga^a, T. Tedeschi^{a,b}

INFN Sezione di Pisa ^a, Università di Pisa ^b, Scuola Normale Superiore di Pisa ^c, Pisa, Italy

K. Androsov^a, P. Azzurri^a, G. Bagliesi^a, V. Bertacchi^{a,c}, L. Bianchini^a, T. Boccali^a, R. Castaldi^a, M.A. Ciocci^{a,b}, R. Dell'Orso^a, M.R. Di Domenico^{a,b}, S. Donato^a, L. Giannini^{a,c}, A. Giassi^a, M.T. Grippo^a, F. Ligabue^{a,c}, E. Manca^{a,c}, G. Mandorli^{a,c}, A. Messineo^{a,b}, F. Palla^a, A. Rizzi^{a,b}

G. Rolandi^{a,c}, S. Roy Chowdhury^{a,c}, A. Scribano^a, N. Shafiei^{a,b}, P. Spagnolo^a, R. Tenchini^a, G. Tonelli^{a,b}, N. Turini^a, A. Venturi^a, P.G. Verdini^a

INFN Sezione di Roma ^a, Sapienza Università di Roma ^b, Rome, Italy

F. Cavallari^a, M. Cipriani^{a,b}, D. Del Re^{a,b}, E. Di Marco^a, M. Diemoz^a, E. Longo^{a,b}, P. Meridiani^a, G. Organtini^{a,b}, F. Pandolfi^a, R. Paramatti^{a,b}, C. Quaranta^{a,b}, S. Rahatlou^{a,b}, C. Rovelli^a, F. Santanastasio^{a,b}, L. Soffi^{a,b}, R. Tramontano^{a,b}

INFN Sezione di Torino ^a, Università di Torino ^b, Torino, Italy, Università del Piemonte Orientale ^c, Novara, Italy

N. Amapane^{a,b}, R. Arcidiacono^{a,c}, S. Argiro^{a,b}, M. Arneodo^{a,c}, N. Bartosik^a, R. Bellan^{a,b}, A. Bellora^{a,b}, C. Biino^a, A. Cappati^{a,b}, N. Cartiglia^a, S. Cometti^a, M. Costa^{a,b}, R. Covarelli^{a,b}, N. Demaria^a, B. Kiani^{a,b}, F. Legger^a, C. Mariotti^a, S. Maselli^a, E. Migliore^{a,b}, V. Monaco^{a,b}, E. Monteil^{a,b}, M. Monteno^a, M.M. Obertino^{a,b}, G. Ortona^a, L. Pacher^{a,b}, N. Pastrone^a, M. Pelliccioni^a, G.L. Pinna Angioni^{a,b}, M. Ruspa^{a,c}, R. Salvatico^{a,b}, F. Siviero^{a,b}, V. Sola^a, A. Solano^{a,b}, D. Soldi^{a,b}, A. Staiano^a, D. Trocino^{a,b}

INFN Sezione di Trieste ^a, Università di Trieste ^b, Trieste, Italy

S. Belforte^a, V. Candelise^{a,b}, M. Casarsa^a, F. Cossutti^a, A. Da Rold^{a,b}, G. Della Ricca^{a,b}, F. Vazzoler^{a,b}

Kyungpook National University, Daegu, Korea

S. Dogra, C. Huh, B. Kim, D.H. Kim, G.N. Kim, J. Lee, S.W. Lee, C.S. Moon, Y.D. Oh, S.I. Pak, S. Sekmen, D.C. Son, Y.C. Yang

Chonnam National University, Institute for Universe and Elementary Particles, Kwangju, Korea

H. Kim, D.H. Moon

Hanyang University, Seoul, Korea

B. Francois, T.J. Kim, J. Park

Korea University, Seoul, Korea

S. Cho, S. Choi, Y. Go, S. Ha, B. Hong, K. Lee, K.S. Lee, J. Lim, J. Park, S.K. Park, Y. Roh, J. Yoo

Kyung Hee University, Department of Physics, Seoul, Republic of Korea

J. Goh, A. Gurtu

Sejong University, Seoul, Korea

H.S. Kim, Y. Kim

Seoul National University, Seoul, Korea

J. Almond, J.H. Bhyun, J. Choi, S. Jeon, J. Kim, J.S. Kim, S. Ko, H. Kwon, H. Lee, K. Lee, S. Lee, K. Nam, B.H. Oh, M. Oh, S.B. Oh, B.C. Radburn-Smith, H. Seo, U.K. Yang, I. Yoon

University of Seoul, Seoul, Korea

D. Jeon, J.H. Kim, B. Ko, J.S.H. Lee, I.C. Park, I.J. Watson

Yonsei University, Department of Physics, Seoul, Korea

H.D. Yoo

Sungkyunkwan University, Suwon, Korea

Y. Choi, C. Hwang, Y. Jeong, J. Lee, Y. Lee, I. Yu

Riga Technical University, Riga, Latvia

T. Torims, V. Veckalns³⁷

Vilnius University, Vilnius, Lithuania

A. Juodagalvis, A. Rinkevicius, G. Tamulaitis

National Centre for Particle Physics, Universiti Malaya, Kuala Lumpur, Malaysia

W.A.T. Wan Abdullah, M.N. Yusli, Z. Zolkapli

Universidad de Sonora (UNISON), Hermosillo, Mexico

J.F. Benitez, A. Castaneda Hernandez, J.A. Murillo Quijada, L. Valencia Palomo

Centro de Investigacion y de Estudios Avanzados del IPN, Mexico City, Mexico

H. Castilla-Valdez, E. De La Cruz-Burelo, I. Heredia-De La Cruz³⁸, R. Lopez-Fernandez, A. Sanchez-Hernandez

Universidad Iberoamericana, Mexico City, Mexico

S. Carrillo Moreno, C. Oropeza Barrera, M. Ramirez-Garcia, F. Vazquez Valencia

Benemerita Universidad Autonoma de Puebla, Puebla, Mexico

J. Eysermans, I. Pedraza, H.A. Salazar Ibarguen, C. Uribe Estrada

Universidad Autónoma de San Luis Potosí, San Luis Potosí, Mexico

A. Morelos Pineda

University of Montenegro, Podgorica, Montenegro

J. Mijuskovic³, N. Raicevic

University of Auckland, Auckland, New Zealand

D. Krofcheck

University of Canterbury, Christchurch, New Zealand

S. Bheesette, P.H. Butler

National Centre for Physics, Quaid-I-Azam University, Islamabad, Pakistan

A. Ahmad, M. Ahmad, M.I. Asghar, M.I.M. Awan, Q. Hassan, H.R. Hoorani, W.A. Khan, S. Qazi, M.A. Shah, M. Waqas

AGH University of Science and Technology Faculty of Computer Science, Electronics and Telecommunications, Krakow, Poland

V. Avati, L. Grzanka, M. Malawski

National Centre for Nuclear Research, Swierk, Poland

H. Bialkowska, M. Bluj, B. Boimska, T. Frueboes, M. Górski, M. Kazana, M. Szleper, P. Traczyk, P. Zalewski

Institute of Experimental Physics, Faculty of Physics, University of Warsaw, Warsaw, Poland

K. Bunkowski, A. Byszek³⁹, K. Doroba, A. Kalinowski, M. Konecki, J. Krolikowski, M. Olszewski, M. Walczak

Laboratório de Instrumentação e Física Experimental de Partículas, Lisboa, Portugal

M. Araujo, P. Bargassa, D. Bastos, A. Di Francesco, P. Faccioli, B. Galinhas, M. Gallinaro, J. Hollar, N. Leonardo, T. Niknejad, J. Seixas, K. Shchelina, O. Toldaiev, J. Varela

Joint Institute for Nuclear Research, Dubna, Russia

S. Afanasiev, V. Alexakhin, P. Bunin, M. Gavrilenko, A. Golunov, I. Golutvin, N. Gorbounov, I. Gorbunov, V. Karjavine, A. Lanev, A. Malakhov, V. Matveev^{40,41}, P. Moisezenz, V. Palichik, V. Perelygin, M. Savina, S. Shmatov, O. Teryaev, B.S. Yuldashev⁴², A. Zarubin

Petersburg Nuclear Physics Institute, Gatchina (St. Petersburg), Russia

G. Gavrillov, V. Golovtcov, Y. Ivanov, V. Kim⁴³, E. Kuznetsova⁴⁴, V. Murzin, V. Oreshkin, I. Smirnov, D. Sosnov, V. Sulimov, L. Uvarov, S. Volkov, A. Vorobyev

Institute for Nuclear Research, Moscow, Russia

Yu. Andreev, A. Dermenev, S. Gninenko, N. Golubev, A. Karneyeu, M. Kirsanov, N. Krasnikov, A. Pashenkov, G. Pivovarov, D. Tlisov, A. Toropin

Institute for Theoretical and Experimental Physics named by A.I. Alikhanov of NRC 'Kurchatov Institute', Moscow, Russia

V. Epshteyn, V. Gavrillov, N. Lychkovskaya, A. Nikitenko⁴⁵, V. Popov, I. Pozdnyakov, G. Safronov, A. Spiridonov, A. Stepenov, M. Toms, E. Vlasov, A. Zhokin

Moscow Institute of Physics and Technology, Moscow, Russia

T. Aushev

National Research Nuclear University 'Moscow Engineering Physics Institute' (MEPhI), Moscow, Russia

O. Bychkova, M. Chadeeva⁴⁶, A. Oskin, P. Parygin, E. Popova, V. Rusinov

P.N. Lebedev Physical Institute, Moscow, Russia

V. Andreev, M. Azarkin, I. Dremin, M. Kirakosyan, A. Terkulov

Skobeltsyn Institute of Nuclear Physics, Lomonosov Moscow State University, Moscow, Russia

A. Belyaev, E. Boos, V. Bunichev, M. Dubinin⁴⁷, L. Dudko, V. Klyukhin, O. Kodolova, I. Lokhtin, S. Obraztsov, M. Perfilov, S. Petrushanko, V. Savrin, A. Snigirev

Novosibirsk State University (NSU), Novosibirsk, Russia

V. Blinov⁴⁸, T. Dimova⁴⁸, L. Kardapoltsev⁴⁸, I. Ovtin⁴⁸, Y. Skovpen⁴⁸

Institute for High Energy Physics of National Research Centre 'Kurchatov Institute', Protvino, Russia

I. Azhgirey, I. Bayshev, S. Bitioukov, V. Kachanov, A. Kalinin, D. Konstantinov, V. Petrov, R. Ryutin, A. Sobol, S. Troshin, N. Tyurin, A. Uzunian, A. Volkov

National Research Tomsk Polytechnic University, Tomsk, Russia

A. Babaev, A. Iuzhakov, V. Okhotnikov

Tomsk State University, Tomsk, Russia

V. Borchsh, V. Ivanchenko, E. Tcherniaev

University of Belgrade: Faculty of Physics and VINCA Institute of Nuclear Sciences, Belgrade, Serbia

P. Adzic⁴⁹, P. Cirkovic, M. Dordevic, P. Milenovic, J. Milosevic, M. Stojanovic

Centro de Investigaciones Energéticas Medioambientales y Tecnológicas (CIEMAT), Madrid, Spain

M. Aguilar-Benitez, J. Alcaraz Maestre, A. Álvarez Fernández, I. Bachiller, M. Barrio Luna, Cristina F. Bedoya, J.A. Brochero Cifuentes, C.A. Carrillo Montoya, M. Cepeda, M. Cerrada, N. Colino, B. De La Cruz, A. Delgado Peris, J.P. Fernández Ramos, J. Flix, M.C. Fouz, O. Gonzalez Lopez, S. Goy Lopez, J.M. Hernandez, M.I. Josa, D. Moran, Á. Navarro Tobar, A. Pérez-Calero Yzquierdo, J. Puerta Pelayo, I. Redondo, L. Romero, S. Sánchez Navas, M.S. Soares, A. Triossi, C. Willmott

Universidad Autónoma de Madrid, Madrid, Spain

C. Albajar, J.F. de Trocóniz, R. Reyes-Almanza

Universidad de Oviedo, Instituto Universitario de Ciencias y Tecnologías Espaciales de Asturias (ICTEA), Oviedo, Spain

B. Alvarez Gonzalez, J. Cuevas, C. Erice, J. Fernandez Menendez, S. Folgueras, I. Gonzalez Caballero, E. Palencia Cortezon, C. Ramón Álvarez, V. Rodríguez Bouza, S. Sanchez Cruz

Instituto de Física de Cantabria (IFCA), CSIC-Universidad de Cantabria, Santander, Spain

I.J. Cabrillo, A. Calderon, B. Chazin Quero, J. Duarte Campderros, M. Fernandez, P.J. Fernández Manteca, A. García Alonso, G. Gomez, C. Martinez Rivero, P. Martinez Ruiz del Arbol, F. Matorras, J. Piedra Gomez, C. Prieels, F. Ricci-Tam, T. Rodrigo, A. Ruiz-Jimeno, L. Russo⁵⁰, L. Scodellaro, I. Vila, J.M. Vizan Garcia

University of Colombo, Colombo, Sri Lanka

MK Jayananda, B. Kailasapathy, D.U.J. Sonnadara, DDC Wickramarathna

University of Ruhuna, Department of Physics, Matara, Sri Lanka

W.G.D. Dharmaratna, K. Liyanage, N. Perera, N. Wickramage

CERN, European Organization for Nuclear Research, Geneva, Switzerland

T.K. Aarrestad, D. Abbaneo, B. Akgun, E. Auffray, G. Auzinger, J. Baechler, P. Baillon, A.H. Ball, D. Barney, J. Bendavid, M. Bianco, A. Bocci, P. Bortignon, E. Bossini, E. Brondolin, T. Camporesi, G. Cerminara, D. d'Enterria, A. Dabrowski, N. Daci, V. Daponte, A. David, O. Davignon, A. De Roeck, M. Deile, R. Di Maria, M. Dobson, M. Dünser, N. Dupont, A. Elliott-Peisert, N. Emriskova, F. Fallavollita⁵¹, D. Fasanella, S. Fiorendi, G. Franzoni, J. Fulcher, W. Funk, S. Giani, D. Gigi, K. Gill, F. Glege, L. Gouskos, M. Gruchala, M. Guilbaud, D. Gulhan, J. Hegeman, C. Heidegger, Y. Iiyama, V. Innocente, T. James, P. Janot, J. Kaspar, J. Kieseler, N. Kratochwil, C. Lange, P. Lecoq, K. Long, C. Lourenço, L. Malgeri, M. Mannelli, A. Massironi, F. Meijers, S. Mersi, E. Meschi, F. Moortgat, M. Mulders, J. Ngadiuba, J. Niedziela, S. Orfanelli, L. Orsini, F. Pantaleo¹⁸, L. Pape, E. Perez, M. Peruzzi, A. Petrilli, G. Petrucciani, A. Pfeiffer, M. Pierini, F.M. Pitters, D. Rabady, A. Racz, M. Rieger, M. Rovere, H. Sakulin, J. Salfeld-Nebgen, S. Scarfi, C. Schäfer, C. Schwick, M. Selvaggi, A. Sharma, P. Silva, W. Snoeys, P. Sphicas⁵², J. Steggemann, S. Summers, V.R. Tavolaro, D. Treille, A. Tsiros, G.P. Van Onsem, A. Vartak, M. Verzetti, K.A. Wozniak, W.D. Zeuner

Paul Scherrer Institut, Villigen, Switzerland

L. Caminada⁵³, K. Deiters, W. Erdmann, R. Horisberger, Q. Ingram, H.C. Kaestli, D. Kotlinski, U. Langenegger, T. Rohe

ETH Zurich - Institute for Particle Physics and Astrophysics (IPA), Zurich, Switzerland

M. Backhaus, P. Berger, A. Calandri, N. Chernyavskaya, G. Dissertori, M. Dittmar, M. Donegà, C. Dorfer, T. Gadek, T.A. Gómez Espinosa, C. Grab, D. Hits, W. Lustermann, A.-M. Lyon, R.A. Manzoni, M.T. Meinhard, F. Micheli, P. Musella, F. Nessi-Tedaldi, F. Pauss, V. Perovic, G. Perrin, L. Perrozzi, S. Pigazzini, M.G. Ratti, M. Reichmann, C. Reissel, T. Reitspiess, B. Ristic, D. Ruini, D.A. Sanz Becerra, M. Schönenberger, L. Shchutska, V. Stampf, M.L. Vesterbacka Olsson, R. Wallny, D.H. Zhu

Universität Zürich, Zurich, Switzerland

C. Amsler⁵⁴, C. Botta, D. Brzhechko, M.F. Canelli, A. De Cosa, R. Del Burgo, J.K. Heikkilä, M. Huwiler, B. Kilminster, S. Leontsinis, A. Macchiolo, V.M. Mikuni, I. Neutelings, G. Rauco, P. Robmann, K. Schweiger, Y. Takahashi, S. Wertz

National Central University, Chung-Li, Taiwan

C.M. Kuo, W. Lin, A. Roy, T. Sarkar³¹, S.S. Yu

National Taiwan University (NTU), Taipei, Taiwan

L. Ceard, P. Chang, Y. Chao, K.F. Chen, P.H. Chen, W.-S. Hou, Y.y. Li, R.-S. Lu, E. Paganis, A. Psallidas, A. Steen

Chulalongkorn University, Faculty of Science, Department of Physics, Bangkok, Thailand

B. Asavapibhop, C. Asawatangtrakuldee, N. Srimanobhas

Çukurova University, Physics Department, Science and Art Faculty, Adana, Turkey

A. Bat, F. Boran, S. Damarseckin⁵⁵, Z.S. Demiroglu, F. Dolek, C. Dozen⁵⁶, I. Dumanoglu⁵⁷, E. Eskut, G. Gokbulut, Y. Guler, E. Gurpinar Guler⁵⁸, I. Hos⁵⁹, C. Isik, E.E. Kangal⁶⁰, O. Kara, A. Kayis Topaksu, U. Kiminsu, G. Onengut, K. Ozdemir⁶¹, A. Polatoz, A.E. Simsek, B. Tali⁶², U.G. Tok, S. Turkcapar, I.S. Zorbakir, C. Zorbilmez

Middle East Technical University, Physics Department, Ankara, Turkey

B. Isildak⁶³, G. Karapinar⁶⁴, K. Ocalan⁶⁵, M. Yalvac⁶⁶

Bogazici University, Istanbul, Turkey

I.O. Atakisi, E. Gülmez, M. Kaya⁶⁷, O. Kaya⁶⁸, Ö. Özçelik, S. Tekten⁶⁹, E.A. Yetkin⁷⁰

Istanbul Technical University, Istanbul, Turkey

A. Cakir, K. Cankocak⁵⁷, Y. Komurcu, S. Sen⁷¹

Istanbul University, Istanbul, Turkey

F. Aydogmus Sen, S. Cerci⁶², B. Kaynak, S. Ozkorucuklu, D. Sunar Cerci⁶²

Institute for Scintillation Materials of National Academy of Science of Ukraine, Kharkov, Ukraine

B. Grynyov

National Scientific Center, Kharkov Institute of Physics and Technology, Kharkov, Ukraine

L. Levchuk

University of Bristol, Bristol, United Kingdom

E. Bhal, S. Bologna, J.J. Brooke, D. Burns⁷², E. Clement, D. Cussans, H. Flacher, J. Goldstein, G.P. Heath, H.F. Heath, L. Kreczko, B. Krikler, S. Paramesvaran, T. Sakuma, S. Seif El Nasr-Storey, V.J. Smith, J. Taylor, A. Titterton

Rutherford Appleton Laboratory, Didcot, United Kingdom

K.W. Bell, A. Belyaev⁷³, C. Brew, R.M. Brown, D.J.A. Cockerill, K.V. Ellis, K. Harder, S. Harper, J. Linacre, K. Manolopoulos, D.M. Newbold, E. Olaiya, D. Petyt, T. Reis, T. Schuh, C.H. Shepherd-Themistocleous, A. Thea, I.R. Tomalin, T. Williams

Imperial College, London, United Kingdom

R. Bainbridge, P. Bloch, S. Bonomally, J. Borg, S. Breeze, O. Buchmuller, A. Bundock, V. Cepaitis, G.S. Chahal⁷⁴, D. Colling, P. Dauncey, G. Davies, M. Della Negra, P. Everaerts, G. Hall, G. Iles, J. Langford, L. Lyons, A.-M. Magnan, S. Malik, A. Martelli, V. Milosevic, A. Morton, J. Nash⁷⁵, V. Palladino, M. Pesaresi, D.M. Raymond, A. Richards, A. Rose, E. Scott, C. Seez, A. Shtipliyski, M. Stoye, A. Tapper, K. Uchida, T. Virdee¹⁸, N. Wardle, S.N. Webb, D. Winterbottom, A.G. Zecchinelli, S.C. Zenz

Brunel University, Uxbridge, United Kingdom

J.E. Cole, P.R. Hobson, A. Khan, P. Kyberd, C.K. Mackay, I.D. Reid, L. Teodorescu, S. Zahid

Baylor University, Waco, USA

A. Brinkerhoff, K. Call, B. Caraway, J. Dittmann, K. Hatakeyama, C. Madrid, B. McMaster, N. Pastika, C. Smith

Catholic University of America, Washington, DC, USA

R. Bartek, A. Dominguez, R. Uniyal, A.M. Vargas Hernandez

The University of Alabama, Tuscaloosa, USA

A. Buccilli, O. Charaf, S.I. Cooper, S.V. Gleyzer, C. Henderson, P. Rumerio, C. West

Boston University, Boston, USA

A. Albert, D. Arcaro, Z. Demiragli, D. Gastler, C. Richardson, J. Rohlf, D. Sperka, D. Spitzbart, I. Suarez, D. Zou

Brown University, Providence, USA

G. Benelli, B. Burkle, X. Coubez¹⁹, D. Cutts, Y.t. Duh, M. Hadley, U. Heintz, J.M. Hogan⁷⁶, K.H.M. Kwok, E. Laird, G. Landsberg, K.T. Lau, J. Lee, M. Narain, S. Sagir⁷⁷, R. Syarif, E. Usai, W.Y. Wong, D. Yu, W. Zhang

University of California, Davis, Davis, USA

R. Band, C. Brainerd, R. Breedon, M. Calderon De La Barca Sanchez, M. Chertok, J. Conway, R. Conway, P.T. Cox, R. Erbacher, C. Flores, G. Funk, F. Jensen, W. Ko[†], O. Kukral, R. Lander, M. Mulhearn, D. Pellett, J. Pilot, M. Shi, D. Taylor, K. Tos, M. Tripathi, Z. Wang, Y. Yao, F. Zhang

University of California, Los Angeles, USA

M. Bachtis, C. Bravo, R. Cousins, A. Dasgupta, A. Florent, D. Hamilton, J. Hauser, M. Ignatenko, T. Lam, N. Mccoll, W.A. Nash, S. Regnard, D. Saltzberg, C. Schnaible, B. Stone, V. Valuev

University of California, Riverside, Riverside, USA

K. Burt, Y. Chen, R. Clare, J.W. Gary, S.M.A. Ghiasi Shirazi, G. Hanson, G. Karapostoli, O.R. Long, N. Manganeli, M. Olmedo Negrete, M.I. Paneva, W. Si, S. Wimpenny, Y. Zhang

University of California, San Diego, La Jolla, USA

J.G. Branson, P. Chang, S. Cittolin, S. Cooperstein, N. Deelen, M. Derdzinski, J. Duarte, R. Gerosa, D. Gilbert, B. Hashemi, D. Klein, V. Krutelyov, J. Letts, M. Masciovecchio, S. May, S. Padhi, M. Pieri, V. Sharma, M. Tadel, F. Würthwein, A. Yagil

University of California, Santa Barbara - Department of Physics, Santa Barbara, USA

N. Amin, R. Bhandari, C. Campagnari, M. Citron, A. Dorsett, V. Dutta, J. Incandela, B. Marsh, H. Mei, A. Ovcharova, H. Qu, J. Richman, U. Sarica, D. Stuart, S. Wang

California Institute of Technology, Pasadena, USA

D. Anderson, A. Bornheim, O. Cerri, I. Dutta, J.M. Lawhorn, N. Lu, J. Mao, H.B. Newman, T.Q. Nguyen, J. Pata, M. Spiropulu, J.R. Vlimant, S. Xie, Z. Zhang, R.Y. Zhu

Carnegie Mellon University, Pittsburgh, USA

J. Alison, M.B. Andrews, T. Ferguson, T. Mudholkar, M. Paulini, M. Sun, I. Vorobiev, M. Weinberg

University of Colorado Boulder, Boulder, USA

J.P. Cumalat, W.T. Ford, E. MacDonald, T. Mulholland, R. Patel, A. Perloff, K. Stenson, K.A. Ulmer, S.R. Wagner

Cornell University, Ithaca, USA

J. Alexander, Y. Cheng, J. Chu, A. Datta, A. Frankenthal, K. Mcdermott, J. Monroy, J.R. Patterson, D. Quach, A. Ryd, W. Sun, S.M. Tan, Z. Tao, J. Thom, P. Wittich, M. Zientek

Fermi National Accelerator Laboratory, Batavia, USA

S. Abdullin, M. Albrow, M. Alyari, G. Apollinari, A. Apresyan, A. Apyan, S. Banerjee, L.A.T. Bauerick, A. Beretvas, D. Berry, J. Berryhill, P.C. Bhat, K. Burkett, J.N. Butler, A. Canepa, G.B. Cerati, H.W.K. Cheung, F. Chlebana, M. Cremonesi, V.D. Elvira, J. Freeman, Z. Gecse, E. Gottschalk, L. Gray, D. Green, S. Grünendahl, O. Gutsche, R.M. Harris, S. Hasegawa, R. Heller, T.C. Herwig, J. Hirschauer, B. Jayatilaka, S. Jindariani, M. Johnson, U. Joshi, T. Klijnsma, B. Klima, M.J. Kortelainen, S. Lammel, J. Lewis, D. Lincoln, R. Lipton, M. Liu, T. Liu, J. Lykken, K. Maeshima, J.M. Marraffino, D. Mason, P. McBride, P. Merkel, S. Mrenna, S. Nahn, V. O'Dell, V. Papadimitriou, K. Pedro, C. Pena⁴⁷, O. Prokofyev, F. Ravera, A. Reinsvold Hall, L. Ristori, B. Schneider, E. Sexton-Kennedy, N. Smith, A. Soha, W.J. Spalding, L. Spiegel, S. Stoynev, J. Strait, L. Taylor, S. Tkaczyk, N.V. Tran, L. Uplegger, E.W. Vaandering, M. Wang, H.A. Weber, A. Woodard

University of Florida, Gainesville, USA

D. Acosta, P. Avery, D. Bourilkov, L. Cadamuro, V. Cherepanov, F. Errico, R.D. Field, D. Guerrero, B.M. Joshi, M. Kim, J. Konigsberg, A. Korytov, K.H. Lo, K. Matchev, N. Menendez, G. Mitselmakher, D. Rosenzweig, K. Shi, J. Wang, S. Wang, X. Zuo

Florida International University, Miami, USA

Y.R. Joshi

Florida State University, Tallahassee, USA

T. Adams, A. Askew, D. Diaz, R. Habibullah, S. Hagopian, V. Hagopian, K.F. Johnson, R. Khurana, T. Kolberg, G. Martinez, H. Prosper, C. Schiber, R. Yohay, J. Zhang

Florida Institute of Technology, Melbourne, USA

M.M. Baarmand, S. Butalla, T. Elkafrawy¹¹, M. Hohlmann, D. Noonan, M. Rahmani, M. Saunders, F. Yumiceva

University of Illinois at Chicago (UIC), Chicago, USA

M.R. Adams, L. Apanasevich, H. Becerril Gonzalez, R.R. Betts, R. Cavanaugh, X. Chen, S. Dittmer, O. Evdokimov, C.E. Gerber, D.A. Hangal, D.J. Hofman, V. Kumar, C. Mills, G. Oh, T. Roy, M.B. Tonjes, N. Varelas, J. Viinikainen, H. Wang, X. Wang, Z. Wu

The University of Iowa, Iowa City, USA

M. Alhusseini, B. Bilki⁵⁸, K. Dilsiz⁷⁸, S. Durgut, R.P. Gandrajula, M. Haytmyradov, V. Khristenko, O.K. Köseyan, J.-P. Merlo, A. Mestvirishvili⁷⁹, A. Moeller, J. Nachtman, H. Ogul⁸⁰, Y. Onel, F. Ozok⁸¹, A. Penzo, C. Snyder, E. Tiras, J. Wetzel, K. Yi⁸²

Johns Hopkins University, Baltimore, USA

O. Amram, B. Blumenfeld, L. Corcodilos, M. Eminizer, A.V. Gritsan, S. Kyriacou, P. Maksimovic, C. Mantilla, J. Roskes, M. Swartz, T.Á. Vami

The University of Kansas, Lawrence, USA

C. Baldenegro Barrera, P. Baringer, A. Bean, S. Boren, A. Bylinkin, T. Isidori, S. Khalil, J. King, G. Krintiras, A. Kropivnitskaya, C. Lindsey, W. Mcbrayer, N. Minafra, M. Murray, C. Rogan, C. Royon, S. Sanders, E. Schmitz, J.D. Tapia Takaki, Q. Wang, J. Williams, G. Wilson

Kansas State University, Manhattan, USA

S. Duric, A. Ivanov, K. Kaadze, D. Kim, Y. Maravin, D.R. Mendis, T. Mitchell, A. Modak, A. Mohammadi

Lawrence Livermore National Laboratory, Livermore, USA

F. Rebassoo, D. Wright

University of Maryland, College Park, USA

E. Adams, A. Baden, O. Baron, A. Belloni, S.C. Eno, Y. Feng, N.J. Hadley, S. Jabeen, G.Y. Jeng, R.G. Kellogg, T. Koeth, A.C. Mignerey, S. Nabili, M. Seidel, A. Skuja, S.C. Tonwar, L. Wang, K. Wong

Massachusetts Institute of Technology, Cambridge, USA

D. Abercrombie, B. Allen, R. Bi, S. Brandt, W. Busza, I.A. Cali, Y. Chen, M. D'Alfonso, G. Gomez Ceballos, M. Goncharov, P. Harris, D. Hsu, M. Hu, M. Klute, D. Kovalskyi, J. Krupa, Y.-J. Lee, P.D. Luckey, B. Maier, A.C. Marini, C. McGinn, C. Mironov, S. Narayanan, X. Niu, C. Paus, D. Rankin, C. Roland, G. Roland, Z. Shi, G.S.F. Stephans, K. Sumorok, K. Tatar, D. Velicanu, J. Wang, T.W. Wang, B. Wyslouch

University of Minnesota, Minneapolis, USA

R.M. Chatterjee, A. Evans, S. Guts[†], P. Hansen, J. Hiltbrand, Sh. Jain, M. Krohn, Y. Kubota, Z. Lesko, J. Mans, M. Revering, R. Rusack, R. Saradhy, N. Schroeder, N. Strobbe, M.A. Wadud

University of Mississippi, Oxford, USA

J.G. Acosta, S. Oliveros

University of Nebraska-Lincoln, Lincoln, USA

K. Bloom, S. Chauhan, D.R. Claes, C. Fangmeier, L. Finco, F. Golf, J.R. González Fernández, R. Kamalieddin, I. Kravchenko, J.E. Siado, G.R. Snow[†], B. Stieger, W. Tabb

State University of New York at Buffalo, Buffalo, USA

G. Agarwal, C. Harrington, I. Iashvili, A. Kharchilava, C. McLean, D. Nguyen, A. Parker, J. Pekkanen, S. Rappoccio, B. Roozbahani

Northeastern University, Boston, USA

G. Alverson, E. Barberis, C. Freer, Y. Haddad, A. Hortiangtham, G. Madigan, B. Marzocchi, D.M. Morse, V. Nguyen, T. Orimoto, L. Skinnari, A. Tishelman-Charny, T. Wamorkar, B. Wang, A. Wisecarver, D. Wood

Northwestern University, Evanston, USA

S. Bhattacharya, J. Bueghly, Z. Chen, G. Fedi, A. Gilbert, T. Gunter, K.A. Hahn, N. Odell, M.H. Schmitt, K. Sung, M. Velasco

University of Notre Dame, Notre Dame, USA

R. Bucci, N. Dev, R. Goldouzian, M. Hildreth, K. Hurtado Anampa, C. Jessop, D.J. Karmgard, K. Lannon, W. Li, N. Loukas, N. Marinelli, I. Mcalister, F. Meng, Y. Musienko⁴⁰, R. Ruchti, P. Siddireddy, S. Taroni, M. Wayne, A. Wightman, M. Wolf

The Ohio State University, Columbus, USA

J. Alimena, B. Bylsma, B. Cardwell, L.S. Durkin, B. Francis, C. Hill, W. Ji, A. Lefeld, B.L. Winer, B.R. Yates

Princeton University, Princeton, USA

G. Dezoort, P. Elmer, N. Haubrich, S. Higginbotham, A. Kalogeropoulos, G. Kopp, S. Kwan, D. Lange, M.T. Lucchini, J. Luo, D. Marlow, K. Mei, I. Ojalvo, J. Olsen, C. Palmer, P. Piroué, D. Stickland, C. Tully

University of Puerto Rico, Mayaguez, USA

S. Malik, S. Norberg

Purdue University, West Lafayette, USA

V.E. Barnes, R. Chawla, S. Das, L. Gutay, M. Jones, A.W. Jung, B. Mahakud, G. Negro, N. Neumeister, C.C. Peng, S. Piperov, H. Qiu, J.F. Schulte, N. Trevisani, F. Wang, R. Xiao, W. Xie

Purdue University Northwest, Hammond, USA

T. Cheng, J. Dolen, N. Parashar

Rice University, Houston, USA

A. Baty, S. Dildick, K.M. Ecklund, S. Freed, F.J.M. Geurts, M. Kilpatrick, A. Kumar, W. Li, B.P. Padley, R. Redjimi, J. Roberts[†], J. Rorie, W. Shi, A.G. Stahl Leiton, Z. Tu, A. Zhang

University of Rochester, Rochester, USA

A. Bodek, P. de Barbaro, R. Demina, J.L. Dulemba, C. Fallon, T. Ferbel, M. Galanti, A. Garcia-Bellido, O. Hindrichs, A. Khukhunaishvili, E. Ranken, R. Taus

Rutgers, The State University of New Jersey, Piscataway, USA

B. Chiarito, J.P. Chou, A. Gandrakota, Y. Gershtein, E. Halkiadakis, A. Hart, M. Heindl, E. Hughes, S. Kaplan, I. Laflotte, A. Lath, R. Montalvo, K. Nash, M. Osherson, S. Salur, S. Schnetzer, S. Somalwar, R. Stone, S. Thomas

University of Tennessee, Knoxville, USA

H. Acharya, A.G. Delannoy, S. Spanier

Texas A&M University, College Station, USA

O. Bouhali⁸³, M. Dalchenko, A. Delgado, R. Eusebi, J. Gilmore, T. Huang, T. Kamon⁸⁴, H. Kim, S. Luo, S. Malhotra, D. Marley, R. Mueller, D. Overton, L. Perniè, D. Rathjens, A. Safonov

Texas Tech University, Lubbock, USA

N. Akchurin, J. Damgov, V. Hegde, S. Kunori, K. Lamichhane, S.W. Lee, T. Mengke, S. Muthumuni, T. Peltola, S. Undleeb, I. Volobouev, Z. Wang, A. Whitbeck

Vanderbilt University, Nashville, USA

E. Appelt, S. Greene, A. Gurrola, R. Janjam, W. Johns, C. Maguire, A. Melo, H. Ni, K. Padeken, F. Romeo, P. Sheldon, S. Tuo, J. Velkovska, M. Verweij

University of Virginia, Charlottesville, USA

L. Ang, M.W. Arenton, B. Cox, G. Cummings, J. Hakala, R. Hirosky, M. Joyce, A. Ledovskoy, C. Neu, B. Tannenwald, Y. Wang, E. Wolfe, F. Xia

Wayne State University, Detroit, USA

P.E. Karchin, N. Poudyal, J. Sturdy, P. Thapa

University of Wisconsin - Madison, Madison, WI, USA

K. Black, T. Bose, J. Buchanan, C. Caillol, S. Dasu, I. De Bruyn, L. Dodd, C. Galloni, H. He, M. Herndon, A. Hervé, U. Hussain, A. Lanaro, A. Loeliger, R. Loveless, J. Madhusudanan Sreekala, A. Mallampalli, D. Pinna, T. Ruggles, A. Savin, V. Shang, V. Sharma, W.H. Smith, D. Teague, S. Trembath-reichert, W. Vetens

†: Deceased

1: Also at Vienna University of Technology, Vienna, Austria

2: Also at Université Libre de Bruxelles, Bruxelles, Belgium

3: Also at IRFU, CEA, Université Paris-Saclay, Gif-sur-Yvette, France

4: Also at Universidade Estadual de Campinas, Campinas, Brazil

5: Also at Federal University of Rio Grande do Sul, Porto Alegre, Brazil

6: Also at UFMS, Nova Andradina, Brazil

- 7: Also at Universidade Federal de Pelotas, Pelotas, Brazil
- 8: Also at University of Chinese Academy of Sciences, Beijing, China
- 9: Also at Institute for Theoretical and Experimental Physics named by A.I. Alikhanov of NRC 'Kurchatov Institute', Moscow, Russia
- 10: Also at Joint Institute for Nuclear Research, Dubna, Russia
- 11: Also at Ain Shams University, Cairo, Egypt
- 12: Now at Cairo University, Cairo, Egypt
- 13: Also at Zewail City of Science and Technology, Zewail, Egypt
- 14: Also at Purdue University, West Lafayette, USA
- 15: Also at Université de Haute Alsace, Mulhouse, France
- 16: Also at Tbilisi State University, Tbilisi, Georgia
- 17: Also at Erzincan Binali Yildirim University, Erzincan, Turkey
- 18: Also at CERN, European Organization for Nuclear Research, Geneva, Switzerland
- 19: Also at RWTH Aachen University, III. Physikalisches Institut A, Aachen, Germany
- 20: Also at University of Hamburg, Hamburg, Germany
- 21: Also at Brandenburg University of Technology, Cottbus, Germany
- 22: Also at Skobeltsyn Institute of Nuclear Physics, Lomonosov Moscow State University, Moscow, Russia
- 23: Also at Institute of Physics, University of Debrecen, Debrecen, Hungary, Debrecen, Hungary
- 24: Also at Institute of Nuclear Research ATOMKI, Debrecen, Hungary
- 25: Also at MTA-ELTE Lendület CMS Particle and Nuclear Physics Group, Eötvös Loránd University, Budapest, Hungary, Budapest, Hungary
- 26: Also at IIT Bhubaneswar, Bhubaneswar, India, Bhubaneswar, India
- 27: Also at Institute of Physics, Bhubaneswar, India
- 28: Also at G.H.G. Khalsa College, Punjab, India
- 29: Also at Shoolini University, Solan, India
- 30: Also at University of Hyderabad, Hyderabad, India
- 31: Also at University of Visva-Bharati, Santiniketan, India
- 32: Also at Deutsches Elektronen-Synchrotron, Hamburg, Germany
- 33: Also at Department of Physics, University of Science and Technology of Mazandaran, Behshahr, Iran
- 34: Now at INFN Sezione di Bari ^a, Università di Bari ^b, Politecnico di Bari ^c, Bari, Italy
- 35: Also at Italian National Agency for New Technologies, Energy and Sustainable Economic Development, Bologna, Italy
- 36: Also at Centro Siciliano di Fisica Nucleare e di Struttura Della Materia, Catania, Italy
- 37: Also at Riga Technical University, Riga, Latvia, Riga, Latvia
- 38: Also at Consejo Nacional de Ciencia y Tecnología, Mexico City, Mexico
- 39: Also at Warsaw University of Technology, Institute of Electronic Systems, Warsaw, Poland
- 40: Also at Institute for Nuclear Research, Moscow, Russia
- 41: Now at National Research Nuclear University 'Moscow Engineering Physics Institute' (MEPhI), Moscow, Russia
- 42: Also at Institute of Nuclear Physics of the Uzbekistan Academy of Sciences, Tashkent, Uzbekistan
- 43: Also at St. Petersburg State Polytechnical University, St. Petersburg, Russia
- 44: Also at University of Florida, Gainesville, USA
- 45: Also at Imperial College, London, United Kingdom
- 46: Also at P.N. Lebedev Physical Institute, Moscow, Russia
- 47: Also at California Institute of Technology, Pasadena, USA

-
- 48: Also at Budker Institute of Nuclear Physics, Novosibirsk, Russia
49: Also at Faculty of Physics, University of Belgrade, Belgrade, Serbia
50: Also at Università degli Studi di Siena, Siena, Italy
51: Also at INFN Sezione di Pavia ^a, Università di Pavia ^b, Pavia, Italy, Pavia, Italy
52: Also at National and Kapodistrian University of Athens, Athens, Greece
53: Also at Universität Zürich, Zurich, Switzerland
54: Also at Stefan Meyer Institute for Subatomic Physics, Vienna, Austria, Vienna, Austria
55: Also at Şırnak University, Sirnak, Turkey
56: Also at Department of Physics, Tsinghua University, Beijing, China, Beijing, China
57: Also at Near East University, Research Center of Experimental Health Science, Nicosia, Turkey
58: Also at Beykent University, Istanbul, Turkey, Istanbul, Turkey
59: Also at Istanbul Aydin University, Application and Research Center for Advanced Studies (App. & Res. Cent. for Advanced Studies), Istanbul, Turkey
60: Also at Mersin University, Mersin, Turkey
61: Also at Piri Reis University, Istanbul, Turkey
62: Also at Adiyaman University, Adiyaman, Turkey
63: Also at Ozyegin University, Istanbul, Turkey
64: Also at Izmir Institute of Technology, Izmir, Turkey
65: Also at Necmettin Erbakan University, Konya, Turkey
66: Also at Bozok Universititesi Rektörlüğü, Yozgat, Turkey
67: Also at Marmara University, Istanbul, Turkey
68: Also at Milli Savunma University, Istanbul, Turkey
69: Also at Kafkas University, Kars, Turkey
70: Also at Istanbul Bilgi University, Istanbul, Turkey
71: Also at Hacettepe University, Ankara, Turkey
72: Also at Vrije Universiteit Brussel, Brussel, Belgium
73: Also at School of Physics and Astronomy, University of Southampton, Southampton, United Kingdom
74: Also at IPPP Durham University, Durham, United Kingdom
75: Also at Monash University, Faculty of Science, Clayton, Australia
76: Also at Bethel University, St. Paul, Minneapolis, USA, St. Paul, USA
77: Also at Karamanoğlu Mehmetbey University, Karaman, Turkey
78: Also at Bingol University, Bingol, Turkey
79: Also at Georgian Technical University, Tbilisi, Georgia
80: Also at Sinop University, Sinop, Turkey
81: Also at Mimar Sinan University, Istanbul, Istanbul, Turkey
82: Also at Nanjing Normal University Department of Physics, Nanjing, China
83: Also at Texas A&M University at Qatar, Doha, Qatar
84: Also at Kyungpook National University, Daegu, Korea, Daegu, Korea